CFD STUDY OF CONVECTIVE HEAT TRANSFER TO CARBON DIOXIDE AND WATER AT SUPERCRITICAL PRESSURES IN VERTICAL CIRCULAR PIPES

CFD STUDY OF CONVECTIVE HEAT TRANSFER TO CARBON DIOXIDE AND WATER AT SUPERCRITICAL PRESSURES IN VERTICAL CIRCULAR PIPES

By

FENG ZHOU, B.Eng.

A Thesis

Submitted to the School of Graduate Studies

in Partial Fulfilment of the Requirements

for the Degree

Master of Applied Science

McMaster University

Master of Applied Science (2014)	McMaster University
(Engineering Physics)	Hamilton, Ontario, Canada

TITLE:	Computational Fluid Dynamics Study of Convective Heat Transfer to Carbon Dioxide and Water at Supercritical Pressures in Vertical Circular Pipes
AUTHOR:	Feng Zhou B.Eng. in Nuclear Engineering and Technology University of Science and Technology of China
SUPERVISOR:	Dr. David Novog
NUMBER OF PAGES:	xvi, 120

Abstract

Due to the recent advancement in computer capability, numerical modelling starts to play an important role in making predictions and improving the understanding of physics in the studies of convective heat transfer to supercritical fluids. Many computational studies have been carried out in recent years to assess the ability of different turbulence models in reproducing the experimental data. The performance of these turbulence models varied significantly in predicting the heat transfer at supercritical pressures, especially for the phenomena of heat transfer deterioration (HTD). The results of these studies showed that the accuracy of different turbulence models was also dependent on the flow conditions. It is still necessary to test these turbulence models against newly available experimental data before the final conclusion can be drawn.

In this work computational simulations on convective heat transfer of carbon dioxide (CO_2) and water (H_2O) at supercritical pressures flowing upward in vertical circular pipes have been carried out using the commercial code STAR-CCM+. Detailed comparisons are made between five turbulence models, including AKN low-Reynolds model by Abe et al. (AKN), Standard low-Reynolds k-ε model by Lien et al. (SLR), k-ω model by Wilcox (WI), SST k-ω model by Menter (SST), and the Reynolds Stress Transport (RST) model, against two independent experiments, i.e., water data by Watts (1980) and the recently published carbon dioxide data by Zahlan (2013). The performance of k-ε models with a two-layer approach, and that of k-ε models with wall-functions are also investigated.

For the CO_2 study, where wall temperatures in most cases are above the pseudo-critical temperature (T_{pc}), RST model is found both qualitatively and quantitatively better than other turbulence models in predicting the wall temperatures when HTD occurs. The RST model while superior, predicted HTD at higher heat fluxes as compared to experiments. The wall temperature trends predicted by SST and WI models are very similar to that predicted by RST, except that they start to predict HTD at even higher heat fluxes than RST, and the peak temperatures are overestimated significantly. Because RST and k-ω models (SST and WI) predict the HTD at higher heat fluxes as compared to experiments, often in literature they are overlooked. Rather CFD users should conduct sensitivity analyses on heat flux, and quite often as a result qualitatively excellent agreement can be observed in some of these models.

The low-Reynolds turbulence models, i.e., SLR and AKN, tended to over-predict the wall temperature after the onset of first temperature peak, because the turbulence production predicted by these models failed to regenerate. The wall temperatures for these models did not show recovery after deterioration until the bulk temperature is close to T_{pc}, while experimentally recovery happened

well upstream of this location. The k-ε models with two-layer approach, and the k-ε models with wall-functions both failed to predict the HTD in all cases.

For the H_2O study, where the wall temperatures in most cases are below the pseudo-critical temperature, the SLR model performed the best among all turbulence models in reproducing the experimental data. AKN model was also able to qualitatively predict the observed HTD, however, not as well as SLR. SST and RST models, on the other hand, under-predicted the buoyancy effect even at the lowest mass fluxes and hence did not adequately predict deterioration. In a few high-heat-flux cases with wall temperatures above T_{pc}, all the turbulence models show consistent response to that discussed in the CO_2 study, i.e. RST model is quantitatively better than other turbulence models. Nevertheless, the wall temperature peaks predicted by RST model is very different from that observed experimentally, i.e. the measured peaks are much milder and more flattened than the predicted ones. All the turbulence models including RST overestimate the wall temperatures significantly when $T_b<T_{pc}<T_w$.

The sensitivity studies of mesh parameters, user-defined fluid properties, turbulent Prandtl number, gravitational orientation, and various boundary conditions (e.g. heat flux, mass flux, pressure, and inlet temperature) have also been carried out, aiming to ensure the reliability of the obtained results, and to gain a deeper insight into the physics of heat transfer deterioration in supercritical fluids.

Detailed mechanistic studies of HTD have been carried out for both the CO_2 and H_2O simulations using different turbulence models (RST, SST, and SLR) in various flow conditions. The radial distribution of fluid properties and turbulence at various axial locations provides direct evidence of the mechanisms involved near the locations of deterioration. The buoyancy effect is found to be responsible for the observed HTD in both experiments (i.e., when gravity forces are removed no deterioration is observed). The buoyancy force exerted on the near-wall low-density layer modifies the velocity profile (thus shear stress distribution) in a way that greatly reduces the near-wall turbulence production, resulting in the impairment of heat transfer. In the CO_2 study where the wall temperature exceeds the T_{pc} in a very short distance from the inlet, the "entrance effect" is found to play a more important role in initially impairing the turbulence production. However, this effect is not observed in cases where wall temperature is below T_{pc}, which is attributed to the weaker density variation below T_{pc}.

Acknowledgements

I would like to sincerely thank those who have helped me in different phases of my research. Without their help it would be impossible to finish this thesis.

First, I thank Dr. D.R. Novog who is my academic supervisor, for his constant encouragement and guidance. He has walked me through all the stages of my graduate studies. Without his consistent and illuminating instruction, this thesis could not have reached its present form.

Second, I would like to express my gratitude to the committee of my thesis, Dr. L.K.H. Leung, and Dr. Cotton, for all the valuable comments on my work. The time and effort spent on correcting my thesis and attending my defence are greatly appreciated.

Thanks to my friends and colleagues at McMaster: Darryl, Shaun, Hummel, Yang, Junfeng, Xiaopan, Will, Bruce etc. Special thanks to Darryl, for providing me those invaluable information on CFD and turbulence.

Also, I give my heartfelt gratitude to all the faculty members of Engineering Physics Department at McMaster University, for their precious instructions in various courses. Many thanks to Dr. Ben Rouben for his valuable suggestions and patient guidance in my study and research.

Last but not least, I would like to thank my dearest wife Jing Shen for her love, support and trust in every day of my life. I cannot imagine my life without her. Love her forever. Special thanks to my parents for their eternal love, and consistent support. I wish them good health and happiness forever.

Table of Contents

List of Figures

List of Tables

Nomenclature

Abbreviations

1-D	One-Dimensional
2-D	Two-Dimensional
3-D	Three-Dimensional
ABWR	Advanced Boiling Water Reactor
ACR1000	Advanced CANDU Reactor
AKN	AKN low-Re model by Abe et al.
APWR	Advanced Pressurized Water Reactor
AP1000	Gen III+ type PWR
BWR	Boiling Water Reactor
CANDU	CANada Deuterium Uranium reactor
CFD	Computational Fluid Dynamics
CO_2	Carbon Dioxide
DNS	Direct Numerical Simulation
EC6	Enhanced CANDU 6
ESBWR	Economic Simplified Boiling Water Reactor
EVM	Eddy Viscosity Models
GIF	Generation IV International Forum
H_2O	Water
HL	Heated Length
HTC	Heat Transfer Coefficient
HTD	Heat Transfer Deterioration
HTE	Heat Transfer Enhancement
LES	Large Eddy Simulation
LPV	Large Property Variation
LWR	Light Water Reactor
NS	Navier-Stokes
PWR	Pressurized Water Reactor
RANS	Reynolds-Averaged Navier-Stokes
RST	Reynolds Stress Transport model
RTO	Realizable k-ε model with two-layer approach
RWF	Realizable k-ε model by Shih et al. with wall function
R&D	Research and Development

SCWR	Supercritical Water-Cooled Reactor
SLR	Standard low-Re k-ω model by Lien et al.
SST	Shear Stress Transport model
STO	Standard k-ε model with two-layer approach
SWF	Standard k-ε model with wall functions
UHL	Unheated Length
VHTR	Very High Temperature Reactor
WI	Standard k-ω model by Wilcox

Letters

Bo^*	Buoyancy parameter ($Bo^* = Gr^*/(Re^{3.425}Pr^{0.8})$)
$C, c, C_\mu, C_\varepsilon$	Constants
C_p	Specific Heat (*J/kg-K*)
D	Diameter (*m*)
f	Damping functions
g	Gravity Acceleration (m/s^2)
G	Mass Flux (kg/m^2s)
G_k	Turbulence Gravitational Production (kg/ms^3)
Gr^*	Grashof number ($Gr^* = \frac{g\beta D^4 q_w''}{k\nu^2}$)
h	Heat Transfer Coefficient (*J/kg*)
k, Tke	Turbulence Kinetic Energy (m^2/s^2)
l_m	Mixing length (*m*)
L	Characteristic Length (*m*)
Nu	Nusselt Number ($Nu = hL/\lambda$)
P	Pressure (*MPa*)
P_k	Turbulence Shear Production (kg/ms^3)
Pr	Prandtl Number ($Pr = \frac{C_p\mu}{\lambda} = \frac{\nu}{\alpha}$)
q, Q	Heat Flux (kW/m^2)
Re	Reynolds Number ($Re = UL/\nu$)
T	Temperature (^oC)
T^+	Non-Dimensional Temperature ($T^+ = \frac{(T-T_w)C_p\rho u_\tau}{q_w}$)
$U, V, \mathrm{u}, \mathrm{v}, \mathrm{w}$	Velocity Components (*m/s*)
$\mathrm{u}', \mathrm{v}', \mathrm{w}'$	Fluctuating Velocities (*m/s*)

u^+	Non-Dimensional Velocity ($u^+ = \frac{U}{u_\tau}$)
u_τ	Friction Velocity ($u_\tau = \sqrt{\tau_w/\rho}$)
x_i, x_j	Coordinates (*m*)
y	Distance from the inside surface of the wall (*m*)
y^+	Non-Dimensional Distance ($y^+ = \frac{\rho \mu_\tau y}{\mu}$)
β	Volume Expansivity (*1/K*)
γ	Constant
ε	Rate of Dissipation of k (m^2/s^3)
λ	Thermal conductivity (*W/m-K*)
μ	Molecular viscosity (*kg/m-s*)
μ_t	Turbulent viscosity (*kg/m-s*)
ν	Kinematic viscosity (*kg/m-s*)
ρ	Density (kg/m^3)
$\sigma_k, \sigma_\varepsilon$	Constants
τ_{ij}	Viscous stress tensor ($kg/m\text{-}s^2$ *or Pa*)
ω	Turbulence frequency ($\omega = \varepsilon/k$, s^{-1})

Subscript

b	Bulk
h	Hydraulic equivalent (Diameter)
i	Inner (Diameter)
in	Inlet
o	Outer (Diameter)
out	Outlet
pc	Pseudo-Critical
t	Turbulent
T	Thermal equivalent (Diameter)
w	Wall

1. Introduction

Nuclear energy has increasingly been considered as a key power generation technology to avoid climate change, because it has very low direct green gas emissions. Meanwhile, the three serious nuclear power plant accidents, i.e. Chernobyl disaster, Three Mile Island accident, and the most recent Fukushima accident, have raised the awareness for the safety of nuclear reactors. For the past few decades, large efforts have been made to improve the safety and economy of nuclear reactor systems. Most of existing reactors around the world are considered as generation II systems. A few of the generation III designs are in operation, e.g. ABWR, while others, e.g. APWR and EC6 are under construction or still waiting to be built. Generation III+ designs, e.g. AP1000, ESBWR and ACR1000, offer significant improvements in the safety and economics over the previous generations. Some of them are under construction, while some are going through the licensing process or in various stage of development.

In 2001, a group of nations, including Canada, initiated the Generation IV International Forum (GIF) to collaboratively develop the next generation (Generation IV) nuclear energy systems, which are generally not expected to be available for commercial construction before 2030 [1]. Six nuclear reactor technologies are selected for further research and development, with four primary goals including the improvements in i) sustainability, ii) economics, iii) safety and reliability, and iv) proliferation resistance and physical protection. Canada has decided to pursue two of six Generation IV reactor types, namely the Supercritical-Water-Cooled Reactor (SCWR) and the Very-High-Temperature Reactor (VHTR). The main focus is the Research and Development (R&D) of SCWR, as it is a natural evolution of the current CANDU reactor systems.

1.1 Background

Supercritical-Water-Cooled Reactor (SCWR) is one of the Generation IV reactor types, and the only Gen-IV type using light water as coolant, making it the most similar to existing power reactor concepts. SCWR operates above the thermodynamic critical point of water (374^{o}C, 22.1MPa), which enables significant simplifications of the system, and a thermal efficiency of 44% or more, compared to about 34% efficiency for the current LWRs.

The SCWR concept combines the design and operation experiences gained from the existing water cooled reactors (PWR, CANDU & BWR) and supercritical fossil fuel plant. Canada is developing a pressure-tube-type SCWR concept, which is designed to generate 1200MW electric power with a core outlet temperature of 625^{o}C at the pressure of 25MPa. With such a high reactor outlet temperature, a thermal efficiency of 48% can be achieved [2]. The Canadian SCWR has evolved from the horizontal design with feeders and on-power refuelling to the vertical simplified design with no inlet feeders and with batch refuelling. Figure 1 shows a preliminary concept of the current vertical-core pressure-tube type SCWR.

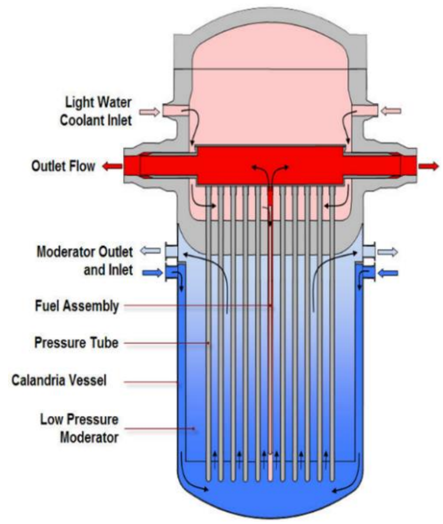

Figure 1 Current design of the Canadian pressure-tube type SCWR *[3]*

The unique features of SCWR offered many advantages over the current water cooled reactors, e.g. simpler system, lower capital cost, higher efficiency and better fuel utilization. However, these advantages also come with several technical challenges associated with the development of SCWR, which are generally in two areas, i.e. thermal-hydraulics and safety, material and chemistry. The main focus of this thesis is on the thermal-hydraulics and safety of SCWR.

One of the R&D priorities for SCWR thermal-hydraulics and safety is the study of heat transfer and pressure losses in fuel channels at supercritical pressures, including the collection of experimental data and the development of prediction methods [4]. The establishment of the maximum power output and safety margin of SCWR requires the information on heat transfer and pressure drop in fuel channels. Understanding heat transfer characteristics from fuel to coolant is vital important to the prediction of cladding and fuel temperatures which have been selected as criteria for the safety of fuel.

1.2 Heat Transfer at Supercritical Pressures

The coolant remains single-phase throughout the SCWR system, as it operates above the critical pressure (Figure 2). As a result, the system can be considerably simplified, resulting in a design with the elimination of recirculation system, steam separator and steam dryer compared with a typical BWR system, and the elimination of pressurizer and steam generators when compared with PWR.

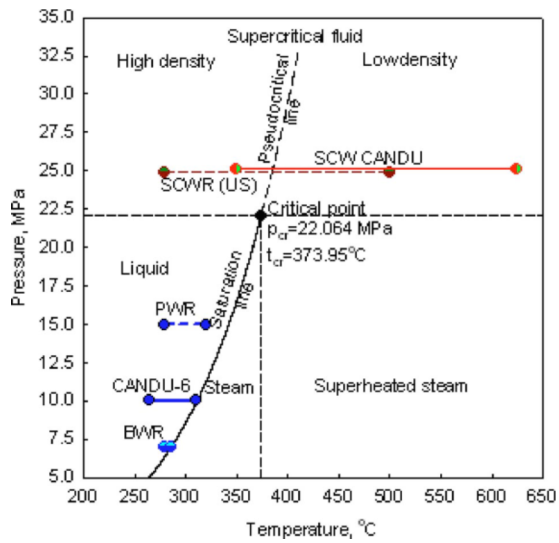

Figure 2 Operating conditions for SCWR and modern reactors *[5]*

Although under supercritical conditions the boiling crisis does not occur, the thermal-physical properties of water will still undergo drastic variations in the vicinity of pseudo-critical temperature (T_{pc}). Figure *3* shows the thermal physical properties versus temperature at pressure of 25 MPa. It can be seen that the density, thermal conductivity, and dynamic viscosity all decrease dramatically when approaching pseudo-critical point (T_{pc} = 384.9°C at 25 MPa). For the thermal conductivity, there also exists a local maximum near the pseudo-critical point (the peak may not correspond to T_{pc}). The specific heat reaches its maximum which is as high as 76.4 kJ/kg-K at T_{pc}. Due to this sharp increase in heat capacity, the Prandtl number has a large peak at the pseudo-critical temperature.

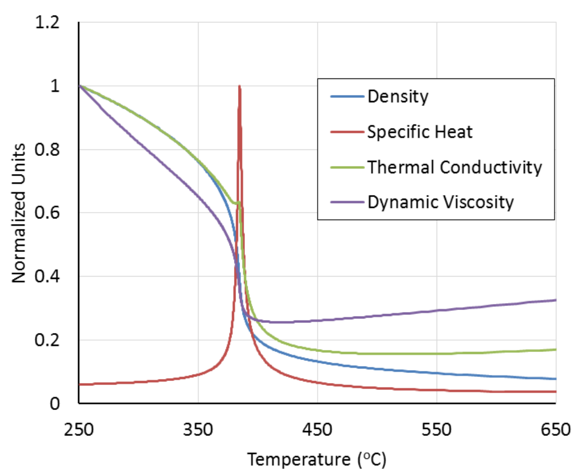

Figure 3 Normalized thermo-physical property variation of water at 25MPa calculated using NIST REFPROP *[6]* by the author

The strong variations of thermal-physical properties lead to heat transfer phenomena which are very different from standard single phase flow. In general, there are three heat transfer modes in fluids at supercritical pressures, i.e. Normal Heat Transfer, Heat Transfer Enhancement (HTE), and Heat Transfer Deterioration (HTD). The Dittus-Boelter equation:

$$Nu = 0.023 \cdot Re^{0.8} \cdot Pr^{1/3}$$

is a widely used empirical correlation for forced turbulent flow in circular pipes, which gives a good approximation for flows far from the supercritical region. The Normal Heat Transfer mode at supercritical pressures is characterized with heat transfer coefficient (HTC) close to that calculated using the Dittus-Boelter equation. However, it has been found that at supercritical pressures the HTC can deviate from this equation significantly, especially near the T_{pc}. At relatively low heat flux with bulk temperature near the T_{pc}, the HTC may become higher than that predicted by equation (1.1), which is often referred to as Heat Transfer Enhancement. As the heat flux increases, HTC may deviate below the Dittus-Boelter equation, which is termed Heat Transfer Deterioration (HTD). As previously stated, there is no concern about the boiling crisis in SCWR. Nevertheless, the HTD will also lead to the large increase in the wall temperature, though in a much smoother way compared to that caused by the boiling crisis. There are a variety of hypotheses on relating to the mechanisms which give rise to HTD and these are discussed elsewhere in this thesis. Predicting the onset of HTD and its subsequent recovery is critical to the reactor design and safety analysis.

1.3 Computational Fluid Dynamics (CFD) in SCWR

One-dimensional (1-D) thermal-hydraulic codes, e.g. RELAP and CATHENA, are widely used in the nuclear industry to perform simulations for the reactor design and safety analysis. However, the main drawback of these 1-D codes is that they are naturally incapable of simulating the complex three-dimensional (3-D) turbulent flow, e.g. the flow in the inlet plenum, or within the sub-channels of a fuel assembly. They also rely heavily on the empirical correlations, most of which are based on experiments performed far away from the supercritical region. Although, a large number of empirical correlations have been developed to predict the heat transfer under supercritical conditions, in general, those correlation are still not capable of predicting the heat transfer with such strong property variations, especially when the heat transfer is deteriorated. Other empirical relationships for shear stresses and pressure drop are also lacking.

Due to the recent advancement in computer capability, Computational Fluid Dynamics (CFD) has been increasingly used in the nuclear reactor design and safety analysis to study the thermal-hydraulic behaviour in the reactor coolant system. While experiments provide direct and the most relevant information, CFD has the ability to provide greater detail on the fluid properties than the experimental approach due to the measurement limitations in experiments. Thus, CFD is a valuable tool to study the effects of large property variation within thermal-fluid flows such as those existing near the pseudo-critical point.

While large effort has been made to improve the performance of CFD in two-phase flows, the reliability of CFD-based prediction is still much greater for single phase flows rather than multiphase flows [7]. An attractive feature of CFD for simulating supercritical-fluid flow is that the coolant remains single-phase in the SCWR primary circuit, regardless of the temperature rise or pressure drop, and the continuity of fluid properties simplifies the simulations relative to multi-phase flows.

However, one of the main difficulties with CFD in the study of supercritical fluids lies in turbulence modelling. Many CFD studies have been carried out in recent years to assess the ability of different turbulence models in reproducing experimental data (see Chapter 2 for details). The performance of these turbulence models varied significantly, especially under conditions which give rise to deteriorated heat transfer. The results of these studies showed that the quality of prediction of different turbulence models was also dependent on the flow conditions. This makes it even more difficult to find the optimal turbulence model for the simulation of supercritical-fluid flow. It is still necessary to compare these turbulence models against new experimental data before the final conclusions can be drawn.

1.4 Objectives of this Study

The primary objective of this present study is to further validate the CFD method in the study of convective heat transfer to supercritical fluids, by developing a single-phase methodology based on the commercial CFD code STAR-CCM+ (v8.06.005). Several of the most promising turbulence models available in STAR-CCM+, including four two-equation turbulence models and the second order Reynolds Stress Transport Model (RST) are selected for comparison. The recently published experimental data on supercritical carbon dioxide flow by Zahlan et al. [7] have been selected as a benchmark for this study, as well as the supercritical water data from University of Manchester by Watts [8].

Within this objective, our aim is not just to compare turbulence models but rather to better understand the heat transfer phenomena under supercritical conditions. In particular with a focus on deterioration mechanisms that occur as a result of buoyancy forces within the fluid, but are still far away from conditions where buoyancy forces would traditionally give rise to natural convection phenomena. The mechanisms of HTD are critical to understanding the safety of SCWR.

In order to better capture the near-wall turbulence production in a flow with high Reynolds number and strong property variations, it is believed that a low y+ wall treatment is essential. This hypothesis is tested by studying various wall treatments on both low y+ type and high y+ type meshes.

Throughout the simulations in this thesis, sensitivity studies to the turbulent Prandtl number (Pr_t) and various boundary conditions (heat flux, mass flux, pressure, and inlet temperature) are performed, as some phenomena predicted by the code are found very sensitive to these parameters.

2. Literature Review

This chapter reviews both numerical and experimental studies of heat transfer to supercritical fluids.

In the first section, a description of the three modes of heat transfer at supercritical pressures is presented, with an emphasis on the review of mechanisms of heat transfer deterioration (HTD) proposed by different researchers.

Then, some of the important experiments on heat transfer of supercritical water and carbon dioxide are reviewed and discussed. Those experiments are essential for the validation of CFD predictions and the establishment of appropriate models. Two of the reviewed experiments are selected as benchmarks for this study.

In section 2.3, CFD studies of heat transfer to supercritical fluids in vertical circular tubes are reviewed (those in annuli and bundle geometries are not included). The experience and conclusions in these studies are valuable to this present study. It is found later that not all previous works are consistent with the results contained within this thesis.

2.1 Different Modes of Heat Transfer in Supercritical Regime

As discussed earlier, there are mainly three modes of heat transfer for supercritical fluids, i.e. normal heat transfer, heat transfer enhancement (HTE), heat transfer deterioration (HTD). These heat transfer modes have been described in the literatures by Jackson and Hall [9] [10], and can be explained with the help of Figure 4.

In the mode of normal heat transfer, the fluid temperature is not in the vicinity of T_{pc}, hence, the property variations are relatively small, and the HTC is close to that calculated using Dittus-Boelter Equation (Figure 4a). When the bulk temperature increases close to the pseudo-critical temperature, the large increase in specific heat and decrease in the viscosity may result in an improvement in the heat transfer effectiveness, i.e. enhanced heat transfer (see Figure 4b). However, this is typically only observed in low-heat-flux experimental conditions. With increasing heat flux, the near-wall fluid gains sufficient energy input to raise its temperature beyond T_{pc}. As a result, the high-specific-heat region moves away from the wall and become more localized, and low-density fluids start to occupy the near-wall region, which may lead to the impairment of enhanced heat transfer (see Figure 4c). As the experimental heat flux increases further, HTC becomes lower than that computed using Dittus-Boelter Equation, which marks the occurrence of HTD. Efforts to explain the HTD date back to early 1960s. And, it has been widely recognized that there are two main phenomena which give rise to HTD, i.e. buoyancy and flow acceleration. Both mechanisms alter the shear stress distribution within pipe flow.

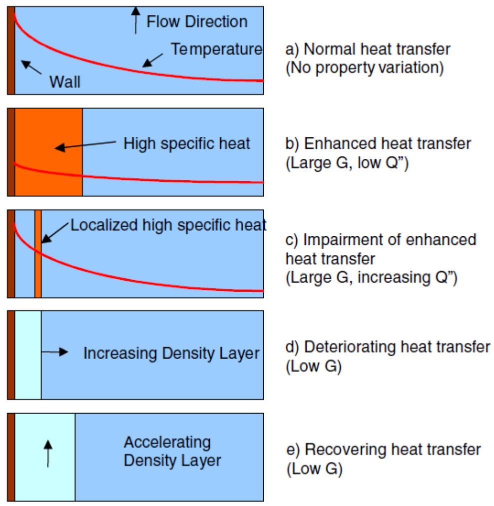

Figure 4 Description of Three Modes of Heat Transfer *[11]*

2.1.1 Buoyancy-Induced Deterioration of Heat Transfer

Explanations involving the buoyancy effect in the upward water flow were first proposed by Shitsman [12] and also by Hall [13] in 1968. According to Shitsman, the transverse turbulent velocity fluctuation might be damped by the correlation and direction of forces, resulting in the laminarization of boundary layer. Hall and Jackson [14] presented a different explanation which has been widely accepted. They believed that the action of buoyancy modifies the distribution of shear stress in a manner that reduces turbulence production, resulting in the impairment of heat transfer as described below.

When the supercritical fluid is flowing upward in a heated tube, there exists a low-density layer near the wall. This low-density layer grows thicker as the fluid is continuously heated, while the core fluid remains high-density (see Figure *4* d). The resultant density difference will generate a buoyant force on the low-density layer resulting in a modified velocity profile and shear stress distribution. Normally, the shear stress due to the velocity gradient is directly related to turbulence production in a wall shear flow. When the low-density layer and associated buoyancy force is sufficient to reduce the shear stress in the near-wall region where turbulence production is normally the greatest, it acts to greatly reduce this production. As a result, the effectiveness of heat transfer is greatly impaired, and the buoyancy-induced HTD occurs. Jackson [15] states that as the low-density layer grows further, the sign of shear stress will eventually be changed in the central region, which means the wall layer will start exerting an upward force on the core fluid, and at some stage downstream the production of turbulence will be restored. Thus this explanation accounts not only for the observed HTD, but also for the subsequent rapid recovery in the heat transfer. The buoyancy-induced HTD only occurs in upward flow where mass velocity is relatively low. In downward flow, the buoyancy force is opposite to the flow direction, which will result in the greater shear stress and turbulence production leading to the improvement of heat transfer.

2.1.2 Acceleration-Induced Deterioration of Heat Transfer

Under moderate-to-high mass flux conditions and with higher heat fluxes, the near-wall buoyancy effect is not sufficient for turbulence suppression, while the flow acceleration caused by thermal expansion becomes significant. This significant flow acceleration requires an additional applied pressure difference. Near the wall, this pressure gradient is greater than that which is needed to accelerate the flow, because the fluid velocity in the near-wall region is smaller than that in the core region. As a result, the shear stress drops more quickly with distance from the tube wall than it would in the absence of flow acceleration. Thus, the turbulence production is reduced due to the lower shear stress in the near-wall region, and consequently the acceleration-induced HTD occurs [16].

As opposed to buoyancy-induced HTD, acceleration-induced HTD occurs in both upward and downward flows. This effect has been found in Shiralkar and Griffith's experiments [17] [18] and has been theoretically discussed by Hall [19]. However, the acceleration effect will not be investigated in this study, as the selected experimental conditions are in the regime where buoyancy is the dominant effect of the observed HTD.

2.2 Experimental Studies

Many experiments have been carried out to study the heat transfer to supercritical fluids, most of which are in supercritical water (H_2O) and supercritical carbon dioxide (CO_2). In 2001, Cheng [20] presented a literature review on the studies of heat transfer at supercritical pressures, covering review papers, experimental study, numerical analysis and empirical correlation. Cheng reviewed twelve supercritical heat transfer experiments in both water and carbon dioxide performed since late 1950s. Pioro and Duffey carried out an exhaustive literature search for experiments in supercritical water [21], and also for experiments in CO_2 [22]. According to Pioro and Duffey, the majority of the experimental data obtained are in vertical tubes, some are in horizontal tubes, and only a few in other flow geometries. A brief review of some of the important experiments are presented below.

2.2.1 Experimental Heat Transfer in Supercritical Water

As early as 1963, Shitsman [23] investigated the heat transfer to supercritical water flowing inside tubes. The phenomenon of HTD was first observed at low mass fluxes (430 kg/m^{2}s) when the bulk temperature is increased towards the pseudo-critical temperature. It was noted that different from two-phase boiling crisis, the temperature spike associated with HTD is less pronounced and recovers after deterioration. He also found that at low heat flux the localized enhancement in heat transfer can occur, and will progress from enhanced condition to deteriorated condition as the heat flux increases (see Figure 5). Based on his data, several correlations were developed for the prediction of heat transfer coefficient.

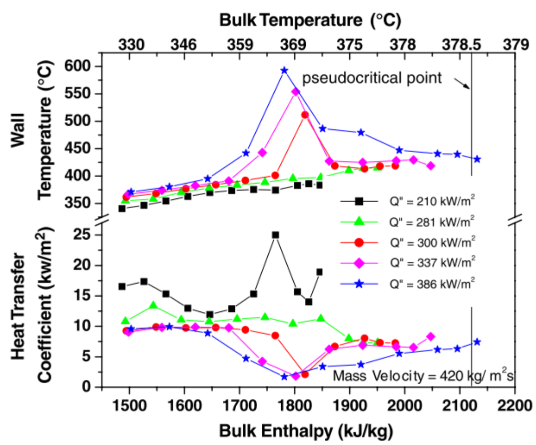

Figure 5 Shitsman data – Low mass flux, low to medium heat flux (fig. by [11])

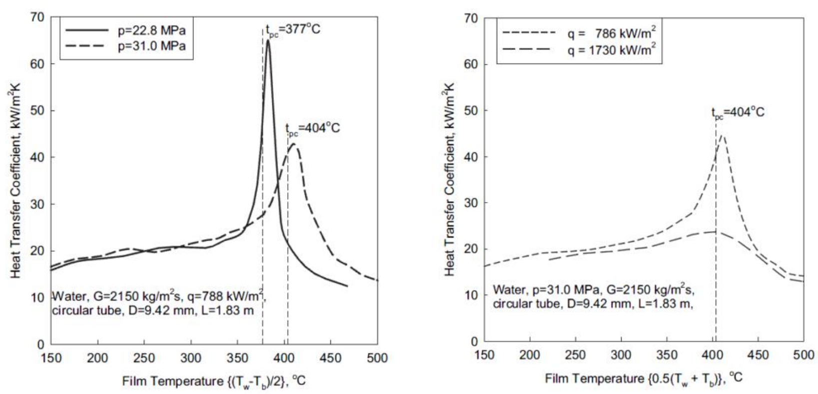

Figure 6 Swenson data – Pressure effect (left) and heat flux effect (right) *[25]*

Bishop et al. (1964) [24] conducted experiments in supercritical water flowing upward inside small-diameter tubes within the following parameter ranges:

$$P=22.8\text{–}27.6\text{MPa},\ T_b=282\text{–}527^{o}\text{C},\ G=651\text{–}3662\text{kg/m}^2\text{s and } q=0.31\text{–}3.46\text{MW/m}^2.$$

Swenson et al. (1965) [25] also carried out a set of tests to supercritical water using tubes with larger diameter (9.42 mm). Swenson found that HTC shows a sharp peak when the film temperature is within the pseudo-critical temperature range, and this peak decreases with increasing pressure and heat flux (see Figure 6). A new correlation was developed by modifying the conventional non-dimensional model to account for the physical property variation across the boundary layer. Out of 2951 data points, 95 percent lie within ±15 percent of the correlation.

Ackerman et al. (1970) [26] investigated heat transfer to water at supercritical pressures flowing in smooth vertical pipes within a wide range of pressure, mass fluxes, heat fluxes and diameters. They observed the pseudo-boiling phenomenon which is due to the large density difference between the near-wall region and core region. This pseudo-film boiling may lead to HTD, but is not the only reason for HTD. Ackerman also noted that when the pseudo-critical temperature was between the bulk temperature and wall temperature, i.e. $T_b<T_{pc}<T_w$, so called “unpredictable” heat transfer performance can occur. The process of pseudo-film boiling is similar to film boiling which occurs at subcritical pressures. The pseudo-film-boiling concept is used to understand the HTD in Ackerman’s work. However, as Jackson [15] stated, it is difficult to explain the rapid recovery in heat transfer downstream of the local HTD on the basis of nucleate and film boiling concepts.

Ornatskiy et al. (1970) [27] investigated the appearance of deteriorated heat transfer in five parallel tubes with stable and pulsating flow. They found that the deteriorated heat transfer in the assembly at supercritical pressures depended on the heat flux to mass flux ratio (q/G) and flow conditions. For stable flow, the HTD occurred when q/G = 0.95-1.05kJ/kg. For pulsating flow, HTD occurred at a lower ratio, i.e. q/G ≥ 0.68-0.9kJ/kg. In 1971, Ornatskiy et al. [28] carried out experiments with rising and falling water flow at supercritical pressures in a tube with a diameter of 3mm. HTD was observed in both upward and downward flows. Later, Ornatskiy et al. [29] investigated normal and deteriorated heat transfer in a vertical annulus. The deteriorated heat transfer zone was observed visually as a red hot spot appearing in the upper section of the test tube.

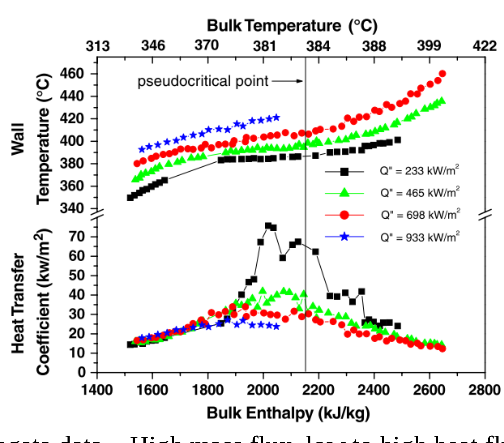

Figure 7 Yamagata data – High mass flux, low to high heat flux (fig. by *[11]*)

Yamagata et al. (1972) [30] investigated forced convective heat transfer to supercritical water flowing in both vertical and horizontal tubes. Yamagata's data which are one of the most popular datasets used for validating numerical models were obtained at relatively high mass flux (1400 kg/m^{2}s). The enhancement in heat transfer was observed when the bulk temperature is increased through the pseudo-critical temperature (see Figure *7*). It was found that this increase in HTC decreases with the increase in heat flux and pressure, and at some point this enhancement will cease.

Alekseev et al. (1976) [31] conducted experiments in a circular vertical tube cooled with super-critical water. They found that at q/G<0.8kJ/kg normal heat transfer occurred. Beyond this value, HTD can occur, and with the increase in heat flux, the temperature peak resulting from HTD moves towards the tube inlet (see Figure *8*).

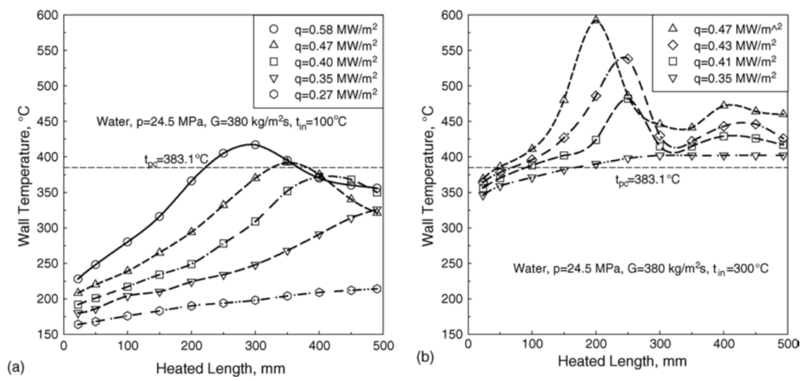

Figure 8 Alekseev data – upward flow at various heat fluxes

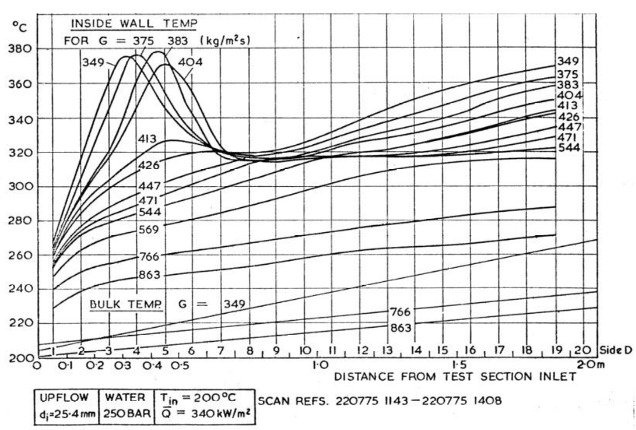

Figure 9 Watts data – upward flow at various mass fluxes

Watts (1980) [32] investigated heat transfer to supercritical water in a smooth circular tube with upward and downward flows. The experimental procedure and detailed experimental results can also be found in the report by Jackson (2009) [8]. There were 11 sets of experimental data, while a typical set of observations was taken with the same inlet temperature and heat flux, but over a range of mass flux. HTD was observed at low mass fluxes, and eventually was replaced by normal heat transfer at high mass fluxes (see Figure *9*). Watts's data were taken as a reference for the validation of turbulence modes in this present study. Detailed experimental investigation can be found in Chapter 4.

Pis'menny et al. (2005) [33] carried out experimental studies on heat transfer to supercritical water flowing upward and downward in vertical tubes. These heat transfer data were obtained at pressure of 23.5 MPa, mass flux within the range from 250 to 2200 kg/m^{2}s, inlet temperature from 100 to 415^{o}C and heat flux up to 3.2 MW/m^2. Pis'menny found that the heat transfer coefficient for downward flow can be higher about 50% compared to that of the upward flow. It was also found that the regime of deteriorated heat transfer for their flow conditions started earlier in the upward flow compared to that in the downward flow (see Figure *10*).

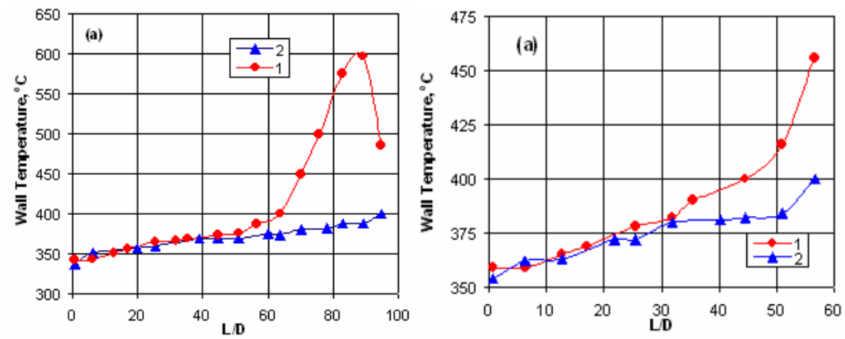

Figure 10 Pis'menny data – Left: $q_{1,\ 2}$=390 kW/m^2, Right: q_1=457kW/m^2 q_2=509 kW/m^2 (P=23.5MPa, D=6.28mm; G=509kg/m^{2}s; 1: upward, and 2: downward)

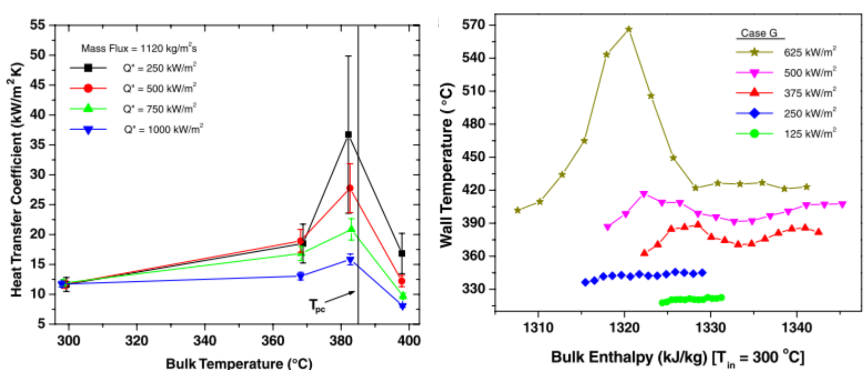

Figure 11 Licht data – HTC at high mass flux (Left) and Evolution in HTD (Right)

Licht et al. (2008) [34] investigated heat transfer to water at supercritical pressures in a circular and square annular flow geometry. Operating conditions included mass velocities of 350-1425kg/m^{2}s, heat fluxes up to 1.0MW/m^2, and bulk inlet temperatures up to 400^{o}C. They found that high mass flux data exhibit an enhancement in heat transfer centered near the pseudo-critical temperature, and an increase in heat flux reduces this effect. HTD was observed at sub-pseudo-critical temperatures, and was found to be dependent on geometry (see Figure *11*). The main purpose of their study is to validate the selected heat transfer correlations and buoyancy criteria.

2.2.2 Experimental Heat Transfer in Supercritical Carbon Dioxide

Carbon dioxide is a valuable alternative to water in experimental studies at supercritical pressures, as it has a relative low critical point (31.1ºC, 7.39 MPa) which can greatly reduce the cost of such experiments. Those experimental data can easily be transformed into water equivalent values using fluid-to-fluid scaling laws [35]. Also, many non-dimensional correlations for HTC are the same for supercritical water and supercritical carbon dioxide.

Hall and Jackson (1969) [14] conducted a set of experiments on heat transfer to supercritical carbon dioxide flowing upward and downward in a vertical circular pipe within the following parameter range: P=7.58MPa, T_{in}=14-24ºC, q=40-57kW/m^2, Re_{in} =113×10^3. Deterioration was observed only in the upward flow. It was concluded that the buoyancy forces cause the reduction of shear stress in the wall layer and consequently impaired the turbulent diffusion (detailed explanation has been discussed in section 2.1.1).

Fewster and Jackson (1976, 2004) [36] [37] investigated heat transfer for turbulent flow of carbon dioxide inside vertical tubes at supercritical pressures. Consistent with the discussion in Chapter 1, they found that three modes of heat transfer at supercritical pressures exist, i.e. normal heat transfer, improved heat transfer and HTD (see Figure *12*). They found that when HTD occurred, the wall temperatures had a sharp first peak that moved upstream as the inlet temperature increased.

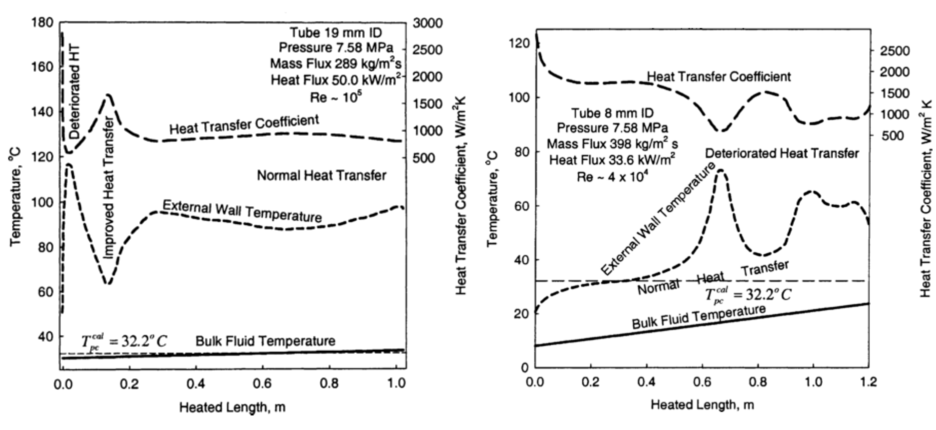

Figure 12 Fewster CO_2 data – Improved heat transfer (Left) and HTD (Right)

Kim et al. (2007) [38] [39] carried out experiments with carbon dioxides at supercritical pressure flowing upward in vertical tubes with circular, triangular, and square cross-sections. Their experimental data were obtained at pressure of 8MPa under various conditions: T_{in}=15-32°C, q=3-180kW/m^2, and G=209-1230 kg/m^{2}s. Wall temperature distributions for the non-circular tubes along the heating region were found to show similar trend to that of the circular tube at the same heat flux and mass velocity. However, an earlier peak of wall temperature was also observed in the case of the non-circular tubes, due to the different heating areas (see Figure *13*). A heat transfer correlation is proposed based the experimental data, which gives ±20% accuracy for 90% of the data in predicting the averaged Nusselt number.

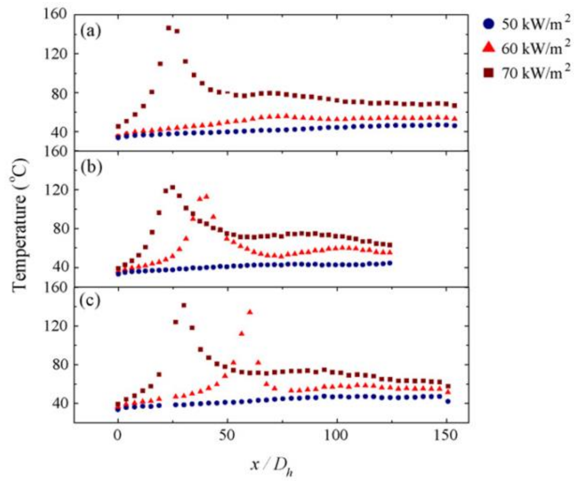

Figure 13 Kim CO_2 data - Comparison of wall temperature distributions; (a) circular tube, (b) triangular tube, and (c) square tube at the mass velocity of 523kg/m^{2}s

Bae and Kim (2011) [40] conducted a series of experiments on heat transfer to CO_2 at supercritical pressures flowing upward and downward in vertical tubes and an annular channel under different flow conditions. After comparing the heat transfer in a tube with that in an annular channel with the same thermal equivalent hydraulic diameter, a good agreement between the tube and annular channel is seen. They also found that the deterioration of heat transfer occurred both in upward and downward flow, but less severe in the downward flow than in the upward. Several existing heat transfer correlations, i.e. Bishop's, Jackson and Hall's, Watts and Chou's correlations, were evaluated against their experimental data, and new correlations were suggested.

Zahlan (2013) [7] performed thermal-hydraulic tests in a directly heated vertical tube using CO_2, at high sub-critical, near-critical and supercritical pressures. These tests conducted over wide ranges of flow condition. At supercritical region, the experimental flow conditions covers the following range: P=7.48-8.67MPa, T_{in}=7.06-13.4°C, G=405-2030kg/m^{2}s, q=20-436kW/m^2. The pressure effect, mass flux effect, and heat flux effect on the heat transfer at supercritical conditions were all discussed. Zahlan's supercritical CO_2 data were also selected as benchmarks for this present study. See Chapter 4.1 for detailed experimental investigation.

2.3 CFD Studies

Due to the limitation of measurements in experimental studies, detailed information on fluid properties in the near-wall region has rarely been obtained. These experiments require high pressure, high temperature, and high power, thus are expensive and difficult to perform. Numerical modelling, which is a powerful tool to make predictions, has the ability to provide insight on the microscopic behaviour in flows of supercritical fluids. Many CFD simulations have been carried out in recent years to study the heat transfer to supercritical fluids. Some of the important CFD studies are described as follows, while the parameters and conclusions of these studies are summarized in Table 1 at the end of this section.

Koshizuka et al. (1995) [41] performed a 2-D numerical analysis on the HTD in a vertical pipe with supercritical water flowing upward, based on a parabolic solver for steady-state equations. The k-ε turbulence model by Jones-Launder was selected, and physical properties are treated as variables. The results agree well with the experimental data of Yamagata et al. [30]. A map of deterioration is presented after calculations with various combinations of flow rate and heat flux. Koshizuka found that there are two different mechanism of HTD. The property variation was employed to explain HTD at high mass flux, while the buoyancy effect was used to explain HTD at low mass flux. The observed oscillation of wall temperature at very heat flux is also explained using the unstable characteristics of the thick thermal boundary layer.

He et al. [42] compared a number of two-equation low-Reynolds turbulence models in his studies of mixed convective heat transfer to carbon dioxide at supercritical pressure, against the CO_2 data by Weinberg [43]. The wall temperatures in most of the simulated cases were below T_{pc}. Their results showed that most of the turbulence models were to some extent able to reproduce the buoyancy-induced HTD in these experiments; however, the performance of these models varied significantly. Some low-Re number models (by Abe et al., and by Launder et al.) over-predicted the HTD and the downstream wall temperatures, while some (by Chien, and by Lam et al.) predicted the downstream wall temperatures quite close to the measured values but underestimated the peak temperatures. They also found that the non-uniformity of properties did not have a strong effect on the results in their particular case and their observed deterioration was explained using buoyancy effect. For the recovery of heat transfer, they believed that further increases in buoyancy causes turbulence to be regenerated in the core region where the velocity profile is inverted, consistent with the theories of Jackson discussed in the previous sections.

He et al. [44] also performed computational simulations on convective heat transfer to CO_2 at a pressure just above the critical value, and compared it to Fewster and Jackson's experiments [36]. The wall temperatures in their case were above T_{pc}. A more complicated V2F turbulence model by

Behnia et al. was incorporated, along with the AKN model. It was found that both models were able to capture the general trends of wall temperature change, however with a significant over-prediction of the buoyancy effect (i.e., the predicted peak wall temperatures are much higher than observed experimentally). Both model predicted a recovery after the onset of HTD, albeit not within the right range (the predictions showed recovery further downstream than the experiment). The effect of buoyancy was explained by relating it to the large-property-variation (LPV) region.

Sharabi et al. [45] carried out CFD studies of heat transfer to supercritical water flowing upward and downward in a circular pipe in an in-house CFD code. The performance of eight low-Reynolds number turbulence modes, including k-τ, k-ω, and k-ε formulations, were assessed against the experimental data by Pis'menny [33]. In their cases, the wall temperatures were above the pseudo-critical temperature. All the k-ε low-Reynolds number models were found able to qualitatively predict the HTD, but with significant over-estimation of the peak wall temperatures. After the onset of HTD, all the low-Re k-ε models predicted a mild recovery of the wall temperature, but it was too weak to be considered as a full recovery and wall temperatures were thus over-predicted in the downstream region. Both k-ω and k-τ model failed to predict HTD at relatively low heat fluxes, however with increases in heat fluxes k-ω model started to predict HTD, but in a much milder way than observed experimentally.

Later, based on Sharabi's results [45], a continuing assessment of the turbulence models for heat transfer in supercritical water was carried out by Ambrosini [46] in the commercial CFD code STAR-CCM+. The two-layer all y+ wall treatment, along with standard low-Reynolds k-ε model by Lien, AKN model and V2F model were selected for comparison. The low-Re, the AKN and the V2F models provide very similar results. Similar to previous studies, they were all able to qualitatively predict the HTD, but again overestimated the wall temperature and failed to correctly predict the recovery. The two-layer all y+ treatment, on the other hand, did not predict the occurrence of HTD in all the cases.

Sharabi et al. [47] also assessed the performance of different turbulence models in comparison with Yamagata's H_2O data [30] and Kim's CO_2 data [38] in circular tubes. The simulated conditions in Yamagata's experiments showed heat-transfer enhancement at bulk temperature close to T_{pc}. In cases with relatively low heat fluxes, all the turbulence models predicted the wall temperature fairly well, including six low-Re k-ε models, k-ω by Wilcox, SST, k-τ model by Speziale and standard k-ε with wall function. With increasing heat flux, the buoyancy started to outbalance the enhancement in heat transfer, and the discrepancies between the predictions by those turbulence models and the experimental data also increased significantly. In those high-heat-flux cases, all the low-Re k-ε models predicted a greater buoyancy effect than the experiments; the k-τ model showed the best results; the standard k-ε with wall function exhibited a rather poor performance. For cases from Kim's experiments where HTD occurred and $T_{pc}<T_w$, all the low-Re k-ε models were able to qualitatively predict the HTD, however, with significant overestimation of peak temperature. The gentle recovery predicted by these models was again too weak to be considered a full recovery. The k-ω model by Wilcox and SST models showed some HTD at relatively higher heat fluxes, again in a much milder way than the experiments.

Palko et al. [48] performed a numerical investigation of HTD using the low-Re k-ω turbulence model (SST) and the standard k-ε model with both wall functions and damping functions. Two independent experiments at low and high coolant flow rates respectively are used for this study. The experiment by Ornatskiy [28] is performed at very high flow rate, while the experiment by Shitsman [23] is in the region of high-buoyancy influence. SST model was found to predict the wall temperature (both onset and recovery of the HTD) in very good agreement with the experimental data from both experiments. The standard k-ε model with wall function for coarse grid, and that with nonlinear damping function for fine grid both fail to calculate the heat transfer in the deteriorated region. After comparing the results by SST model with and without the buoyancy terms in the NS equation, it was concluded that the HTD observed at low flow rate is caused by buoyancy force, while the HTD at high flow rate is caused by another mechanism (likely acceleration).

Liu et al [49] studied the HTD numerically in both circular tubes and an annular channel using eight low-Re-number models which include six low-Reynolds k-ε models, a V2F model, and the SST model. The same flow conditions as used in Palko's study, i.e. experiments by Shitsman [23] and that by Ornatskiy [28], are simulated using FLUENT in circular tubes. For Shitsman's experiments which is at low mass fluxes, most of the turbulence models predict a temperature peak in the inlet region, while SST model is quantitatively better than others and is able to predict a second peak further downstream. For Ornatskiy's experiment at high mass fluxes, the majority of models are able to predict the HTD to some extent; SST model again presents the best performance. It was found that the increase in tube diameter will lead to the aggravation of HTD, which is most obvious at low mass flux. They also found that the HTD observed at high mass flux in circular tube and annular channel are similar to each other when the hydraulic equivalent diameters (D_h) and thermal equivalent diameters (D_T) are the same.

In the CFD studies mentioned above, the low-Reynolds k-ε models were found to predict the HTD qualitatively, and they were often recommended to predict the heat transfer of supercritical fluids and were widely used for the mechanism study of HTD. However, they demonstrated rather poor performance in predicting the level of deterioration and the subsequent recovery. SST and k-ω models seem to predict the HTD at higher heat flux, and in a very few cases SST model predicted the HTD in an excellent agreement with the experiments. The performance of turbulence models varies and seems to also depend on flow conditions. No clear conclusion can be drawn on which turbulence model is superior to others. Hence, further investigations are still necessary.

Table 1 A list of CFD studies with supercritical fluid flowing in vertical circular tubes

Reference	Experiments	Flow conditions	Flow Geometry	Turbulence Models Compared	Conclusions
Koshizuka 1995	Yamagata H_2O	P=24.52MPa; various combinations of G and q	D=10mm HL=2m upward (y+<0.1 at largest Re)	(In-house) k-ε model by Jones-Launder	HTD at low flow rate is caused by buoyancy; HTD at high flow rate is due to decrease in viscosity and Pr; Thermo-acoustic oscillations was also discussed.
He 2004	Weinberg, CO_2 (University of Manchester)	P=7.58MPa; T_{pc}=32.2ºC; T_{in}=8, 10ºC; q=9210-15100W/m^2; m=0.029-0.082kg/s	D=19mm UHL=64D HL=129D upward (y+<0.5 axial×radial:92×62)	(SWIRL 'in-house') All Low-Reynolds number turbulence models: k-ε by Launder, Sharma (LS), k-ε by Chien (CH), k-ε by Lam, Bremhorst (LB), k-ε AKN model, k-ε by Myoung, Kasagi (MK), k-ω model by Wilcox (WI)	WI and MK both predict too weak the influence of buoyancy; The rest were able to reproduce HTD to some extent; the buoyancy occurs sooner and is stronger using LS and AKN; all over-predict the T_w for the developed region at some point.
Sharabi 2007	Pis'menny 2006 H_2O	P=23.5MPa; T_{pc}=379.35ºC; T_{in}=391, 300 ºC; q=390, 433, 457, 509, 750, 1172 W/m^2; G=509, 2193kg/m^{2}s	D=6.28mm UHL=64D HL=57.3, 95.5D Upward, downward (y+<1 axial×radial: 162×70)	(In-House) k-τ model by Speziale (SAA) k-ω model by Wilcox (WI) Six low-Re k-ε models: by Jones-Launder (JL) by Launder-Sharma (LS) by Lam-Bremhorst (LB) by Chien (CH) by Yang-Shih (YS) by Abe et al. (AKN)	For the forced convection: all models fairly well; When HTD occur: all k-ε models over-predict T_w; increasing the q/G, the discrepancy increase; k-ω model reproduce T_w fairly well at high q/G.
He 2008	Fewster and Jackson CO_2	P=7.58MPa; T_{in}=13.2, 20.5ºC; q=68, 318W/m^2; Re=187950, 44046	D=5mm UHL=75D HL=150D upward, downward (y+<0.5, axial×radial:120×106)	(SWIRL 'in-house') low-Reynolds number AKN model, V2F model	AKN was better for the conditions considered; Both were able to capture the general trends of T_w, but still very different from that in experiments; buoyancy was explained by relating it to the large-property-variation (LPV) region.
Ambrosini 2009	Pis'menny 2006 H_2O	P=23.5MPa; T_{pc}=379.35ºC; T_{in}=300 ºC; q=390W/m^2; G=509kg/m^{2}s	D=6.28mm UHL=64D HL= 95.5D Upward, downward (y+<1 axial×radial: 500×68)	(STAR-CCM+) Two-Layer All y+ Wall Treatment (all y+); Standard Low-Re k-ε Model (low-Re); AKN model; V2F model	low-Re, AKN, and V2F provide very similar results, all over-estimate T_w without recovering; all y+ (probably two-layer wall treatment) cannot catch laminarization.

Sharabi 2009	Yamagata 1972 H_2O; Kim 2005 CO_2	H_2O: P=24.5MPa; T_{in} varied; q=233,698W/m^2; G=1260kg/m^{2}s CO_2: P=8MPa; T_{in}=15ºC; q=23, 30W/m^2; G=314kg/m^{2}s	(Low-Re: y+<0.5; WF: y+>30; axial×radial: 120×70) H_2O: D=7.5mm HL=1.5m Upward CO_2: D=7.8, 7.9, 9.8mm HL=1.2m Upward	(THEMAT "in-house") k-τ model by Speziale (SP) k-ω model by Wilcox (WI) Standard k-ε model with wall function (WF) Six low-Re k-ε models: by Jones-Launder (JL) by Launder-Sharma (LS) by Lam-Bremhorst (LB) by Chien (CH) by Yang-Shih (YS) by Abe et al. (AKN) (Fluent) SST k-ω	H_2O: SAA model shows the best results; all low-Re models predict a greater buoyancy than in exp.; CO_2: All low-Re k-ε models are able to qualitatively predict HTD, but with significant over-estimation of the wall temperature; WI and SST models start to respond to HTD at higher heat flux, though in a much milder way than exp.
Palko 2008	Shitsman H_2O Ornatskij H_2O	Shitsman: P=23.3MPa; q=319.87W/m^2; G=430kg/m^{2}s Ornatskij: P=25.5MPa; q=1810W/m^2; G=1500kg/m^{2}s	y+=0.1, 0.5, 1, 6 Shitsman: D=8mm Upward Ornatskij: D=3 mm Upward	(Ansys-CFX 11.0) SST model by Menter; Standard k-ε model with wall function (coarse grid); Standard k-ε model with damping function (fine grid)	SST predicts the HTC in a very good agreement with the experimental results; The standard k-ε model for both coarse grid and fine grid fail to calculate the heat transfer in the deteriorated region; The HTD in Shitsman experiment is caused by buoyancy force, while the HTD in Ornatskij's is caused by other mechanism.
Liu 2013	Shitsman H_2O (Low mass flux) Ornatskij H_2O (High mass flux) Glushchenko H_2O (High mass flux)	Shitsman: P=23.3MPa; q=319.87W/m^2; G=430kg/m^{2}s Ornatskij: P=25.5MPa; q=1810W/m^2; G=1500kg/m^{2}s Glushchenko: P=23.5MPa; q=2410W/m^2; G=2200kg/m^{2}s	Shitsman: D=8mm (compared to 4, 2 mm) Upward Ornatskij: D=3mm (compared to 5, 7 mm) Upward Glushchenko: Annular channel D_o/D_i=10mm/8mm Upward	(Fluent) Eight low-Reynolds-number turbulence models: Abid (AB), Lam–Bremhors (LB), Launder–Sharma (LS), Yang–Shih (YS), Abe–Kondoh–Nagano (AKN), Chang–Hsieh–Chen (CHC), k–ε–v2–f (V2F) and Shear Stress Transport (SST) model.	SST perform better than other models in predicting the HTD in all the three experiments; HTD phenomenon becomes more notable with the increase of the tube diameter at both high and low mass fluxes; With the same D_h and D_T, the HTD observed at high mass flux in circular tube and annular channel are similar to each other.

3. Numerical Modelling

As mentioned earlier, the main difficulty of modelling supercritical flow lies in the modelling of turbulence in particular in the presence of large property gradients. There are three available numerical methods that are well developed for modelling turbulence, i.e. Reynolds-Averaged Navier-Stokes (RANS), Large Eddy Simulation (LES), and Direct Numerical Simulation (DNS). Both LES and DNS are highly costly in terms of computing resources, and are not extensively used for industrial flow computations, therefore, are out of consideration in this thesis. The RANS approach, which is mainstay of engineering flow calculation, focuses on the mean flow and the effects of turbulence on mean flow properties. In this study, several two-equation turbulence models, and the Reynolds Stress Transport (RST) model for RANS equations are used and discussed.

3.1 Governing Equation for Mean Flow

The supercritical fluid undergoes strong variation in fluid properties including density in the vicinity of T_{pc}. On the other hand, the hydraulic pressure drop in this study is negligible compared to the system pressure (25MPa for H_2O, 8.5MPa for CO_2). Hence, the governing equations for mean flow can be expressed as follows:

Continuity:

$$\frac{\partial \rho}{\partial t} + \frac{\partial}{\partial x_i}(\rho u_i) = 0$$

Momentum:

$$\frac{\partial \rho u_i}{\partial t} + \frac{\partial}{\partial x_j}\left(\rho u_j u_i\right) = -\frac{\partial p}{\partial x_i} + \frac{\partial \tau_{ij}}{\partial x_j} + \rho g_i$$

Energy:

$$\frac{\partial \rho C_p T}{\partial t} + \frac{\partial}{\partial x_j}\left(\rho C_p u_j T\right) = \frac{\partial}{\partial x_j}\left(k\frac{\partial T}{\partial x_j}\right) + \frac{\partial}{\partial x_j}\left(u_i \tau_{ij}\right)$$

where the viscous stress tensor τ_{ij} is defined as:

$$\tau_{ij} = \mu\left(\frac{\partial u_i}{\partial x_j} + \frac{\partial u_j}{\partial x_i}\right) - \frac{2}{3}\mu\frac{\partial u_k}{\partial x_k}\delta_{ij}$$

3.2 Turbulence Modelling

3.2.1 Reynolds-Averaged Navier-Stokes Equations

The above Navier-Stokes (NS) equations describe the mean flow without turbulence. In order to take into consideration the effect of turbulent fluctuations on properties of the mean flow, an approach called time-averaging or Reynolds-Averaging is adopted. The velocity variable u_i in the NS equations are replaced by the sum of a mean and fluctuating component,

$$u_i = \widetilde{u_i} + u_i'$$

where the Favre averaging is used, since the flow of supercritical fluids is a variable-property turbulent flow with large density variation. The Favre averaging is defined as follows:

$$\widetilde{u_i} = \frac{1}{\bar{\rho}} \lim_{\Delta t \to \infty} \frac{1}{\Delta t} \int_t^{t+\Delta t} \rho(\rho, \tau)\, u_i(x, \tau) d\tau$$

This yields the following Reynolds-Averaged Navier-Stokes equations:

Continuity:

$$\frac{\partial \bar{\rho}}{\partial t} + \frac{\partial}{\partial x_i}(\bar{\rho}\tilde{u}_i) = 0$$

Momentum:

$$\frac{\partial \bar{\rho}\tilde{u}_i}{\partial t} + \frac{\partial}{\partial x_j}\left(\rho \tilde{u}_j \tilde{u}_i\right) = -\frac{\partial \bar{p}}{\partial x_i} + \frac{\partial}{\partial x_j}\left(\bar{\tau}_{ij} - \bar{\rho}\widetilde{u_i' u_j'}\right) + \bar{\rho} g_i$$

Energy:

$$\frac{\partial \bar{\rho} C_p \bar{T}}{\partial t} + \frac{\partial}{\partial x_j}\left(\bar{\rho} C_p \tilde{u}_j \bar{T}\right) = \frac{\partial}{\partial x_j}\left(k \frac{\partial \bar{T}}{\partial x_j} - \bar{\rho} C_p \widetilde{u_j' T'}\right)$$

The momentum equation contains the term $-\bar{\rho}\widetilde{u_i' u_j'}$, which is called Reynolds stress tensor, including three normal stresses, i.e. $-\bar{\rho}\widetilde{u'^2}, -\bar{\rho}\widetilde{v'^2}, -\bar{\rho}\widetilde{w'^2}$, and three shear stresses, i.e. $-\bar{\rho}\widetilde{u'v'}, -\bar{\rho}\widetilde{u'w'}, -\bar{\rho}\widetilde{w'v'}$. Similarly, in the energy equation, the term $-\bar{\rho} C_p \widetilde{u_j' T'}$, which are called turbulent fluxes, are three additional unknowns yielded after the time-averaging operation. It is notable that the viscous energy dissipation term in the energy equation is neglected, as it is much smaller than the turbulent term in high-Reynolds-number flow.

3.2.2 Boussinesq Hypothesis and Mixing Length Model

In order to compute the turbulent flows using the above RANS equations, we need to develop turbulence models to predict the six Reynolds stresses and the three turbulent heat fluxes, and to close the RANS equation. The most common RANS turbulence models are classified in the following table, see Table *2*.

Table 2 Types of turbulence models *[51]*

Order	No. of extra equations	Name of Turbulence models
First Order	Zero	Mixing length model
	One	Spalart-Allmaras model
	Two	k-ε model
		k-ω model
Second Order	Two	Algebraic stress model
	Seven	Reynolds stress transport model

The first order models which are also called Eddy Viscosity Models (EVM) are based on the analogy between laminar and turbulent flow. The analogy can be expressed as follows:

$$\begin{cases} \tau_{ij} = \mu\left(\frac{\partial u_i}{\partial x_j} + \frac{\partial u_j}{\partial x_i}\right) - \frac{2}{3}\mu\frac{\partial u_k}{\partial x_k}\delta_{ij} & \text{Viscous Stresses} \\ {\tau_{ij}}^t = -\rho\widetilde{u_i' u_j'} = \mu_t\left(\frac{\partial \tilde{u}_i}{\partial x_j} + \frac{\partial \tilde{u}_j}{\partial x_i}\right) - \frac{2}{3}\rho k\delta_{ij} & \text{Reynolds Stresses} \end{cases}$$

$$\begin{cases} q_i = \frac{k}{C_p}\frac{\partial T}{\partial x_i} & \text{Heat Fluxes} \\ q_i^t = -\bar{\rho}\widetilde{u_j' T'} = \frac{k_t}{C_p}\frac{\partial T}{\partial x_i} = \frac{\mu_t}{Pr_t}\frac{\partial T}{\partial x_i} & \text{Turbulent Fluxes} \end{cases}$$

which is often referred to as the Boussinesq hypothesis. Pr_t is the turbulent Prandtl number which is ratio of turbulent viscosity and turbulent diffusivity (of heat). Its default value in Star-CCM+ is 0.9 which is recommended for near-wall flows (0.5 for jets and mixing layers, and 0.7 in axisymmetric jets). In this study the value of 0.9 is used, the sensitivity of Pr_t is also carried out and the results are shown later in section 5.1.3.

Since the kinematic turbulent viscosity ν_t, has dimensions m^2/s, it can be expressed as a product of turbulent velocity scale u (m/s) and a turbulent length scale l (m). Dimensional analysis yields:

$$\nu_t = \frac{\mu_t}{\rho} = Clu$$

where *C* is a dimensionless constant of proportionality.

The zero equation model, i.e. mixing length model, has no PDE that describes the transport of Reynolds stresses and turbulent fluxes. Since there is strong connection between the mean flow and the behaviour of the largest eddies, the mixing length model attempts to link the characteristic velocity scale of eddies with the mean flow properties. For simple two-dimensional turbulent flows where the only significant Reynolds stress is $-\bar{\rho}\widetilde{u'v'}$, and the only significant mean velocity gradient is $\partial U/\partial y$, the turbulent velocity scale is expressed as follows:

$$u = cl\left|\frac{\partial U}{\partial y}\right|$$

where *c* is a dimensionless constant. Replacing u in the equation of ν_t by the above relation yields:

$$\nu_t = \frac{\mu_t}{\rho} = Clu = l_m^2\left|\frac{\partial U}{\partial y}\right|$$

The two constants *C* and *c* are absorbed into a new length scale l_m which is often referred to as mixing length. This is the Prandtl's mixing length model. Hence, the turbulent Reynolds stress is described by

$${\tau_{xy}}^t = -\rho\widetilde{u'v'} = \rho l_m^2\left|\frac{\partial U}{\partial y}\right|\frac{\partial U}{\partial y}$$

which is very straightforward and useful for estimating the Reynolds shear stress and turbulence production (see section 5.3). Nevertheless, the mixing length model may be inappropriate in this present study, as it relies on the assumption that the local production and dissipation of turbulence are in the state of equilibrium [15] [51], but the convection and diffusion of turbulent kinetic energy (see the following section for the definitions) will become significant when turbulence is changing rapidly which is very likely in this study.

3.2.3 Governing equation for turbulent kinetic energy k

The two-equation models including k-ε and k-ω models, focus on the mechanisms that affect the turbulent kinetic energy k, which is defined by

$$\mathrm{k} = \frac{1}{2}(\widetilde{u'^2} + \widetilde{v'^2} + \widetilde{w'^2})$$

The governing equation for turbulent kinetic energy can be expressed as follows [51]:

$$\frac{\partial(\rho k)}{\partial t} + \frac{\partial \rho k \tilde{u}_j}{x_j} = \frac{\partial}{\partial x_j}\left(-\widetilde{p'u_j'} - \rho\frac{1}{2}\widetilde{u_i' \cdot u_i'u_j'} + \mu\frac{\partial k}{x_j}\right) - \rho\widetilde{u_i'u_j'} \cdot S_{ij} - \beta g_i \rho\widetilde{u_i'T'} - 2\mu\widetilde{s_{ij}'s_{ij}'}$$

terms in which, from left to right, are "Rate of change of k", "Transport of k by convection", "Transport of k by pressure", "Transport of k by Reynolds stress", "Transport of k by viscous stresses", "Rate of production of k due to shear stress", "Rate of production of k due to gravity", "Rate of dissipation of k", respectively. The dissipation of k is caused by work done by the smallest eddies against viscous stresses, which is normally expressed as the product of density and ε. Thus, ε which is equal to $2\nu\overline{s'_{ij}s'_{ij}}$, is the rate of dissipation of k per unit mass. This equation introduces two new unknown correlations, i.e. Transport of k by pressure and Reynolds stress (D_k), and Rate of dissipation of k (ε_k or $\rho\varepsilon$) which need to be modeled.

The production and dissipation terms are used to calculate the production rate and dissipation rate of turbulence in the later HTD study (see section 5.3 and 5.5). It is notable that in a supercritical flow, based on the CFD results by He et al. [44], the rate of production of k due to gravity, i.e. gravitational production (G_k), is two orders of magnitude smaller than the shear production (P_k).

3.2.4 The k-ε models

In the k-ε model [51], k and ε based on dimensional analysis are used to define the velocity scale u and length scale l, i.e.

$$u = k^{1/2}, l = \frac{k^{3/2}}{\varepsilon}$$

Similar dimensional analysis yields:

$$\mu_t = C\rho l u = \rho C_\mu \frac{k^2}{\varepsilon}$$

where C_μ is the dimensionless constant.

The standard k-ε model uses the following transport equations for k and ε:

$$\frac{\partial(\rho k)}{\partial t} + \frac{\partial \rho k \tilde{u}_j}{x_j} = \frac{\partial}{x_j}\left((\mu + \frac{\mu_t}{\sigma_k})\frac{\partial k}{\partial x_j}\right) + P_k + G_k - \rho\varepsilon$$

$$\frac{\partial(\rho \varepsilon)}{\partial t} + \frac{\partial \rho \varepsilon \tilde{u}_j}{x_j} = \frac{\partial}{x_j}\left((\mu + \frac{\mu_t}{\sigma_\varepsilon})\frac{\partial \varepsilon}{\partial x_j}\right) + C_{1\varepsilon}\frac{\varepsilon}{k}(P_k + G_k) - C_{2\varepsilon}\rho\frac{\varepsilon^2}{k}$$

which contain another four adjustable constants, i.e. $C_{1\varepsilon}, C_{2\varepsilon}, \sigma_k, \sigma_\varepsilon$. The shear production P_k, and gravitational production G_k, are defined using the following equations based on the Boussinesq hypothesis:

$$P_k = -\rho\widetilde{u'_i u'_j} \cdot S_{ij} = \mu_t\left(\frac{\partial \tilde{u}_i}{\partial x_j} + \frac{\partial \tilde{u}_j}{\partial x_i}\right)\frac{\partial \tilde{u}_i}{\partial x_j}$$

$$G_k = -\beta g_i \rho\widetilde{u'_i T'} = \beta g_i \frac{k_t}{C_p}\frac{\partial T}{\partial x_i} = \beta g_i \frac{\mu_t}{Pr_t}\frac{\partial T}{\partial x_i}$$

The value of these five constants in the standard k-ε model by Launder and Sharma [52] that are arrived at by comprehensive data fitting for a wide range of turbulent flows are listed as follows:

$$C_\mu = 0.09, \sigma_k = 1.00, \sigma_\varepsilon = 1.30, C_{1\varepsilon} = 1.44, C_{2\varepsilon} = 1.92$$

These values are used in the STAR-CCM+ in Standard k-ε model.

k-ε model with wall functions

The k-ε model in its original formulation was applied with wall functions. The wall-function approach avoids the need to integrate the model equation right through to the wall by using the log-law in the near-wall region, which can be written as

$$u^+ = \frac{U}{u_\tau} = \frac{1}{\kappa} \ln E y_p^+$$

where the Von Karman constant κ is equal to 0.41, and wall roughness parameter E equal to 9.8 for smooth walls (wall roughness will decrease the value of E). The assumption that rate of turbulence production equals the rate of dissipation is also used, which yields

$$k = \frac{u_\tau^2}{\sqrt{C_\mu}}, \varepsilon = \frac{u_\tau^3}{\kappa y}$$

For heat transfer, the wall function based on the universal near-wall temperature distribution is used:

$$T^+ \equiv \frac{(T - T_w) C_p \rho u_\tau}{q_w} = \sigma_{T,t} \left(u^+ + P \left[\frac{\sigma_{T,l}}{\sigma_{T,t}} \right] \right)$$

where $\sigma_{T,l}$ is the molecular Prandtl number, and $\sigma_{T,t}$ turbulent Prandtl number, and P is the P-function which is a correction function dependent on the ratio $\sigma_{T,l}/\sigma_{T,t}$.

The wall function approach, (or high y+ wall treatment in STAR-CCM+), requires that the near wall cell lies within the logarithmic region of the boundary layer, which starts at about y+=20. However, the wall function approach is based on assumptions that are only valid at high Reynolds numbers. For heat transfer at supercritical condition, the fluid properties vary significantly in the near-wall region, the viscous sub-layer need to be resolved in order to depict this strong variation. Hence, k-ε model with wall function are inherently unsuitable for modeling flows in this thesis, which has been proved after the assessment of performance of various turbulence models with high y+ wall treatment (see section 5.1.5).

Low-Reynolds number k-ε model

In order to resolve the viscous sublayer, the k-ε model was modified to use either low-Reynolds number approach or two-layer approach (discussed later). A low y+ or all y+ wall treatment in a very fine mesh (y+<1) is necessary for those two approaches to properly resolve the viscous sublayer.

The most common approach for k-ε model is to apply damping functions to some or all of the coefficients in the model (C_μ, $C_{\varepsilon 1}$, and $C_{\varepsilon 2}$). These damping functions (f_μ, f_1, f_2, respectively) modulate the coefficients as functions of a turbulent Reynolds number, often also incorporating the wall distance. Many models incorporating damping functions have been proposed in the literature, which are often referred to as low-Reynolds k-ε type models. Two of them are chosen for this present study, i.e. Standard low-Re k-ε model and the AKN low-Re model (more information on these two models can be found in section 3.3.3).

The equations for k, ε, and eddy viscosity, as well as the RANS equations need to be integrated to the wall, hence the boundary condition for ε need to be specified. Lam and Bremhorst use $\partial \varepsilon / \partial \mathrm{y} = 0$ as the boundary condition, while other low-Re number k-ε models often use the modified dissipation rate

$$\tilde{\varepsilon} = \varepsilon - 2\nu\left(\partial\sqrt{k}/\partial n\right)^2$$

which allows a more straightforward boundary condition $\tilde{\varepsilon} = 0$ at the wall.

<u>k-ε model with two-layer approach</u>

The two-layer approach, suggested by Rodi [53], is an alternative to the low-Reynolds number approach that allows the k-ε model to be applied in the viscous sub-layer. As its name implies, the computation is divided into two layers.

In the near-wall viscous region, i.e. $Re_y = \frac{y\sqrt{k}}{\nu} < 200$, only the k-equation is solved, and the length scale is specified using

$$l = \kappa y\left[1 - \exp(-Re_y/A)\right]$$

which is similar in the form to expression of mixing length in the viscous sub-layer (as discussed in section 3.2.2), and $A = 2\kappa C_\mu^{-3/4}$. The rate of dissipation and eddy viscosity in this region can be written as

$$\varepsilon = C_\mu^{3/4} k^{3/2}/l$$

$$\mu_{t,v} = C_\mu^{1/4} \rho k^{1/2} l$$

Hence, the turbulence dissipation rate ε and the turbulent viscosity μ_t are specified as function of wall distance in the viscous region.

For fully turbulent region, i.e. $Re_y = \frac{y\sqrt{k}}{\nu} \geq 200$, the normal transport equations for k and ε are solved and the eddy viscosity is computed with usual relationship

$$\mu_{t,t} = C_\mu \rho k^2/\varepsilon$$

The value of ε specified in the near-wall layer are blended smoothly with the values computed from solving the transport equation far from the wall, which avoid instabilities associated with the difference between these two values at the join. In STAR-CCM+, this two-layer approach works with either low-Reynolds number type mesh, i.e. y+<1, or wall-function type meshes, i.e. y+>30. However, as mentioned earlier, very fine mesh (y+<1) is necessary for this approach to properly resolve the viscous sublayer.

3.2.5 The k-ω models

- **Wilcox k-ω model**

Since the rate of dissipation of turbulence kinetic energy ε is not the only possible length scale determining variable, many other two-equation models are also developed. The k-ω model, which is the most prominent alternative to k-ε model, uses the turbulence frequency ω = ε/k (dimensions s^{-1}) as the second variable. Hence, the eddy viscosity is given by

$$\mu_t = \rho k/\omega$$

in which the length scale is

$$l = \frac{k^{1/2}}{\omega}$$

The standard k-ω model by Wilcox [54] uses the following transport equations for k and ω:

$$\frac{\partial(\rho k)}{\partial t} + \frac{\partial \rho k \tilde{u}_j}{x_j} = \frac{\partial}{x_j}\left((\mu + \frac{\mu_t}{\sigma_k})\frac{\partial k}{\partial x_j}\right) + P_k + G_k - \beta^* \rho k \omega$$

$$\frac{\partial(\rho \omega)}{\partial t} + \frac{\partial \rho \omega \tilde{u}_j}{x_j} = \frac{\partial}{x_j}\left((\mu + \frac{\mu_t}{\sigma_\omega})\frac{\partial \omega}{\partial x_j}\right) + \gamma_1 \frac{\omega}{k}(P_k + G_k) - \beta_1 \rho \omega^2$$

The model constants in the original version [55] are as follows:

$$\gamma_1 = 0.553, \beta_1 = 0.075, \beta^* = 0.09, \sigma_k = 2.0, \sigma_\omega = 2.0$$

One of the main advantage of k-ω model is that its integration to the wall does not require wall-damping functions in low-Reynolds number applications. The value of k at the wall is set to zero, while the frequency ω tends to infinity at the wall. We can either specify a very large value at the wall or apply a hyperbolic variation $\omega_P = 6\nu/(\beta_1 y_P^2)$ at the near-wall grid point. It is also noteworthy that the results are insensitive to the details of this treatment [51]. Zhu's work [56] has proved that k-ω model has better performance in predicting the boundary layer in the flow of supercritical fluids than the k-ε models, which is further confirmed in this thesis.

However, the main drawback of the standard k-ω model is its boundary condition of ω in a free stream, where $k \to 0, \omega \to 0$. The eddy viscosity $\mu_t = \rho k/\omega$, is indeterminate or infinite as $\omega \to 0$, so a small non-zero value of ω must be specified. And the results of the standard k-ω model was found to be dependent on this non-zero value, which is a serious problem in external aerodynamics and aerospace application, where free stream boundary conditions are frequently used. Nevertheless, for pipe flows in this present study, the sensitivity of the standard k-ω model to inlet turbulent condition is less of a problem.

- **Menter SST k-ω model**

Based on the fact that k-ε is far less sensitive to the assumed values in the free stream, Menter [57] proposed a hybrid model, i.e. SST k-ω model, which combines positive features of standard k-ε model and k-ω model. SST model uses a transformation of the k-ε model into a k-ω model in the near-wall region and the standard k-ε model in the fully turbulent region far from the wall. The Reynolds stress and k-equation of SST are identical to that of the standard k-ω model, while the ω-equation is obtained by substituting $\varepsilon = k\omega$, which yields:

$$\frac{\partial(\rho\omega)}{\partial t} + \frac{\partial\rho\omega\tilde{u}_j}{x_j} = \frac{\partial}{x_j}\left((\mu + \frac{\mu_t}{\sigma_{\omega1}})\frac{\partial\omega}{\partial x_j}\right) + \gamma_2\frac{\omega}{k}(P_k + G_k) - \beta_2\rho\omega^2 + 2\frac{\rho}{\sigma_{\omega2}\omega}\frac{\partial k}{\partial x_j}\frac{\partial\omega}{\partial x_j}$$

The model constants after Menter's revision in 2003 [58] as used in STAR-CCM+ are listed as follows:

$$\gamma_2 = 0.44, \beta_2 = 0.083, \beta^* = 0.09, \sigma_k = 1.0, \sigma_{\omega1} = 2.0, \sigma_{\omega2} = 1.17$$

The above transformed equation is very similar to the one in standard k-ω model, but adds an additional non-conservative cross-diffusion term (rightmost), which makes it give identical results to the k-ε model. Blending functions are used to achieve a smooth transition between the standard k-ε model in the far field and the transformed k-ω model near the wall. However, for the cross-diffusion term, Menter uses a blending function that includes this term far from the wall but not near the wall, which make SST model distinguished from the k-ε model. Therefore, this approach effectively blends the k-ε model in the far field with k-ω model near the wall. Details of the blending functions can be found in the Menter's report [58], and will not be discussed here.

It is worth mentioning that SST model adopts the following limiters on the eddy viscosity and turbulence kinetic energy production,

$$\mu_t = \frac{a_1\rho k}{\max(a_1\omega, SF_2)}$$

$$P_k = \min(10\beta^*, 2\mu_t S_{ij} \cdot S_{ij} - \frac{2}{3}\rho k \frac{\partial \tilde{u}_i}{\partial x_j} \delta_{ij})$$

which helps give improved performance in flows with adverse pressure gradients and prevents the build-up of turbulence in stagnation regions, respectively.

SST model is stable and robust, and has be proven to give superior performance in various applications. Although, the free stream effect is less of an issue in this study, the SST model was found to coverage better than the standard k-ω model by Wilcox (see further below).

3.2.6 Reynolds Stress Transport Model

The Reynolds Stress Transport (RST) model is a popular second order model, and makes direct use of governing equations for the second order moments, i.e. Reynolds stresses and turbulent fluxes, instead of the Boussinesq hypothesis. Thus, RST model overcomes several drawbacks of the first order models in predicting flows with complex strain fields or significant body forces, where the individual Reynolds stresses are poorly represented by the Boussinesq equation. RST model's six momentum equations for Reynolds stresses can be written as

$$\frac{\partial\left(\rho \widetilde{u_i' u_j'}\right)}{\partial t} + \frac{\partial \rho \widetilde{u_i' u_j'} \tilde{u}_k}{\partial x_k} = \frac{\partial}{\partial x_k}\left(\mu \frac{\partial \widetilde{u_i' u_j'}}{\partial x_k} + D_{ij}^t\right) + P_{ij} + G_{ij} + \Phi_{ij} - \varepsilon_{ij}$$

P_{ij} and G_{ij} are the rate of production of Reynolds stress $\widetilde{u_i' u_j'}$ due to shear stress and gravity respectively, and can be expressed as follows

$$P_{ij} = -\rho \widetilde{u_i' u_k'} \frac{\partial \tilde{u}_j}{\partial x_k} - \rho \widetilde{u_j' u_k'} \frac{\partial \tilde{u}_i}{\partial x_k}$$

$$G_{ij} = -\beta g_j \rho \widetilde{u_i' T'} - \beta g_i \rho \widetilde{u_j' T'}$$

The scalar transport equation is

$$\frac{\partial\left(\rho \widetilde{u_i' T'}\right)}{\partial t} + \frac{\partial \rho \widetilde{u_i' T'} \tilde{u}_j}{\partial x_j} = \frac{\partial}{\partial x_j}\left(\mu \frac{\partial \widetilde{u_i' T'}}{\partial x_j} + D_{it}^t\right) + P_{it} + G_{it} + \Phi_{it} - \varepsilon_{it}$$

where P_{it} and G_{it} is given by

$$P_{it} = -\rho \widetilde{u_i' u_k'} \frac{\partial T}{\partial x_k} - \rho \widetilde{T' u_k'} \frac{\partial \tilde{u}_i}{\partial x_k}$$

$$G_{it} = -\beta g_i \rho \overline{T'^2}$$

The convection term and production term can be retained in their exact form, while the diffusion terms (D_{ij}^t, D_{it}^t), the pressure-strain interaction terms (Φ_{ij}, Φ_{it}), and the dissipation rate ($\varepsilon_{ij}, \varepsilon_{it}$) need to be modelled.

The diffusion terms are modelled with the assumption that the rate of transport of the second order moments by diffusion is proportional to its gradients, which can be expressed as follows

$$D_{ij}^t = C_s \frac{k}{\varepsilon}\left(\widetilde{u_k' u_m'} \frac{\partial \widetilde{u_i' u_j'}}{\partial x_m}\right)$$

$$D_{it}^t = C_{st} \frac{k}{\varepsilon}\left(\widetilde{u_i' u_k'} \frac{\partial \widetilde{u_j' T'}}{\partial x_k} + \widetilde{u_j' u_k'} \frac{\partial \widetilde{u_i' T'}}{\partial x_k}\right)$$

The dissipation rate is modelled using simple isotropic model:

$$\varepsilon_{ij} = \frac{2}{3}\varepsilon\delta_{ij}$$

$$\varepsilon_{it} = 0$$

The pressure-strain interaction term is one of the most important terms in the transport equation, but the most difficult one to model accurately. Its effect is to redistribute energy amongst the normal Reynolds stresses ($i=j$) so as to make them more isotropic and to reduce the Reynolds shear stresses ($i \neq j$). The simplest representation of the pressure-strain term can be given by

$$\Phi_{ij} = -C_1 \frac{\varepsilon}{k}\left(\rho \widetilde{u_i' u_j'} - \frac{2}{3}k\delta_{ij}\right) - C_2\left(P_{ij} - \frac{2}{3}kP_{kk}\right)$$

More information on the pressure-strain term can be found in the paper by Launder et al. [59]. In STAR-CCM+, two methods are provided to model the pressure strain term, which will be discussed in section 3.3.3.

3.3 Numerical Method in this study

The commercial code STAR-CCM+ is a general Computational Fluid Dynamics (CFD) code based on finite volume method (FVM). The continuous governing equations are discretised into a form that can be solved numerically. STAR-CCM+ provides two approaches to solve the discretised governing equations, i.e. the segregated approach, and the coupled approach.

The coupled approach solves the flow equations for mass and momentum simultaneously. This method is more robust in solving flows with dominant source terms, as well as in solving compressible flows. Another advantage is that the convergence rate is less sensitive to mesh refinement.

The segregated approach solves the flow equation in a segregated/uncoupled manner, i.e. one for each component of velocity and one for pressure. The Predictor-corrector method is used to link the momentum and continuity equation with a SIMPLE-type algorithm. The segregated approach is suitable for incompressible flows or compressible flows at low Mach number.

In this thesis, the coupled approach is found to converge faster than the segregated approach in some cases. A proper ramp of the Courant number is necessary in order to reduce the number of iterations. However, the segregated solver sometimes achieves better convergence than the coupled solver. It is suggested to adopt segregated solver when convergence issues arise.

3.3.1 Mesh Structure

As the fluid is flowing either upward or downward, a 2-D axisymmetric mesh is used, which significantly reduces the computational cost. Since the geometry and flow conditions for these two chosen experiments were different, the meshes were developed separately for each experiment. The primary mesh parameters for both CO_2 study and H_2O study are summarized in Table *3*.

Table 3 Primary Mesh Parameters

Experiments	Heated Length (Unheated)	D	Radial × Axial	RGR [1]	y+
CO_2	1.94m (0.89m)	8mm	32 × 1415	1.0	y+ ≈ 30 [*]
			79 × 1415	1.2	y+ < 0.2
			106 × 1415	1.2	y+ < 0.06 [**]
H_2O	2m (0.63m)	25.4mm	78 × 1315	1.2	y+ < 0.2
			87 × 1315	1.2	y+ < 0.02 [**]
			78 × 2630 [#]	1.2	y+ < 0.2

1: Radial Growth Ratio (RGR) is the ratio of thickness of a cell layer to its previous layer in the near-wall refined region;
*: for the assessment of performance of high y+ wall treatment, see section 5.1.5;
**: for mesh sensitivity study of y+ value, see section 5.1.1;
#: for mesh sensitivity study of axial refinement, see section 5.1.1.

For CO_2 flow, the heated portion is 1.94m long preceded by an unheated section with a length of 0.89m. The reason for this unheated part is to ensure that the flow entering the heat section was hydro-dynamically developed and free of entrance effects. Two fine meshes were developed specifically for simulations with low y+ (or all y+) wall treatment, while the coarse mesh (see Figure *14*) was developed for those with high y+ wall treatment.

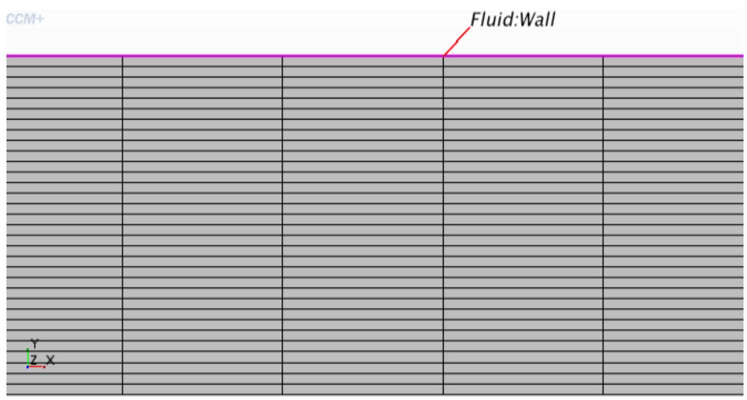

Figure 14 Coarse Mesh with y+ ≈ 30 for CO_2

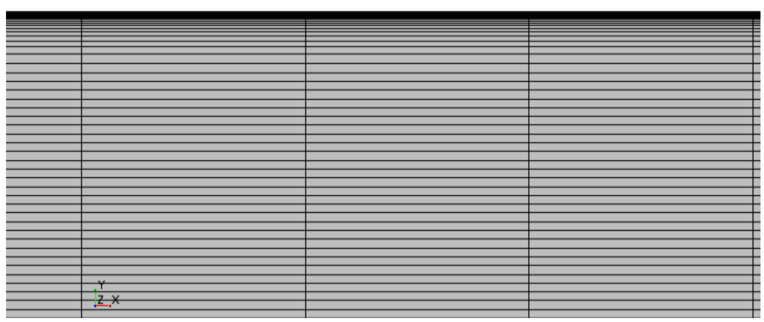

Figure 15 Fine Mesh with y+ < 0.2 for CO_2

The primary mesh used in the study of CO_2 is the fine one with y+ < 0.2. The computational domain was discretized into a mesh of grid with 79 nodes in radial direction and 1415 nodes in axial direction. The mesh was compressed in the radial direction towards the wall, and the y+ value of the wall-cell centroid is always less than 0.2 even at the highest Reynolds number, see Figure *15*. Another fine mesh with y+ < 0.06 was developed for the sensitivity mesh study of the y+ value as shown in Table *3*.

Similarly, for H_2O flow, the computational domain which consists of a heated region of 2m and an unheated region of 0.63m was discretized into 78 × 1315 (radial × axial) grids. The y+ of the wall-cell centroid was also adjusted to satisfy y+ < 0.2 for all the experimental conditions. Two finer meshes were also developed for the mesh sensitivity study, one for radial refinement and the other for axial.

3.3.2 Fluid Properties

The IAPWS-IF97 models in STAR-CCM+ for the calculation of the water properties are only valid within certain ranges of temperature and pressure. The SCWR operates at supercritical pressure which is not supported in the current version of built-in thermodynamic properties. However, STAR-CCM+ provides various methods for specifying user defined thermodynamic properties, e.g. constant, field function, temperature polynomial, and the option to input tabular data from a file. The thermodynamic properties of CO_2 and H_2O used in this study are defined by the author using data from NIST Standard Reference Database 23 (NIST REFPROP version 9.1) [6].

Density and specific heat were defined using temperature polynomials, while the dynamic viscosity and thermal conductivity were provided in the form of tables. It is important to note that the pressure drops in this study are very small (less than 0.02 MPa in a test run), compared to the system pressures. Therefore, for computational convenience the properties were indexed as a function of temperature at constant pressure. It was also verified in the later sensitivity study of pressure. However, if the pressure drop was significant, e.g. in a study of critical flow discharge [60], it is necessary to provide the CFD codes with 2-D (temperature and pressure) tables for all the fluid properties.

Since the thermal properties vary dramatically in the vicinity of T_{pc}, the temperature intervals are refined in that region for polynomials and tables of properties, see Figure *16* and Figure *17*. The number of temperature intervals and range of temperature are summarized in Table *4*.

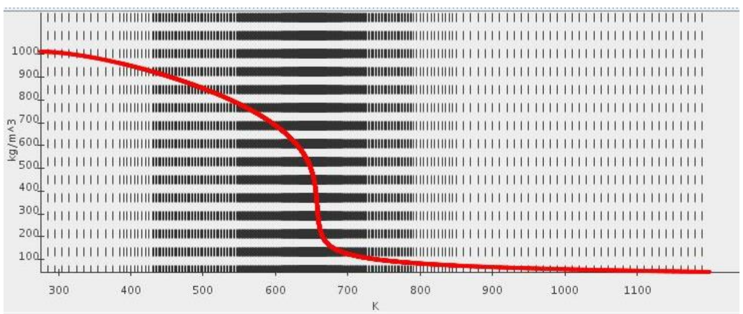

Figure 16 Screenshot of temperature polynomials for H_2O density in STAR-CCM+

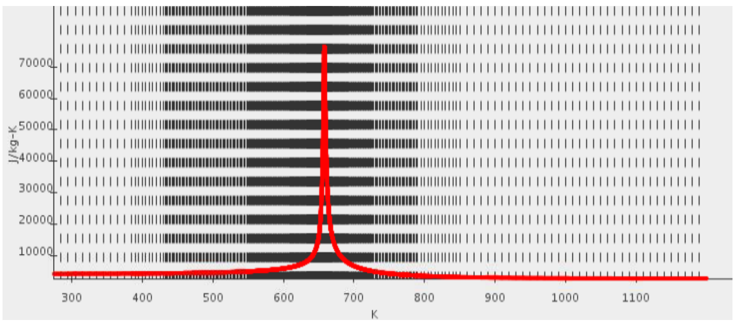

Figure 17 Screenshot of temperature polynomials for H_2O specific heat in STAR-CCM+

Table 4 Parameters of user defined thermodynamic properties

	Pressure (MPa)	Range of Temperature (K)	Number of Intervals
CO_2	7.53	230 to 500	684
		275.15 to 475.15	1102 *
	8.50	230 to 930	499
	8.64 #	230 to 930	499
	8.32 #	230 to 930	499
H_2O	25.0	275 to 1200	815
		275 to 658.04	925 *

*: for the sensitivity study of number of temperature intervals, see section 5.1.2;
#: for the sensitivity study of pressure, see section 5.2.3;

3.3.3 Selected Turbulence Models in STAR-CCM+

The turbulence models examined in this study are listed in Table *5*, which includes several two-equation k-ε, k-ω models, and the second order Reynolds Stress Transport (RST) model. The k-ε models selected are Standard k-ε model by Jones and Launder [61] with three choices of wall-treatments (wall function high y+, two-layer all y+, low-Re all y+), Realizable k-ε by Shih et al. [62] with two choices of wall treatments (wall function high y+, two-layer all y+), and AKN low-Re model by Abe et al. [63] (AKN). The V2F low-Re model was found to have a convergence problem in this study, thus will not be discussed here. The k-ω models chosen are Standard k-ω model by Wilcox, and SST k-ω model by Menter [57] (SST).

Table 5 Selected Turbulence Models in STAR-CCM+

	Wall-Treatment		***Name of Turbulence models***
First Order Two-equation	k-ε	Wall Function (high y+)	Standard k-ε (SWF) Realizable k-ε by Shih et al. (RWF)
		Two-Layer (all y+) 1	Standard k-ε with two-layer approach (STO) Realizable k-ε with two-layer approach (RTO)
		Low-Re (all y+)	AKN low-Re model by Abe et al. (AKN)* Standard low-Re by Lien et al. (SLR)* V2F low-Re (V2F) 2
	k-ω	all y+	Standard k-ω model by Wilcox (WI1, WI2)# SST model by Menter (SST)*
Second Order	Two-Layer (all y+)		Reynolds Stress Transport (RST)*

1: The all y+ wall treatment is a hybrid treatment that attempts to emulate the high y+ wall treatment for coarse meshes, and the low y+ wall treatment for fine meshes;

2: Results are not presented because of convergence issue;

#: WI1: most recent version; WI2: NO Cross-diffusion Limiter, NO Vortex-Stretching Modification;

*: Turbulence models chosen for both CO_2 and H_2O study, the rest are for CO_2 only.

The general descriptions of the above turbulence models have already been presented in section 3.2. A few more comments on some the turbulence models are added below based on the User Guide of STAR-CCM+ [64].

1. *Standard k-ε model with wall function (SWF)*

The Standard k-ε model in STAR-CCM+ is a standard version of the two-equation models. The transport equations are of the form suggested by Jones and Launder [61], with coefficients suggested by Launder and Sharma [52]. The values of these coefficients can be found in section 3.2.4.

2. *Realizable k-ε model with wall function (RWF)*

The Realizable k-ε model is developed by Shih et al. [62] more recently. This model has a new transport equation for turbulent dissipation rate ε. Different from standard model, the coefficient C_μ of this model is expressed as a function of mean flow and turbulent properties, rather than constant in the standard model. The concept of a variable C_μ is consistent with experimental observations in the boundary layers. Thus, this model is substantially better than the standard k-ε model for many applications, and according the user guide, it is able to give solutions that are at least as accurate as the standard model.

3. *Standard low-Re k-ε model (SLR)*

The Standard low-Re k-ε model was developed by Lien et al. [65]. This model has identical coefficients to the Standard k-ε model, but provides more damping functions which let it be applied in the viscous sublayer. The damping functions f_μ, f_1, f_2 which are for model constants C_μ, C_1, C_2, respecitively, can be written as follows:

$$f_\mu = \left[1 - \exp(-0.0198 Re_y)\right]\left(1 + \frac{20.5}{Re_y}\right)$$

$$f_1 = 1, f_2 = \left[1 - 0.3\exp({Re_T}^2)\right]$$

where $Re_y = \frac{y\sqrt{k}}{v}, Re_T = \frac{k^2}{v\varepsilon}$. This model is recommended for natural convection problem.

4. *AKN low-Re k-ε Model (AKN)*

AKN low-Re k-ε Model which is developed by Abe et al. [63] uses different coefficients than the Standard k-ε model, and different damping functions than the Standard low-Re model. The damping functions and model constants are listed as follows

$$f_\mu = \left[1 + \frac{5}{Re_T^{0.75}}\exp(-\left(\frac{Re_T}{200}\right)^2)\right]\left(1 - \exp(-\frac{y^*}{14})\right)^2$$

$$f_1 = 1, f_2 = \left[1 - 0.3\exp({Re_T}^2)\right]$$

$$C_\mu = 0.09, \sigma_k = 1.90, \sigma_\varepsilon = 1.40, C_{1\varepsilon} = 1.50, C_{1\varepsilon} = 1.90$$

where $y^* = \frac{y}{\nu}(\nu\varepsilon)^{0.25}, Re_T = \frac{k^2}{\nu\varepsilon}$. Besides, the Kolmogorov velocity scale, i.e. $u_\varepsilon = (\nu\varepsilon)^{1/4}$, is used instead of the friction velocity $u_t = \sqrt{\tau_w/\rho}$.

This model is recommended for complex flow with low Reynolds numbers.

5. *k-ε models with two-layer approach (STO & RTO)*

Two models of this type are chosen in this study, i.e. Standard k-ε with two-layer approach (STO), and Realizable k-ε with two-layer approach (RTO). The coefficients in these two models are identical to those in their original models, but they gain added flexibility of an all y+ wall treatment after combination with the two-layer approach (details can be found in section 3.2.4).

6. *Wilcox k-ω Models (WI1 & WI2)*

As mentioned earlier, the biggest disadvantage of standard k-ω model (its original form) is that the boundary layer computations are sensitive to the value of ω in the free stream. The standard k-ω model by Wilcox included in STAR-CCM+, has been modified in an attempt to address this shortcoming.

Wilcox revised his original model in 1998 [54], then in 2008 [66], to account for several perceived deficiencies, including a revised set of model coefficients, two corrections to account for sensitivity to the free stream and inlet conditions, a low-Reynolds number correction, a compressibility correction, and a correction to improve the free-shear-flow spreading rates. These corrections have all been included as different options in STAR-CCM+. And the revised set of model constants that are used in STAR-CCM+ are:

$$\gamma_1 = 0.52, \beta_1 = 0.072, \beta^* = 0.09, \sigma_k = 2.0, \sigma_\omega = 2.0$$

The most recent version of Standard k-ω model (WI1) is used in this thesis with all these above corrections, which means “Cross-diffusion Limiter in the Free-Shear”, and “Vortex-Stretching Modification” are activated, and the “Realizability Option” is set to “Durbin Scale Limiter”.

However, it was found WI1 did not converge well at higher heat fluxes. The older version (WI2) without “Cross-diffusion Limiter in Free-Shear” and “Vortex-Stretching Modification” is also compared which is found to converge much better than WI1.

7. *SST k-ω model by Menter (SST)*

Details about the SST model have been shown in section 3.2.5. It is also worth noting that STAR-CCM+ implemented the low-Reynolds number modifications which can be used by any k-ω model. It provides properties with which the user can control the damping modification. The model constants are modified as follows:

$$\beta^*_{1,low-Re} = \beta^* \frac{4/15 + \left(Re_T/Re_\beta\right)^2}{1 + \left(Re_T/Re_\beta\right)^2}$$

$$\gamma_{1,low-Re} = \alpha_1 \frac{\alpha_0 + Re_T/Re_\omega}{1 + Re_T/Re_\omega} \frac{1}{\alpha_1^*}$$

$$\alpha^*_{1,low-Re} = \beta^* \frac{\beta_1/3 + Re_T/Re_k}{1 + Re_T/Re_k}$$

However, this modification is disabled by default, and it is not needed for low y+ wall treatment, only for transitional flows. Hence, it is not activated in all the low y+ type simulations of the present study, but activated in all the high y+ type ones. Furthermore, it is found that this modification does not improve the prediction of HTD, and only small discrepancies of the results can be noticed between models with and without the low-Reynolds number modification.

8. Reynolds Stress Transport Model

RST model available in STAR-CCM+ is ε-based RST (εRST), as another model equation for the scalar dissipation rate ε is solved in addition to the six Reynolds stress transport equations. It uses the same equation for ε as the one used in the standard k-ε model.

STAR-CCM+ provides two methods to model the pressure strain term, i.e. Linear Pressure Strain Model by Gibson et al. [67], and Quadratic Pressure Strain Model by Speziale et al. [68]. The Quadratic Pressure Strain model is a more modern formulation, however, it can only be used with high y+ wall treatment, i.e. using wall functions without resolving the viscous-affected region. Hence, it is unsuitable for the simulation of supercritical fluids in this study.

The Linear Pressure Strain model uses a classic approach to model the pressure-strain term, splitting it up into a slow (return-to-isotropy) term, a rapid term, and a wall-reflection term. It can be used with both high y+ wall treatment and two-layer approach. The same two-layer approach by Rodi [53] is used as the one in two-layer k-ε models.

Thus, RST model with Linear Pressure Strain method incorporated into a two-layer formulation is used in this thesis, aiming to better resolve the viscous sublayer.

4. Experimental Investigation

Two independent experiments by Zahlan et al. [7] and Watts [32] are numerically simulated in this study to assess the performance of different turbulence models in predicting the HTD. The main reason for choosing these two experiments is that in both experiments significant HTD was observed at relatively low mass flux where the buoyancy effect may be the dominant HTD mode. On the other hand, there is an important difference between these two experiments, i.e. in Zahlan's experiments, $T_b<T_{pc}<T_w$, while in Watts's, $T_b<T_w<T_{pc}$ (discussed later). These two experiments are summarized in this chapter.

4.1 Supercritical Carbon Dioxide Flow

The experiments by Zahlan et al. [7] were carried out at University of Ottawa in a supercritical loop using CO_2. The test section used was a circular pipe made of Inconel 600, and was mounted vertically with CO_2 flowing upward. It had an inner diameter of 8mm, wall thickness of 1mm. The test section had a heated length of 1.94m, preceded by an unheated section of 0.89m.

The reported tests were performed over wide ranges of flow conditions at high subcritical and supercritical pressure regions, including the conditions of main interest to SCWR. In their report, not only the measurements heat transfer at supercritical pressures was presented and discussed, but also the measurements of critical heat flux and film boiling wall temperatures at high subcritical pressures. For supercritical heat transfer, the results are presented in three different aspects, i.e. pressure effect, mass flux effect, and heat flux effect, see Figure *18* to Figure *20* respectively. The experimental HTC is presented in a normalized form as h/h_j, where h_j is the value calculated by the modified Dittus-Boelter type equation: $\mathrm{Nu}_b = 0.021 Re_b^{0.8} Pr_b^{0.4} \left(\frac{\rho_w}{\rho_b}\right)^{0.3} \left(\frac{\overline{C_p}}{C_{pb}}\right)^n$(see [17]).

Two peaks of wall temperature were observed when studying the pressure effect, and it was found that with increasing pressure, both peak temperatures decreased and both peak locations moved downstream, see Figure *18*. The study of mass flux effect was carried out at relatively high mass flux where the HTC shows significant enhancement, see Figure *19*. For the heat flux effect, the results showed that at relatively low mass flux and high heat flux the wall temperature presented two peaks which moved upstream with increasing heat flux, see Figure *20*. It was also observed that the upstream peak was sharp and narrow, while the downstream one was much less pronounced.

The experimental data from the study of heat flux effect is of main interest in this present study, as the data showed how HTD evolved with increasing heat flux and can thus be used to study the response of different turbulence models to the onset of HTD. However, a few cases from pressure and mass flux study are also selected to examine the numerical sensitivity to these parameters relative to the sensitivities observed in experiments.

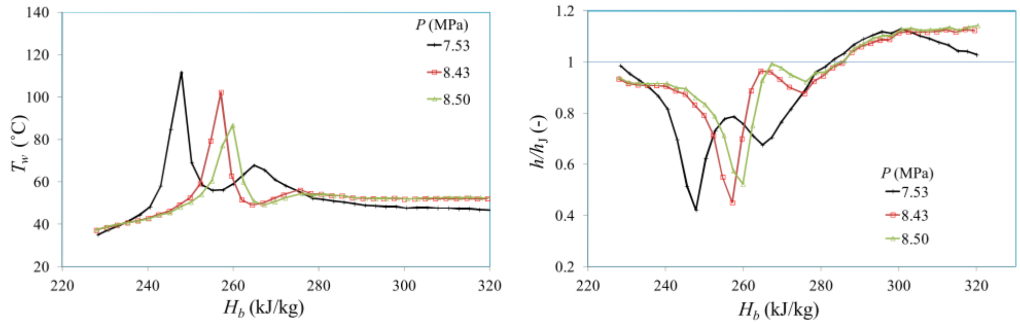

Figure 18 Pressure effect in CO_2 experiments, G = 510 ±10, kg/m^{2}s, q = 50 ±0 kW/m^2, T_{in} = 11.7 ±2.0°C *[7]*

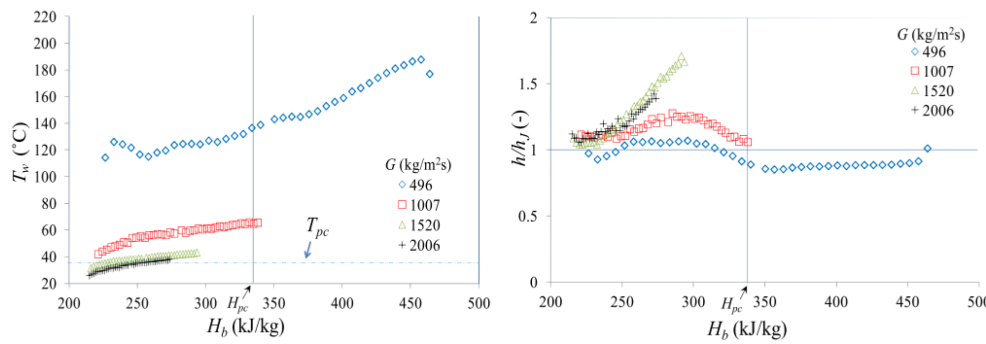

Figure 19 Mass flux effect in CO_2 experiments, P = 8.33 ±0.18 MPa, q = 125 ±0 kW/m^2, T_{in} = 8.5 ±0.4°C *[7]*

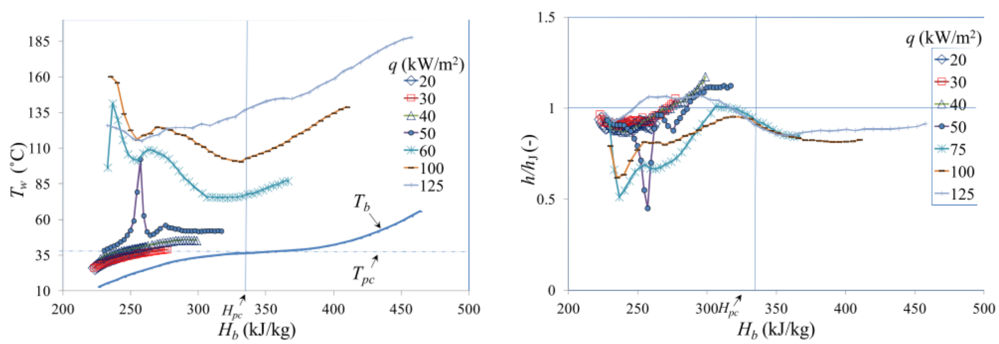

Figure 20 Heat flux effect in CO_2 experiments, P = 8.48 ±0.16 MPa, G = 505 ±12 kg/m^{2}s, T_{in} = 12.0 ±1.4°C *[7]*

All the simulated experimental conditions are listed in Table *6*. The Reynolds number *Re* and buoyancy parameter *Bo** were calcuated along axial using bulk fluid properties, but only the inlet and outlet are shown. The fomula of *Bo** is first introduced by Jackson and Hall [10], and can be written as follows

$$Bo^* = Gr^*/(Re^{3.425}Pr^{0.8})$$

where the Grashof number $Gr^* = \frac{g\beta D^4 q_w''}{k\nu^2}$.

Table 6 Simulated flow conditions in Zahlan's experiments for CO_2

P MPa	T_{in} ºC	q_w kW/m^2	G kg/m^{2}s	Re_{in}	Bo^*_{in}	Re_{exit}	Bo^*_{exit}
7.53	11.7	50*	510	46141	8.73E-07	106960	1.03E-06
8.5	12.0	30	505	44708	5.32E-07	69493	5.30E-07
	12.0	40	505	44708	7.09E-07	82142	7.05E-07
	12.0	50*	505	44708	8.87E-07	98120	8.06E-07
	12.0	75*	505	44708	1.33E-06	145282	4.86E-07
	12.0	100*	505	44708	1.77E-06	182343	2.04E-07
	12.0	125*	505	44708	2.22E-06	197092	9.62E-08

Note: At pressure of 7.53MPa, T_{pc}=31.9ºC; at pressure of 8.5MPa, T_{pc}=37.37ºC;
*: Cases where HTD was observed in experiments.

Mikielewicz et al. [69] suggested a threshold for the buoyancy induced HTD to be $Bo^*>5.6\times10^{-7}$. The calculated buoyancy parameters show that the threshold of HTD in this experiments is around 8×10^{-7}, which is fairly close the value suggested by Mikielewicz. It is also noticed that the Bo^* varies significantly from inlet to outlet, and the peak of Bo^* profile is often located somewhere between the inlet and outlet of the heated section. Hence, it is suggested to find the minimum and maximum of Bo^*, rather than simply calculate the inlet and outlet value.

Yamagata also suggested a criterion for the occurance of HTD based on the ratio of heat flux to mass flux, i.e. $q/G^{1.2}>0.2$. The calculated results in this study showed large discrepancy compared to the value suggested by Yamagata, thus are not shown here. This is attributed to the difference in fluid properties between water and CO_2, because this criterion is based on experimental data on supercritical water, rather than CO_2.

4.2 Supercritical Water Flow

Watts's experiments [8] [32] were conducted at University of Manchester in the late 1970s on the forced and mixed convection heat transfer to water. The main test section in the loop was a vertical stainless steel pipe, which has a diameter of 25.4mm and a heated length of 2m. An unheated length of 0.78m was also located upstream the test section. The operating pressure of the fluid was 25 ± 0.1MPa (T_{pc}=384.9ºC). 20 thermocouples were placed on opposite sides of the pipe to obtain two complete axial wall temperature profiles, which coincide with the thickest and thinnest lines of the pipe respectively. One side of the pipe was about 0.25mm thicker than the opposite side. Therefore the thicker side has the slightly higher heat flux which leads to the slightly higher wall temperature. However, the obtained wall temperature profiles for two sides were almost the same, and the pipe was treated as "uniformly heated" by using the average heat flux.

In Watts's experiments, there were 11 sets of data. A set of observations was taken with the same inlet temperature and heat flux, but over a range of mass flux. HTD was observed at relatively low mass flux. Figure *21* shows the plot of one set of these experimental data. We can clearly see that all the wall temperature curves lie below the T_{pc} line. Though, for Watts's experiments, the main interest is in cases where the peak temperature is less than T_{pc}, there are still a few cases where the wall temperature exceeds the T_{pc} (Figure *22*). Those cases are also investigated, as turbulence models exhibit very different performance in those cases. All the simulated experimental flow conditions are summarized in Table *7*, all are upward flows.

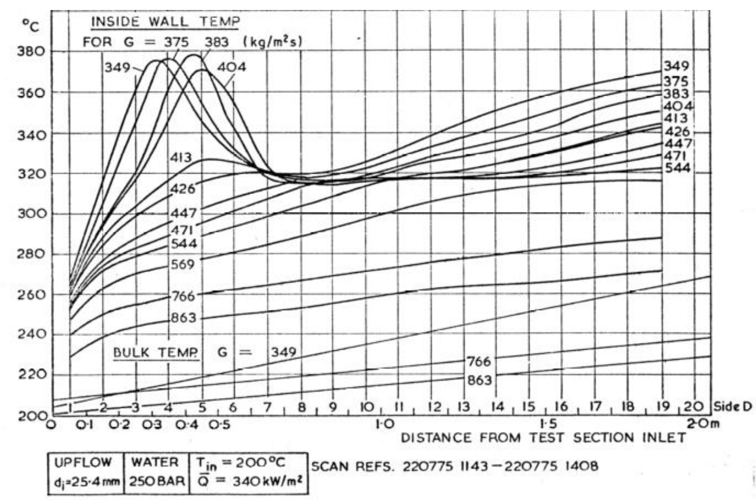

Figure 21 Watts H_2O data - Axial wall temperature distribution (T_b<T_w<T_{pc})

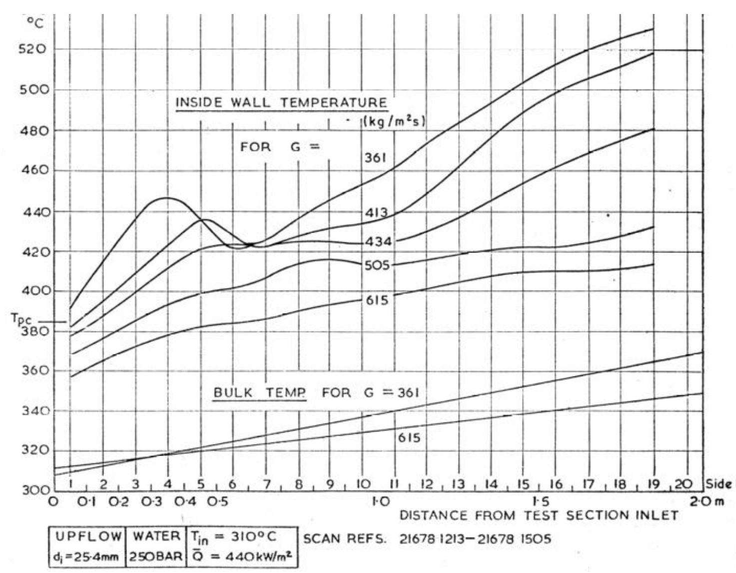

Figure 22 Watts H_2O data - Axial wall temperature distribution (T_b<T_{pc}<T_w)

Table 7 Simulated flow conditions in Watts's experiments for H_2O

T_{in} °C	q_w kW/m²	G kg/m²s	Re_{in}	Bo^*_{in}	Re_{exit}	Bo^*_{exit}	$q/G^{1.2}$	*Purpose of Study*
150	175	278*	37414	4.60E-06	49348	4.37E-06	0.20	Turbulence models
		326*	43874	2.67E-06	55854	2.55E-06	0.17	
150	250	273*	36741	6.99E-06	53579	6.54E-06	0.30	$T_b<T_w<T_{pc}$ Mass Flux Effect Study
		295*	39702	5.36E-06	56589	5.03E-06	0.27	
		325*	43740	3.85E-06	60685	3.63E-06	0.24	
		341*	45893	3.26E-06	62864	3.08E-06	0.23	
		367*	49392	2.54E-06	66404	2.40E-06	0.21	
		382	51411	2.21E-06	68440	2.10E-06	0.20	
150	340	364*	48989	3.55E-06	71872	3.32E-06	0.29	$T_b<T_w<T_{pc}$
200	175	232*	41995	8.09E-06	53247	7.88E-06	0.25	$T_b<T_w<T_{pc}$ Mass Flux Effect Study
		261*	47245	5.41E-06	58517	5.27E-06	0.22	
		280*	50684	4.25E-06	61967	4.15E-06	0.20	
		299	54123	3.39E-06	65420	3.32E-06	0.18	
		326	59011	2.52E-06	70322	2.47E-06	0.17	
200	250	269*	48693	6.96E-06	64721	6.77E-06	0.30	$T_b<T_w<T_{pc}$
		340*	61545	3.12E-06	77620	3.04E-06	0.23	
200	340	349*	63174	3.88E-06	84959	3.78E-06	0.30	$T_b<T_w<T_{pc}$ Mass Flux Effect Study
		375*	67881	3.04E-06	89681	2.95E-06	0.28	
		383*	69329	2.82E-06	91131	2.75E-06	0.27	
		404*	73130	2.35E-06	94953	2.29E-06	0.25	
		426	77112	1.96E-06	98952	1.91E-06	0.24	
250	340	392*	88964	2.54E-06	111035	2.56E-06	0.26	T_w crosses T_{pc} Turbulence models
		411*	93276	2.16E-06	115286	2.18E-06	0.25	
250	400	394*	89417	2.94E-06	115681	2.98E-06	0.30	
		410*	93049	2.56E-06	119226	2.59E-06	0.30	
310	440	361*	104118	4.41E-06	143967	4.89E-06	0.38	$T_b<T_{pc}<T_w$ Turbulence models & Mass Flux Study
		413*	119116	2.78E-06	157114	3.02E-06	0.32	
		434*	125173	2.35E-06	162616	2.53E-06	0.30	
		505	145650	1.4E-06	181709	1.48E-06	0.25	

Re, Bo^*, *and* $q/G^{1.2}$ are calculated by author; *: Cases where significant HTD occurs.

It can be seen the Bo^*_{in} threshold for the occurrence of HTD varied from 2×10^{-6} to 4×10^{-6} between different sets of experiments, dependent on T_{in} and q_w, and the values are very different from that of the CO_2 experiments as calculated earlier. Yamagata's criterion $q/G^{1.2}>0.2$, seems to predict the occurrence of HTD fairly well in some sets of the Watts water data.

5. Results and Discussion

In this chapter, numerical simulations are carried out over a wide range of experimental conditions for CO_2 and H_2O. In order to gain a deeper insight into the heat transfer behaviour at supercritical pressures (especially HTD and its threshold), a set of simulations are performed with increasing heat flux for CO_2, and another sets of simulations with increasing mass flux for H_2O.

The performance of turbulence models in predicting the HTD is investigated under different flow conditions. The mechanism of HTD is discussed for both CO_2 and H_2O using several turbulence models (RST, SST, and SLR) in various flow conditions.

Before starting the main results, the results of sensitivity studies are presented and discussed in the section 5.1, including the sensitivity studies of mesh, fluid property, turbulent Prandtl number, and gravitational orientation. All these sensitivity studies uses a low y+ type mesh with y+<1, as it is believed in order to predict the heat transfer of supercritical fluid the viscous sublayer need to be properly resolved.

The sensitivity of boundary conditions, i.e. heat flux, mass flux, pressure, and inlet temperature, are discussed separately in section 5.2.2 and 5.2.3 after the main results, as they are closely related to the main results. The performance of high y+ wall treatment is also studied, and the results are shown in section 5.1.5.

5.1 Verification and Validation

5.1.1 Mesh Sensitivity

As discussed in section 3.3.1, the mesh parameters in this study are selected based on the previous experience and literature review. However, in order to be assured that the obtained results in this study are mesh-independent, i.e. the mesh is sufficiently fine, a mesh sensitivity study is carried out for both axial direction and radial direction. The mesh parameters for CO_2 and H_2O studies can be found in Table *3*.

For mesh in the CO_2 study, the y+ sensitivity is checked by comparing the primary mesh (y+<0.2) with an even finer mesh (y+<0.06). Three different turbulence models, i.e. AKN, SLR and RST, are selected for this study. The simulated flow condition is at T_{in}=11.7ºC, G=510kg/m^{2}s, q=50kW/m^2, P=7.53MPa, where significant HTD is observed. The results are shown in Figure *23*. It can be seen that the y+<0.2 curves (solid lines) and y+<0.06 curves (dash lines) only show small discrepancies for all three models. Therefore, the mesh with y+<0.2 is believed to be sufficiently fine in this study.

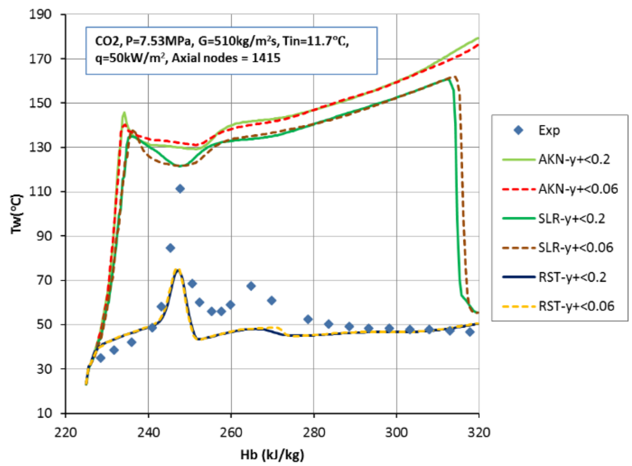

Figure 23 Sensitivity study of y+ value for CO_2

For mesh in the H_2O study, a similar y+ sensitivity study is carried out by comparing the primary mesh (y+<0.2) with the mesh that has y+<0.02. The mesh sensitivity for axial direction is also checked by doubling the number of axial nodes, i.e. comparing the primary mesh (1315 nodes axially) with a finer mesh that has 2630 nodes in axial direction. Three experimental conditions with different mass fluxes but same other boundary conditions are selected for the y+ sensitivity study, while two of them are chosen for the mesh sensitivity study in axial direction. Only the SLR model is used, and the results are shown in Figure *24* and Figure *25* respectively. It can be seen from Figure *24* that all the y+<0.02 curves fall onto the y+<0.2 ones, except for the case in which the code predicts a second temperature peak (G=325kg/m^{2}s). In fact, the second peak here is very sensitive to other parameters too (discussed later), thus we will focus on the first temperature peak in this mesh selection section. For the axial direction, the temperature curves predicted by the finer mesh (2630 nodes) perfectly fall onto that by the mesh with 1315 nodes for all the flow conditions (Figure *25*). Putting aside the sensitive second temperature peak, it can be concluded that the mesh is sufficiently fine for this H_2O study.

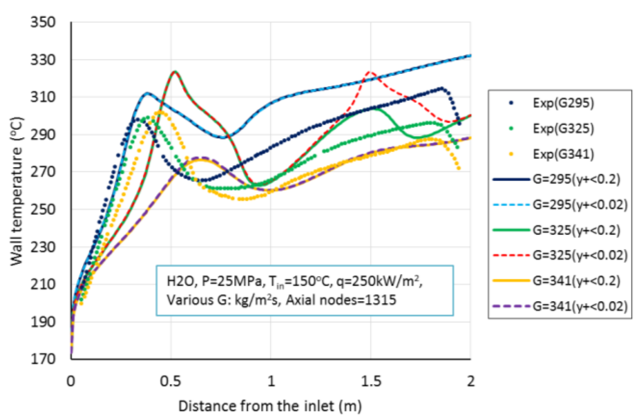

Figure 24 Sensitivity study of y+ value for H_2O by SLR

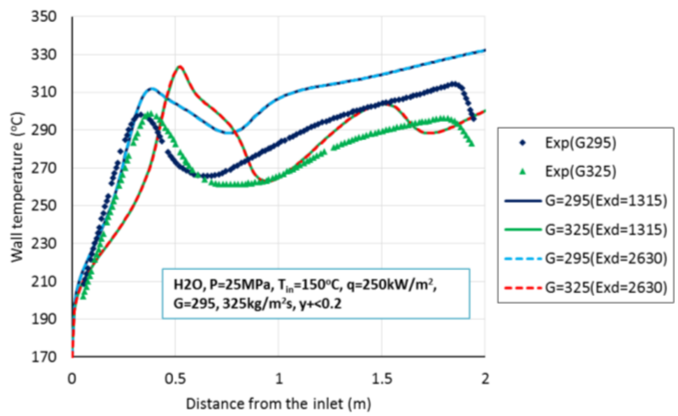

Figure 25 Sensitivity study of number of nodes in axial direction for H_2O by SLR

5.1.2 Sensitivity of the Number of Temperature Intervals for Fluid Properties

As discussed earlier, all the fluid properties were indexed as a function of temperature only. Density and specific heat were defined using polynomials of temperature, meanwhile dynamic viscosity and thermal conductivity were provided in the form of tables. In order to accurately represent the sharp changes in fluid properties in the vicinity of T_{pc}, the temperature intervals of these properties are refined in that region. The parameters are summarized in Table *4*.

However, it is still necessary to check the properties discretization dependence, as increasing the number of temperature intervals can capture more details of the variation of fluid properties which may result in more accurate results, but will also appreciably increase the time per iteration. A sensitivity study is therefore carried out to decide the right number of temperature intervals for the properties of CO_2, comparing the 684-interval properties and the 1102-interval properties. The results are shown in Figure *26*.

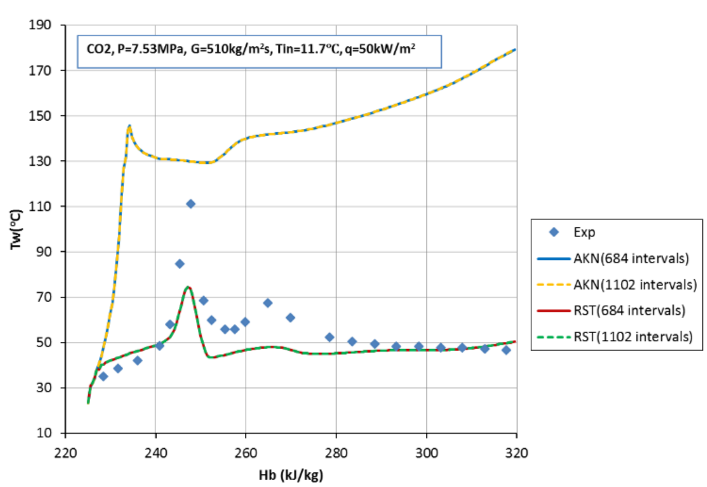

Figure 26 Sensitivity of the number of temperature intervals of fluid properties for CO_2

The same flow condition for CO_2 is selected as that used in mesh sensitivity study, i.e. T_{in}=11.7°C, G=510kg/m^{2}s, q=50kW/m^2, P=7.53MPa. Two turbulence models (AKN and RST) are chosen for this study. It can be seen that the temperature curves of the 1102-interval properties (dash lines) fall perfectly on that of the 684-intervals properties (solid lines). Thus, it can be concluded that the computational results are not sensitive to fluid properties, and it is safe to use the less-fine fluid properties that has 684 temperature intervals.

For the fluid properties in the H_2O study, a similar sensitivity study is carried out by comparing the 815-interval properties and the 925-interval properties. The 925-interval properties covers a smaller range of temperature, i.e. 275K to 658.04K (compared to 275K to 1200K for the 815-interval ones). Two turbulence models (SLR and RST) are used for this study, at one of the lowest mass flux where HTD is observed. The results are shown in Figure *27*. Again, two different sets of fluid properties show almost identical wall temperature distributions. Hence, we can be assured that the thermodynamic properties of supercritical water are sufficiently fine.

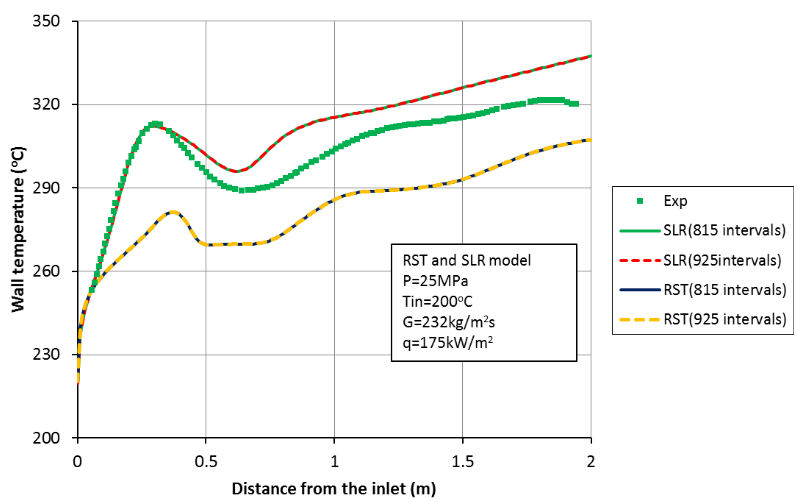

Figure 27 Sensitivity of the number of temperature intervals of fluid properties for H_2O

5.1.3 Turbulent Prandtl Number Sensitivity

As mentioned earlier in chapter 3, the turbulence Prandtl number (Pr_t), is normally taken as constant, and the default value in STAR-CCM+ is 0.9 which is used in this present study. However, in the studies of supercritical fluids, a constant Pr_t of 0.85 was sometimes used by other researchers [45]. Some studies showed that the calculation results are not significantly affected by the choice of Pr_t [70], while some researchers believed that using a constant turbulent Prandtl number will cause the inability of turbulence models in reproducing turbulent heat flux which can partly leads to the failure of predicting the heat transfer in strong-buoyancy-influenced cases [71],. Therefore, it is of interest to examine the sensitivity of Pr_t, and the suitability of the assumption of constant Pr_t.

A sensitivity study of turbulent Prandtl number is carried out by comparing the results of different constant Pr_t, i.e. 0.85, 0.9, 0.95, 1.0, and 1.2, for both CO_2 and H_2O, in various flow conditions with several turbulence models. The results are shown in *Figure 28*, *Figure 29*, *Figure 30* and Figure *31*. It can be seen that the temperature curves of different Pr_t show very small discrepancies in most cases. However, the discrepancies increase in cases just prior to the onset of HTD. It can be seen from *Figure 28* that RST model predicts very different wall temperatures with different turbulent Prandtl numbers. But in cases away from the vicinity of "HTD thresholds" (the minimum heat fluxes that will cause HTD, see section 5.2.2 for detail), the results are much less sensitive to Pr_t (e.g. q=50, 75kW/m^2 in *Figure 29*). It is actually consistent with the later sensitivity studies of boundary conditions in section 5.2.3. *Figure 30* and Figure *31* show the sensitivity of Pr_t in H_2O study using both SLR and RST models. Similar behaviour is also observed. The results are sensitive to Pr_t only for conditions in the vicinity of HTD threshold, e.g. the first peak at mass flux of 341kg/m^2s, and the second peak at mass flux of 325kg/m^2s in *Figure 30*.

It is also notable that the increase in Pr_t will increase the magnitude of deterioration, resulting in a higher peak temperature. Hence, better results can be achieved by tuning the Pr_t, especially in the vicinity of HTD threshold. Nevertheless, the author believes it is inappropriate to tune the Pr_t freely to reproduce the experimental data, as there are many other factors that may lead to the discrepancies between measured and code predicted wall temperatures. Therefore, the turbulent Prandtl number Pr_t is set to 0.9 in both CO_2 and H_2O studies. Further investigation on Pr_t in the regime of supercritical pressure is needed.

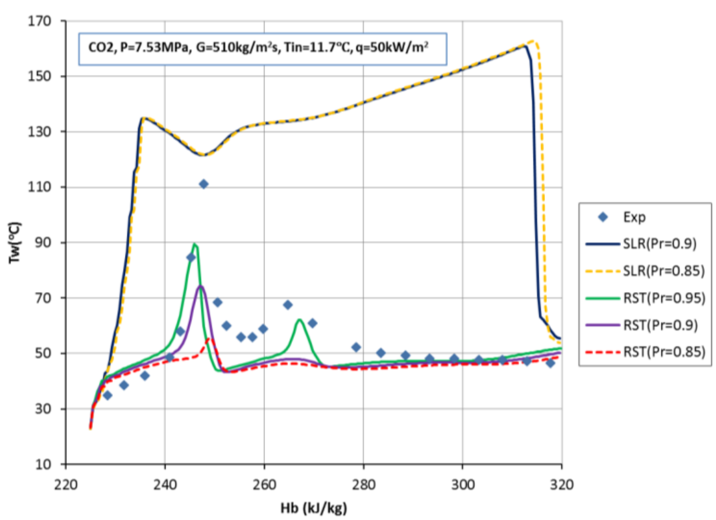

Figure 28 Sensitivity study of Pr_t by SLR and RST models for CO_2

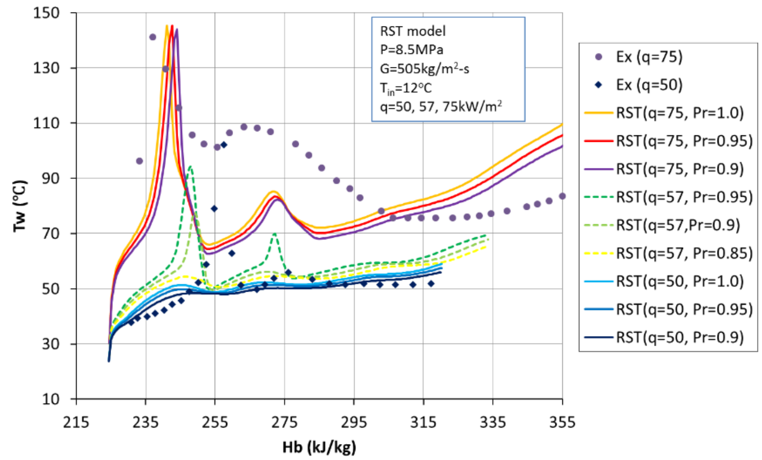

Figure 29 Sensitivity study of Pr_t by RST model for CO_2 in other flow conditions

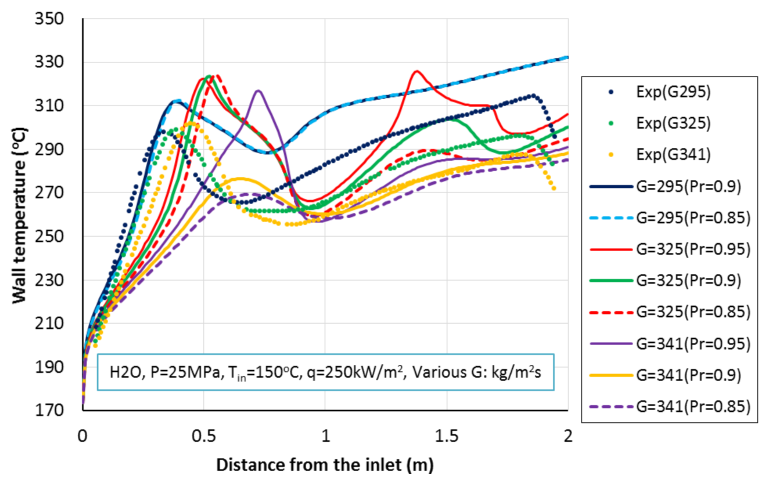

Figure 30 Sensitivity study of Pr_t by SLR model for H_2O

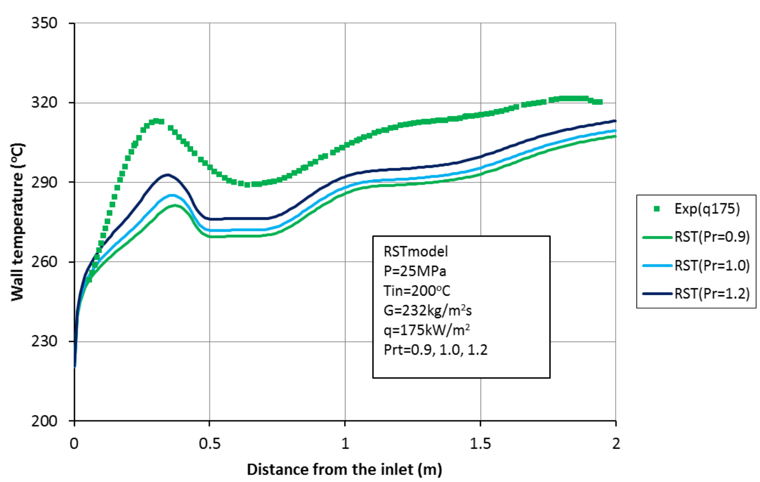

Figure 31 Sensitivity study of Pr_t by RST model for H_2O

5.1.4 Influence of Gravity on Deteriorated Heat Transfer

The buoyancy effect is the primary focus of this study, as the mass fluxes in these two experiments are relatively low and the calculated buoyancy parameters also indicate that the buoyancy force is important. However, in order to prove that the HTD is caused by the buoyancy force, the same equations are solved using identical girds with exact same boundary conditions but without the buoyancy terms in NS equations.

In STAR-CCM+ [64], the buoyancy terms are added by turning on the Gravity model. Once the Gravity model is active, the body force due to gravity can be included in the momentum equations. For variable-density flow, the buoyancy effects due to gravity and density variation are modelled directly and are always presented. For problems using the Constant Density model, the buoyancy effect are only included when the optional Boussinesq model is selected in addition to the Gravity model. In our cases, the fluid density undergoes large variations, thus the Polynomial Density model plus the Gravity model are used. By turning the Gravity model off or using a gravitational acceleration (g) of 0 m/s^2, the buoyancy terms are removed from the NS equations.

Figure *32*, Figure *33* and Figure *34* showed the comparison between upward flow (g= -9.81m/s^2), downward flow (g= 9.81m/s^2), and no-gravity flow (g= 0m/s^2) in three typical cases where HTD was observed using AKN and SST models for both CO_2 and H_2O. It can been seen that in all three cases wall temperatures in downward flow and no-gravity flow were substantially lower than that of upward flow. The temperature increased monotonously with distance and with no predicted peaks, which is consistent with the findings in experiments that the localized peak in temperature did not occur in the downward flows with the same heat flux and mass flux. This implies that the buoyancy terms in the NS equations is responsible for the observed HTD in experiments.

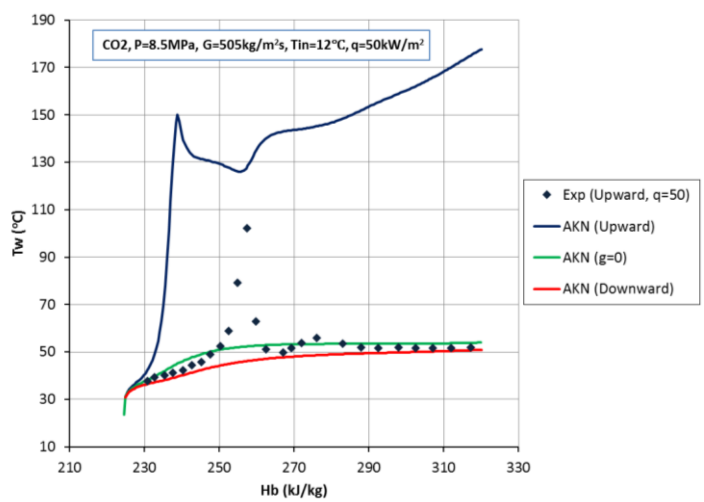

Figure 32 Different options for gravity at low heat flux by AKN model for CO_2

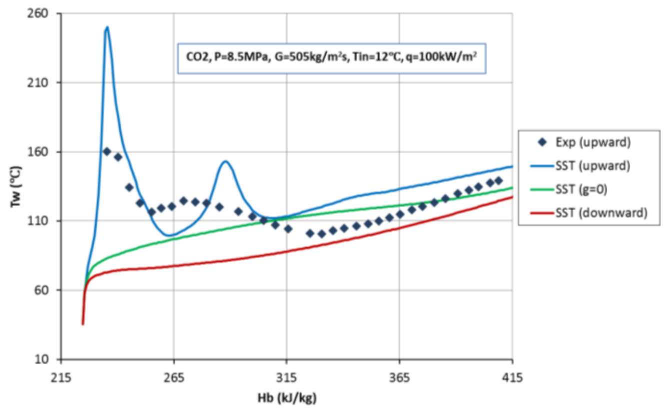

Figure 33 Different options for gravity at high heat flux by SST model for CO_2

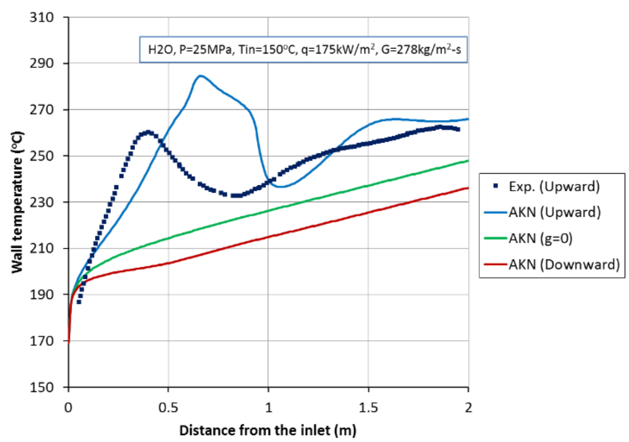

Figure 34 Different options for gravity by AKN model for H_2O

The downward flow predicts a lower wall temperature than no-gravity flow, which is also attributed to the buoyancy force: when the fluid is flowing downward the shear stress in the outer edge will be bigger than that in the absence of buoyancy, thus the production of turbulence will be higher, which leads to the enhancement in heat transfer compared to no-gravity flow. This is consistent with other authors' results as described in Chapter 2.

5.1.5 *Performance of High y+ Wall Treatment*

Although, turbulence models with high y+ wall treatment have a poor reputation in predicting the heat transfer at supercritical pressures, all the turbulence models in STAR-CCM+ that can be applied to a coarse mesh using either high y+ or all y+ wall treatment are assessed at both low and high heat fluxes. The results are shown in Figure *35* and Figure *36*.

The parameters of this coarse mesh can be found in Table *3*. The y+ value of the wall-cell centroid is kept always greater than 20. All the selected turbulence models are summarized in Table *5*. Except for the two k-ε models with wall functions (SWF and RWF), all turbulence models use the all y+

wall treatment instead of the high y+ wall treatment. The all y+ wall treatment is always recommended as it is a hybrid approach that can give very similar results to the low y+ treatment for y+<1, and to the high y+ treatment for y+>30.

It can be seen from Figure *35* that the wall temperature predicted by all models showed no significant peaks. Though, small humps in temperature may be recognized, they are too weak to be considered as HTD. Figure *36* shows the poor performance of these models at relatively high heat flux. It is quite clear that none of the selected turbulence models were able to predict the HTD observed in experiments on a high y+ type mesh. This is actually within our expectations, as the large variations of properties in the near-wall layer should require a great number of grid points to depict the details. Hence, the following discussions are based on the low-Reynolds number type meshes (y+<0.2) with either low y+ or all y+ wall treatments.

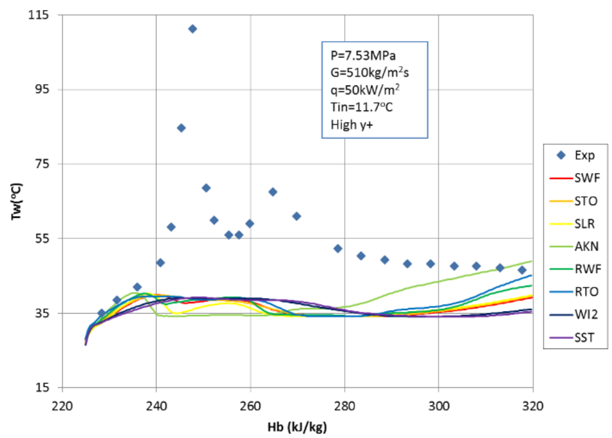

Figure 35 Performance of high y+ wall treatment at relatively low heat flux

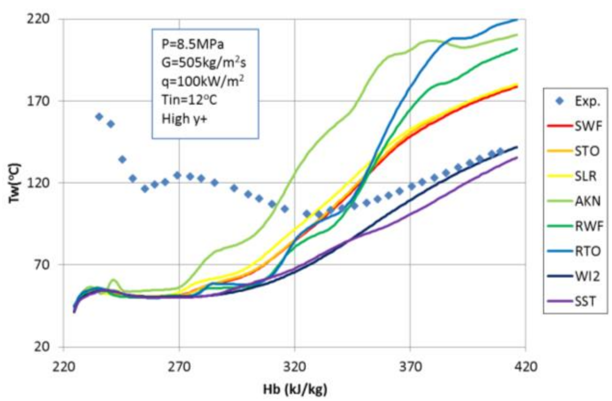

Figure 36 Performance of high y+ wall treatment at relatively high heat flux

5.2 Supercritical CO_2 Flow

5.2.1 Wall Temperature Predicted by Different Turbulence Models

As mentioned ealier in the experimental investigation, the data of heat flux effect from CO_2 experiment is of main interest of this study, as it can be used to learn how and when those turbulence models respond to HTD. In experiments, the HTD was observed at heat flux between 40 and 50kW/m^2, the corresponding buoyancy parameters are 7.09×10^{-7} and 8.87×10^{-7} (see Table *6*).

Figure *37* to Figure *40* showed the wall temperature distribution predicted by different turbulence models (the meaning of abbrevations can be found in Table *5*). It can be seen that the performance of these turbulence models varied significantly. All the models can reproduce the wall temperature very well at low heat flux (q=30kW/m^2) where there is no HTD, see Figure *37*. However, discrepancies increase at higher heat fluxes in the presence of HTD.

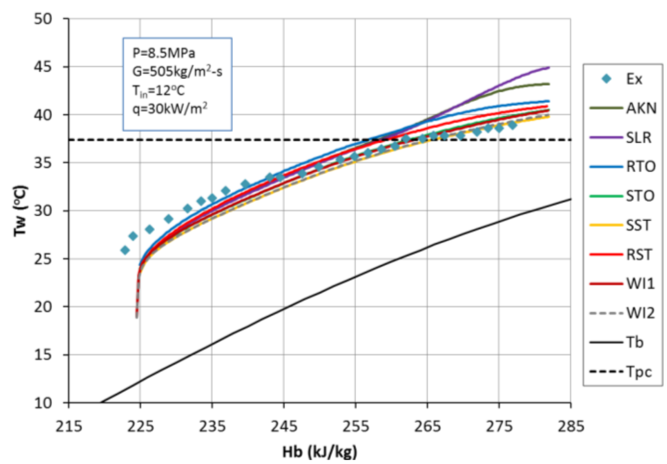

Figure 37 Axial wall temperature distribution at heat flux of 30kW/m^2

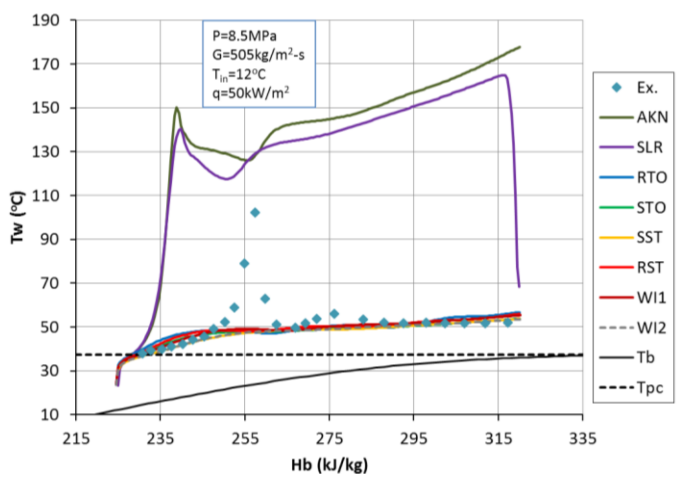

Figure 38 Axial wall temperature distribution at heat flux of 50kW/m^2

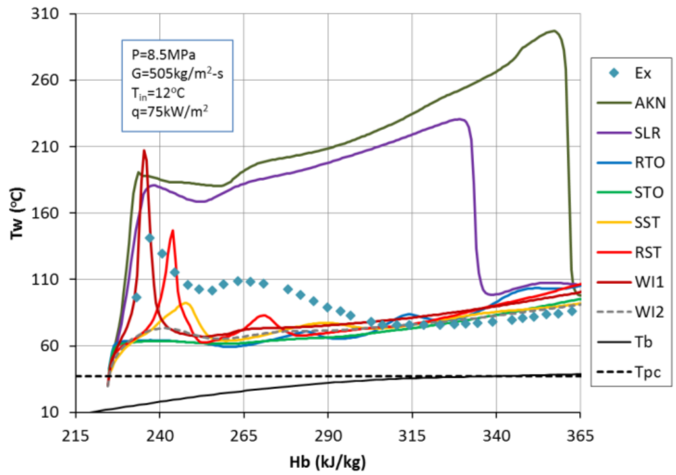

Figure 39 Axial wall temperature distribution at heat flux of 75kW/m^2

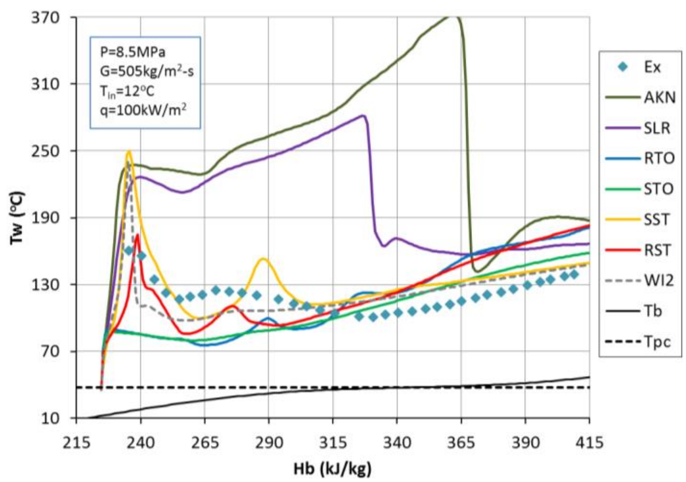

Figure 40 Axial wall temperature distribution at heat flux of 100kW/m^2

The two k-ε models with two-layer approach, i.e., RTO and STO, fail to predict HTD in all the cases, even at the highest heat flux. Similar behavior was also found in Ambrosini's study [44].

The two low-Re models, i.e. AKN and SLR models, predict the onset of HTD qualitatively in all cases (Figure *38* to Figure *40*). However, the wall temperatures in these cases are significantly overestimated. Also, it is important to note that both AKN and SLR have trouble recovering the wall temperature after the onset of HTD. This is in fact consistent with the results from other researchers [45] [46] [47]. It seems a common failing of all low-Reynolds number k-ε models when predicting the buoyancy-induced HTD. These low-Reynolds models do predict a gentle recovery of wall temperature following the local maximum point, but it is too weak to be considered as a full recovery. This issue will be discussed later in section 5.3.3 with the discussion of HTD mechanism.

AKN and SLR both predict a steep decrease in wall temperature further downstream where T_b is around T_{pc}, which was not observed in their original studies [45] [46] [47]. Similar behavior was also found in the CO_2 study using same AKN model by He et al. [42]. It is suspected that the relatively short heated length used in the previous literature was insufficiently long and the pseudo-critical temperature was never approached [45] [46] [47], i.e., in those historical works the bulk fluid has not been heated to T_{pc}. In order to confirm this hypothesis, the author modifies a simulation from Sharabi's paper [45] with identical flow conditions but with artificially increased heated lengths, the results of which show consistent response to that discussed above, i.e. same steep decrease in wall temperature occurs further down-stream where the bulk temperature is close to T_{pc}. These results are presented and discussed later in Appendix 1, while the reason are illustrated in section 5.3.3.

Although, SST, RST, WI1 and WI2, all fail to predict the first occurrence of HTD at a heat flux of 50kW/m^2 (Figure *38*), they all start to predict the HTD at higher heat fluxes (Figure *39* and Figure *40*). It can be seen that RST model is able to predict the two temperature peaks observed in experiments both qualitatively and quantitatively. SST model underestimates the peak temperature at heat flux of 75kW/m^2 (Figure *39*) while overestimates the peak temperature at heat flux of 100kW/m^2 (Figure *40*). Similarly, both WI1 and WI2 are able to predict the HTD at high heat fluxes. The most recent version (WI1) predicts the HTD at lower heat flux than WI2, however, it has too-high residuals at heat flux of 100kW/m^2 (the difference between WI1 and WI2 can be found in section 3.3.3). It is worth mentioning that in other studies, k-ω models are often overlooked as the heat fluxes in those cases were not sufficiently high to trigger the response to HTD.

It is quite clear that RST model presents the best performance in predicting the HTD for these conditions. *Figure 41* summarized wall temperatures predicted by RST model in all flow conditions. Except for lowest heat flux where deterioration occurs, the RST model reproduce the wall temperature quite well within the vicinity of HTD. It is also worth noting that RST model tends to over-predict the far downstream wall temperatures where CO_2 transitions into the gaseous state, while SST model seems better in this aspect as seen in Figure *39* and Figure *40*.

Before starting the next section, it is helpful to review the difference among STO, SLR and RST model. STO and SLR models have the identical equations and coefficients from Standard k-ε model. The main difference between them is that STO uses the two-layer approach to resolve the viscous sublayer, while SLR model uses the low-Reynolds number approach. One may suspect that the two-layer approach is mainly responsible for the failing in predicting HTD, but the fact RST model uses the same two-layer approach and all y+ wall treatment as STO model (see section 3.3.3) reveals that something else important is leading to the different behaviors between STO and RST models. Further investigation on this issue is needed.

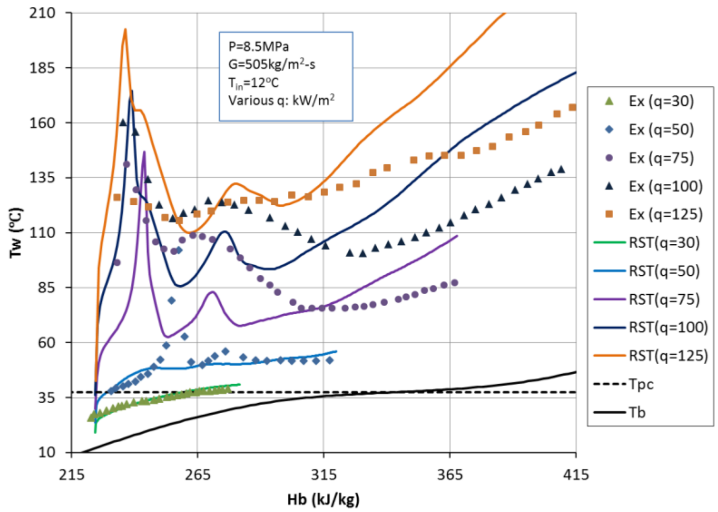

Figure 41 Wall temperature distribution by RST model at various heat fluxes

5.2.2 Sensitivity Study of Heat Flux

After the above discussion, it can be seen that SST and RST models are able to predict the HTD, albeit at higher heat fluxes than observed experimentally. Although, the two low-Re k-ε models, i.e. AKN and SLR, seem better in predicting the first occurrence of HTD at heat flux of 50kW/m^2, they both are deficient in predicting recovery. Besides, it is possible that these low-Re models would respond to HTD at heat fluxes below those observed in experiments. Thus, it is worthwhile to carry out a study on the heat flux sensitivity for these models, to determine the threshold where these turbulence models start predict HTD. The results of this sensitivity study are shown in Figure *42* to Figure *46*. The heat fluxes, after careful adjustment, were set around the threshold where HTD was about to occur, i.e. through trial and error the lowest heat flux where HTD can be observed was determined for each model.

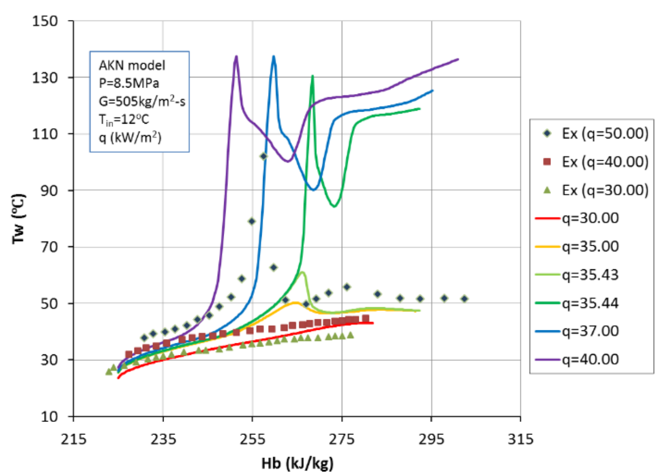

Figure 42 Heat flux sensitivity by AKN model

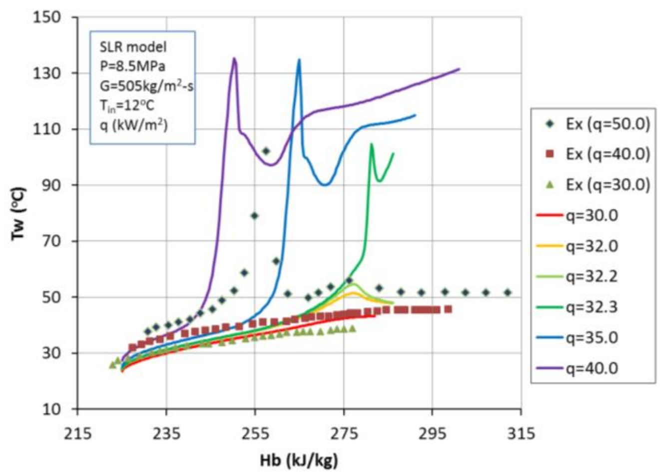

Figure 43 Heat flux sensitivity by SLR model

It is surprising to see from Figure *42* and Figure *43* that both AKN and SLR are extremely sensitive to heat flux in the vicinity of HTD threshold, which could be attributed to the stiffness of non-linear damping functions in the equations. The wall temperature rises abruptly with only a small increase in heat flux (AKN by 0.01kW/m^2 and SLR by 0.1kW/m^2). This seems contrary to experimental observations wherein HTD is much more mild and gradual than dry-out mechanisms in multiphase flows. At heat flux of 40kW/m^2, AKN and SLR predict a significant HTD which was not observed in experiment. Therefore, it is confirmed that they both respond to HTD at heat flux well below those observed in experiments.

SST, RST and WI1 are far less sensitive. From Figure *44*, Figure *45* and Figure *46*, we can see that the temperature peaks gradually rise with increasing heat flux. Although, all three models showed some delay in the response to HTD, they were able to qualitatively predict the deterioration at slightly higher heat fluxes compared to experiments.

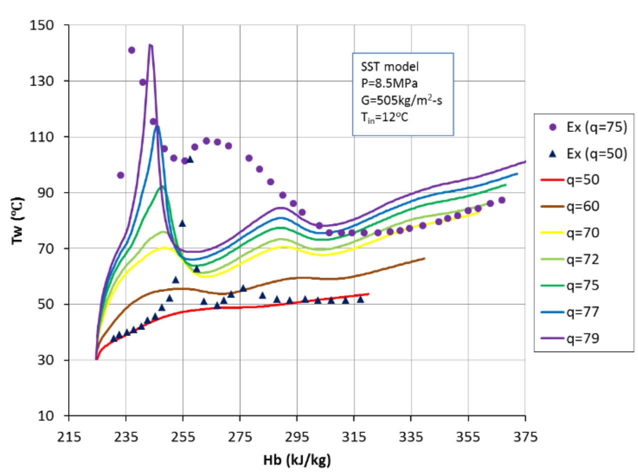

Figure 44 Heat flux sensitivity by SST model

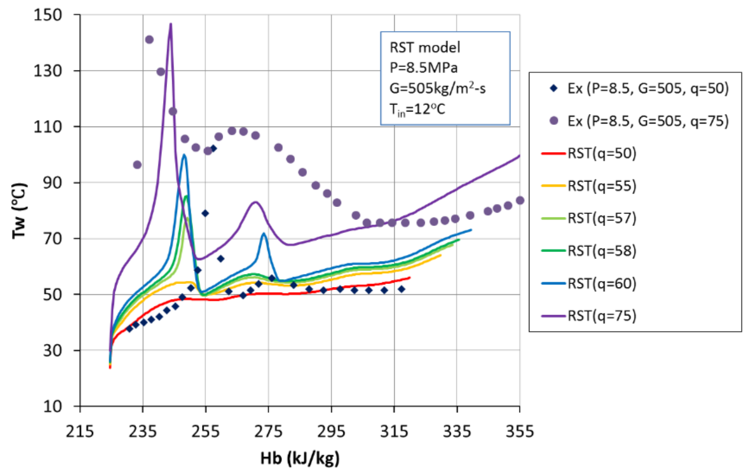

Figure 45 Heat flux sensitivity by RST model

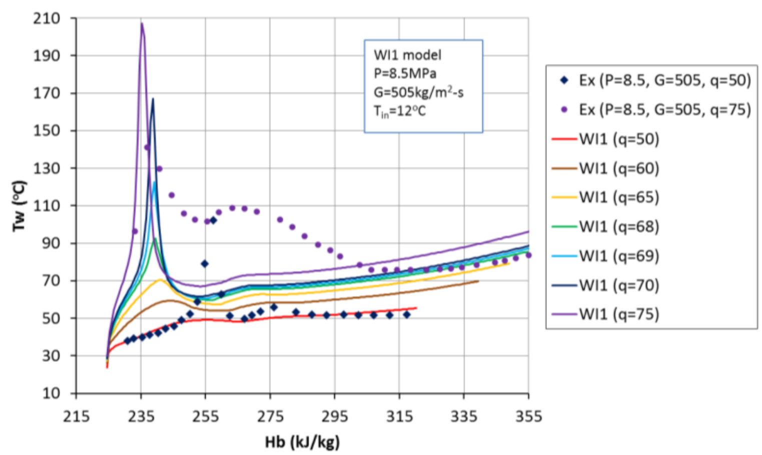

Figure 46 Heat flux sensitivity by WI1 model

Table 8 Threshold heat fluxes of HTD by different turbulence models

Turbulence Models	AKN	SLR	SST	RST	WI1	Exp.
HTD Heat Flux Threshold (kW/m^2)	35.43-35.44	32.2-32.3	70-80	55-60	65-70	40-50

Note: keeping other boundary conditions constant, i.e. P=8.5MPa, G=505kg/m^{2}s, T_{in}=12°C.

Table *8* summarized the heat flux thresholds for HTD by different turbulence models based on the above figures (Note that the way of determining the thresholds here may be highly subjective). It seems that RST model presents the best performance, as it started responding to HTD around 57kW/m^2. The experimental data showed that HTD occurred somewhere between 40 and 50kW/m^2. It would be helpful if more experimental data around HTD threshold were available. It is suggested that the experiments is performed in a manner consistent with those used to detect the first onset of Critical Heat Flux experiments, i.e. the heat flux is gradually increased until the first onset of HTD is observed.

5.2.3 Sensitivity Study of Other Boundary Conditions

The measurements of test section pressure, temperature, and mass flow rate in Zahlan's experiment have small uncertainties. The boundary conditions in the Figure *20* where the data was digitized from also have some uncertainties, i.e. P = 8.48 ± 0.16 MPa, G = 505 ± 12 kg/m^{2}s, T_{in} = 12.0 ± 1.4^{o}C. After realizing how sensitive those turbulence models are to heat flux, it is worthwhile to investigate the sensitivity of other boundary conditions, as an error in the boundary condition when we run a simulation might result in some unexpected effects.

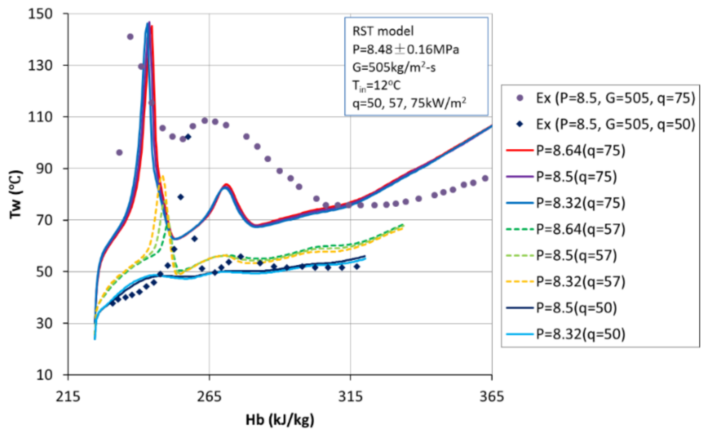

Figure 47 Pressure sensitivity by RST model for CO_2

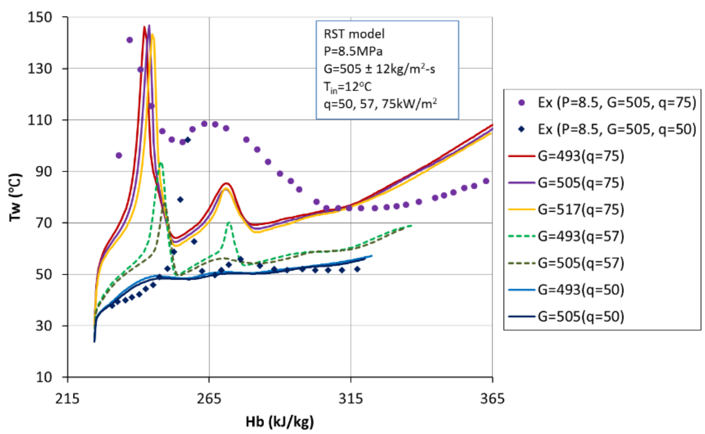

Figure 48 Mass flux sensitivity by RST model for CO_2

Figure *47* and Figure *48* show the sensitivity studies of pressure, and mass flux, using the RST model. It is noteworthy that only in the vicinity of HTD threshold (q≈57kW/m^2), the RST model is sensitive to the pressure and mass flux. A similar study of the SST model has come to the same conclusion. It is in fact consistent with the previous sensitivity studies of turbulent Prandtl number and heat flux. It seems that the predicted heat transfer coefficient is very sensitive to turbulence and boundary conditions in the vicinity of deterioration. An increase in the pressure or mass flux will completely suppress the HTD, while the opposite will increase the predicted effect of HTD. Beyond the vicinity of heat flux threshold, the predicted wall temperatures are far less sensitive to these two boundary conditions.

If we carefully tune the boundary conditions within the ranges of experimental uncertainties, the discrepancies between measured and predicted results may become smaller, e.g. for SST model at heat flux of 75kW/m^2 (see Figure *49*). Nevertheless, it is only effective in matching the experimental results in region near deterioration and in the vicinity of HTD threshold. Similar to the case of turbulent Prandtl number, no tuning is employed for the remainder of the discussions.

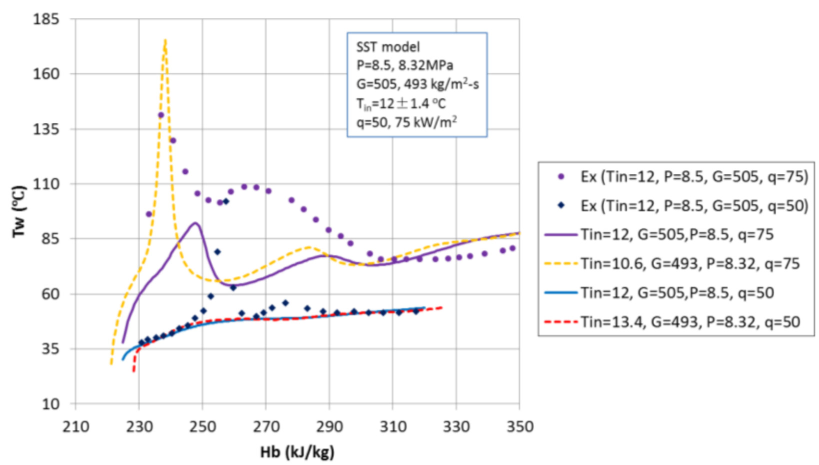

Figure 49 Sensitivity of SST model for CO_2

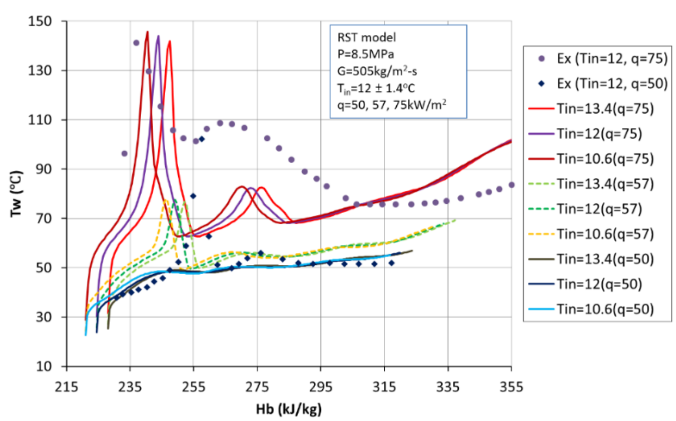

Figure 50 Inlet temperature sensitivity by RST model for CO_2

Figure *50* shows the sensitivity study of inlet temperature. It can be seen that the increase or decrease in T_{in} acts only to shift the temperature profiles right or left without affecting the shape of the temperature distribution. It is important to note that the wall temperature distributions here are plotted against the bulk enthalpy, and the shift in the peak with regards to enthalpy exactly corresponds to the change in inlet enthalpy boundary condition. When plotted against the distance from inlet, the peak location and peak temperature would remain unchanged. This reveals that the onset of HTD in these cases is not dependent on the bulk enthalpy, but rather on the location with respect to the start of the heated length.

Vikhrev et al. [72] found two types of HTD in their experiments: the first type appeared in the entrance region of the tube (L/D≤40-60) and was due to the flow structure within the entrance region; the second appeared at any section of the tube, but only within a certain enthalpy range when the wall temperature exceeds T_{pc}. Although the above definitions of two types of HTD are not enough for their clear identification, the response to the inlet temperature sensitivities RST model presents reveals that the HTD in this study may be due to the flow structure within the entrance region. Detailed discussion on this issue and the HTD mechanism are in the following section.

5.3 HTD Mechanism Study for CO_2

As discussed earlier, there are two main phenomena noted in literature which give rise to HTD, i.e. buoyancy and flow acceleration. As opposed to acceleration-induced phenomenon, the buoyancy-induced HTD usually occurs at low mass flux and only in upward flow. The gravity study in section 5.1.4 indicates that the gravity plays an important role in causing the HTD for the experiments of interest here. Hence, it is believed that buoyancy is responsible for the HTD in this study. Although the mechanism of HTD has already been studied numerically by other researchers, it is still worthwhile to investigate this phenomenon further. After the discussion in the previous sections, the RST model stands out as one of the best performing models, as it is qualitatively and quantitatively better than other turbulence models in reproducing the experimental results and with smaller sensitivities. Hence we adopt the RST model to examine the detailed mechanisms within the flow that give rise to HTD.

It is also notable that most of the existing CFD studies on HTD mechanism were based on low-Re k-ε models under experimental conditions where other models like SST exhibit relatively poor performance, e.g. He [42] [44] investigated HTD mechanism using three k-ε models by Launder & Sharma (LS), Chien (CH), and Abe et al. (AKN); Rosa [73] carried out a similar mechanism study using standard k-ε model by Lien; Sharabi [45] also briefly looked into the HTD phenomenon using k-ε low-Re model by Yang and Shih (YS). Their results all tended to agree with Hall and Jackson's buoyancy theory [14], which depends on the reduction in the rate of production of turbulence, following a modification of the distribution of shear stress across the flow due to the action of buoyancy (see section 2.1.1 for details). While such previous studies provide qualitative information of the mechanisms they also demonstrate rather poor performance in predicting HTD and recovery, hence we adopt the RST model to observe the detailed fluid behaviour near the deterioration location.

Furthermore, these previous two-equation model studies and subsequent mechanism discussions rely on the approximation that the turbulence production and the velocity gradient are positively correlated. As discussed in section 3.2.3, the production term in the governing equation of turbulent kinetic energy, is the multiplication of turbulent shear stress and velocity gradient. The turbulent shear stress, $\rho\overline{u_i'u_j'}$, as mentioned earlier in section 3.2.2, can be estimated using the mixing length model,

$$\tau_T = \rho\overline{u_i'u_j'} = \rho l^2 \left|\frac{\partial \bar{u}}{\partial y}\right| \frac{\partial \bar{u}}{\partial y}$$

which implies that the reduction in total shear stress will directly reduce the turbulent shear stress, and thus the turbulence production. However, as Jackson mentioned recently [15], it is by no means certain that the mixing length will be unaffected by the presence of low density layer; and the use of mixing length model could be inappropriate, as the convection of turbulent kinetic energy may become significant in this present application.

Based on the above, further inspection on this buoyancy theory is still necessary. Here, by using Reynolds Stress Transport Model (often referred to as RST or RSM), the HTD mechanism is studied comprehensively. The results of other turbulence models, i.e. SLR and SST, are also compared. A different perspective on the mechanism of buoyancy-induced HTD is presented.

The case selected for this mechanism study is the one at heat flux of 100kW/m^2 (Figure *40*), where strong buoyancy effects are expected.

5.3.1 RST Model in Upward Flow

The RST model predicts two temperature peaks similar to that observed in experiments, and the second peak is much milder than the first one. The two peaks are plotted against x/D on Figure *52*. It can be seen clearly that the maximum of first temperature peak is located at x/D=18 while the second at x/D=68.

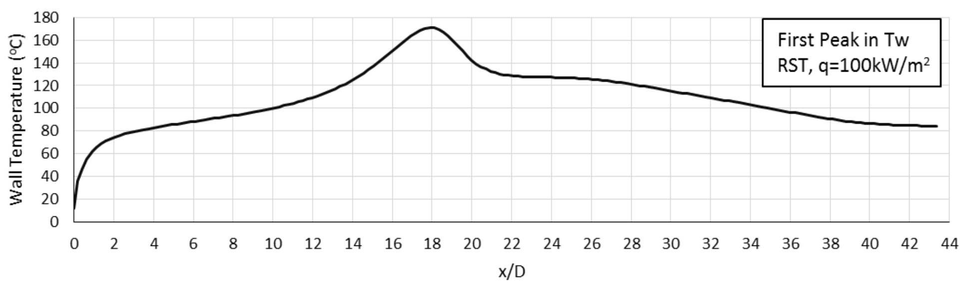

Figure 51 First peak of wall temperature predicted by RST model

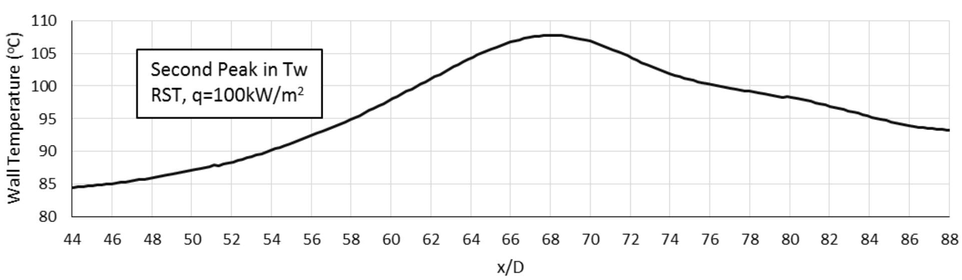

Figure 52 Second peak of wall temperature predicted by RST model

The radial distributions of fluid properties are shown in the following figures. About 20 axial locations are chosen for each peak, 10 upstream of the peak temperature and 10 downstream (corresponding to lines in different colors: the redder, the higher temperature; the more purple, the lower).

- **<u>First peak</u>**

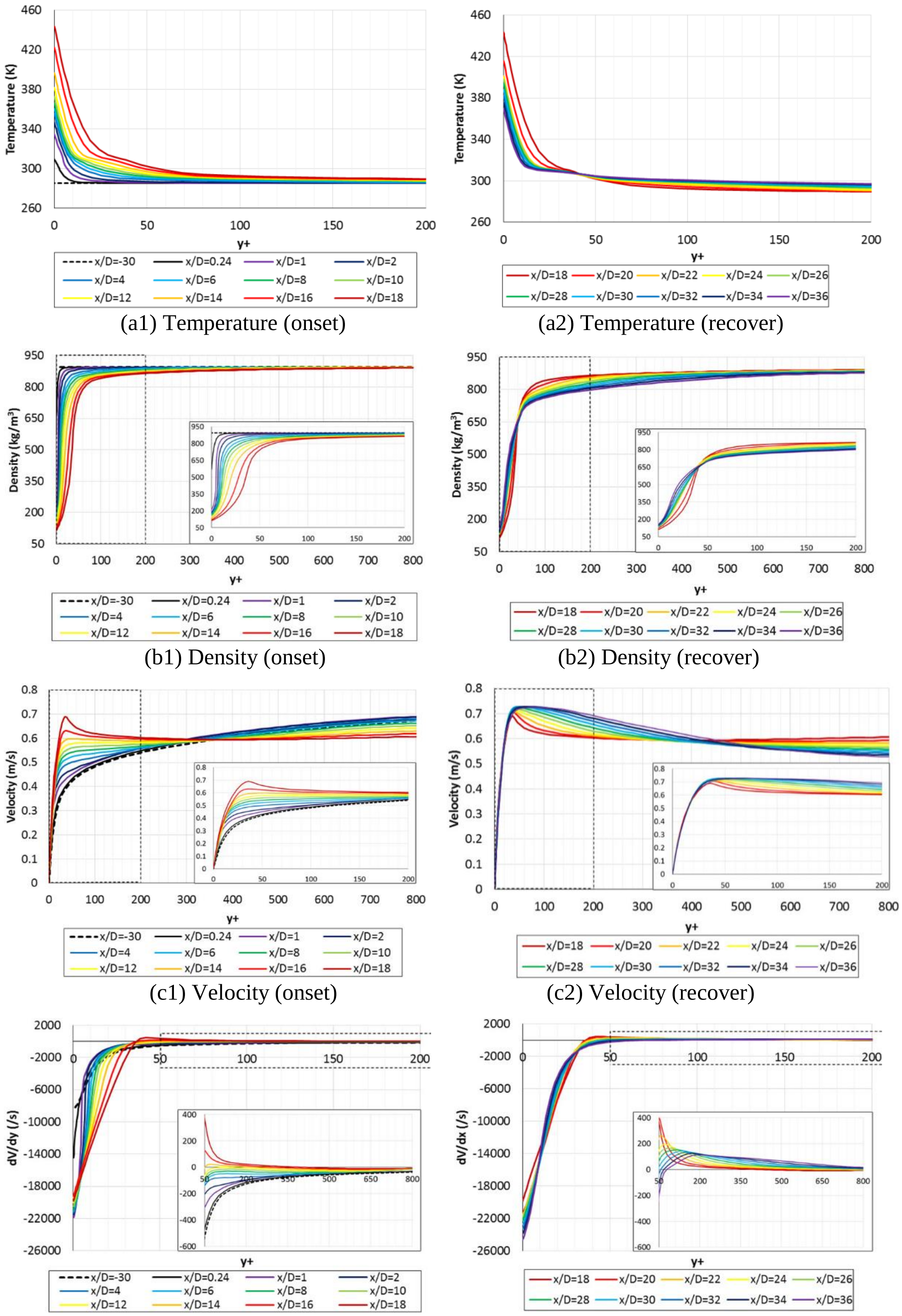

(a1) Temperature (onset) (a2) Temperature (recover)

(b1) Density (onset) (b2) Density (recover)

(c1) Velocity (onset) (c2) Velocity (recover)

(d1) Velocity gradient (onset) (d2) Velocity gradient (recover)

Figure 53 Radial distributions of fluid properties by RST - 1st peak

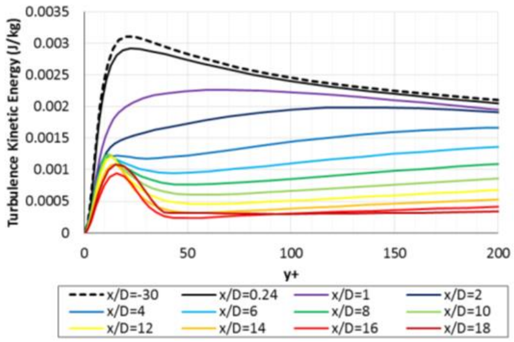

(a1) Turbulence Kinetic Energy (onset)

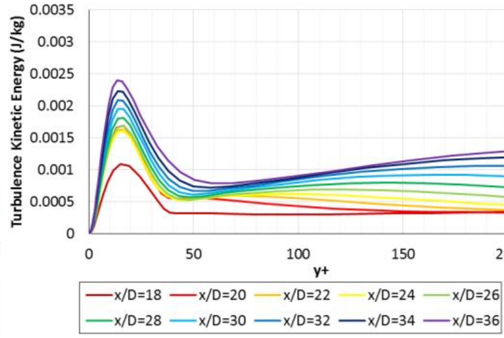

(a2) Turbulence Kinetic Energy (recover)

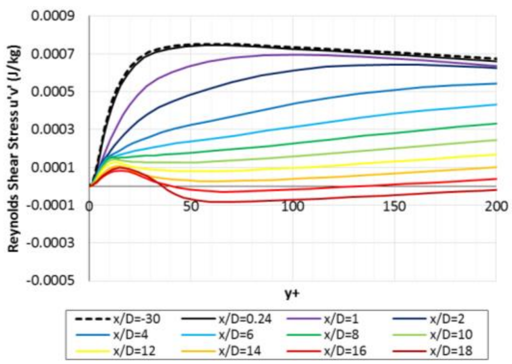

(b1) Reynolds shear stress $u'v'$ (onset)

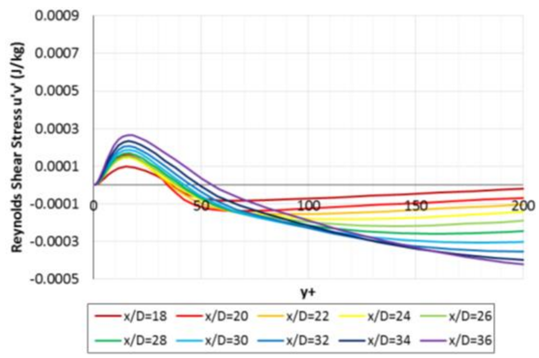

(b2) Reynolds shear stress $u'v'$ (recover)

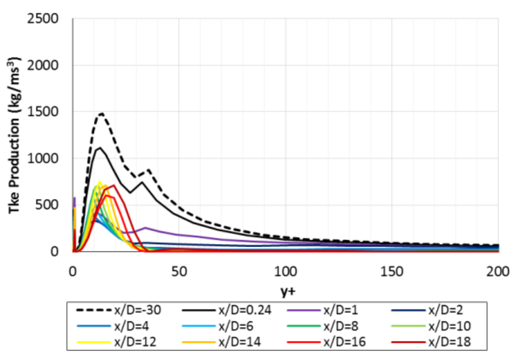

(c1) Tke production (onset)

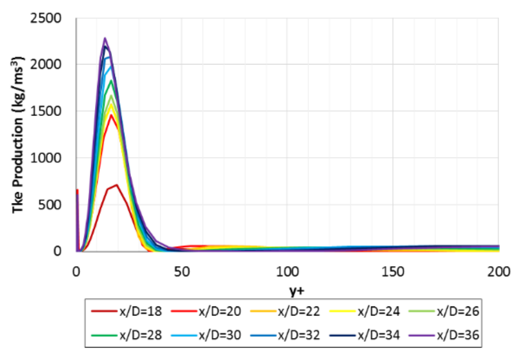

(c2) Tke production (recover)

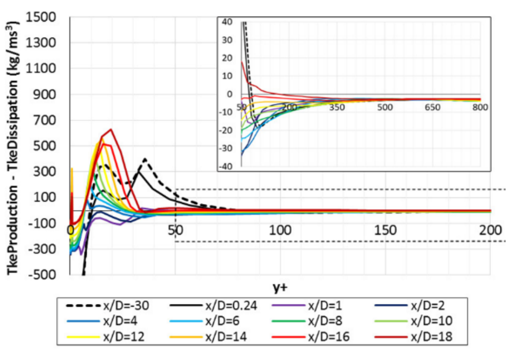

(d1) Tke net production (onset)

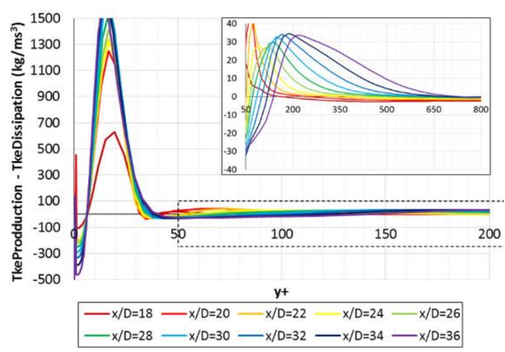

(d2) Tke net production (recover)

Figure 54 Information on the turbulence by RST – 1st peak

1) Before entering the heated section (x/D= -30)

The distributions of fluid properties of fully developed isothermal flow at location of x/D= -30 upstream in the non-heated region, was plotted as references (dash lines). It can be seen that before entering the heated section the velocity increases gradually from the wall to the central line (Figure *53* c1), and the turbulence is mainly generated in the near-wall region (10<y+<60) (*Figure 54* c1). Most of produced turbulence kinetic energy (Tke) dissipates locally. The net production of Tke, i.e. production minus dissipation (*Figure 54* d1), shows that there is a positive area within 10<y+<80 and negative areas in both y+<10 and y+>80, indicating the Tke generated in 10<y+<80 is also transported out to offset the dissipation in the viscous sublayer and core regions.

2) Immediately downstream of the start of heated section (0<x/D<1)

When the flow enters the heated length, it is heated by the wall. In this case, the wall temperature exceeds T_{pc} in a very short distance from the inlet (x/D≈0.2), which implies that the density in the wall-layer will decrease rapidly (Figure *53* b1). When the flow reaches x/D=1, a very thin low-density layer is formed against the wall (y+<5). From Figure *53* c1, we can see that the fluid in this thin layer is immediately accelerated leading to a modified velocity profile. As a result, the shear stress (dV/dy) within 0<y+<5 increases, while that everywhere else (y+>5) decreases (Figure *53* d1). Since the turbulence is mainly generated within 10<y+<80, the decrease in shear stress in y+>5 greatly impairs the turbulence production (Figure 54 c1). It can be seen from *Figure 54* d1, the net production of Tke in 10<y+<80 becomes negative, which indicates that more turbulence is dissipated than generated in this region, which coincidently upstream of the heated length was responsible for most of the turbulence generation. Consequently, Tke starts to decrease (Figure 54 a1) in the vicinity immediately downstream of the start of heated length.

The impairment in turbulence production occurs much earlier than expected, which is very different from what other researchers have documented. Most authors postulate that the low-density layer needs to grow sufficiently thick in order to reduce the turbulence production, and when the low density layer is limited to the viscous sub-layer the turbulence will not be significantly modified. Apparently, what is found here is inconsistent with this historical view. A comparative study in the absence of gravity and with identical flow conditions shows that almost the same acceleration exists near the inlet (results are shown in section 5.3.2). This reveals that the initial reduction in turbulence production is not simply caused by buoyancy, the "entrance effect" (see section 5.3.2) is playing a more important role in redistributing the shear stress and impairing the turbulence production in regions very close to the inlet. It will be shown later that in the absence of gravity turbulence is re-introduced downstream of this initial location, while in the presence of buoyancy turbulence levels are not able to recover.

3) The onset of HTD (1<x/D<16)

As the low-density layer grows thicker (Figure *53* b1), more fluid is accelerated (Figure *53* c1). The shear stress increases further in the near-wall region (y+<30), while it decreases further in the core region (y+>30). Meanwhile the region where shear stress is larger than in unheated flow moves from y+<5 to y+<30 (Figure *53* d1). As a result, turbulence in the buffer layer 10<y+<30 is regenerated at this stage (*Figure 54* c1), and the net production of Tke in that region becomes positive again (*Figure 54* d1). However, the velocity gradient in the core region (y+>30) is further reduced (Figure *53* f1), as the velocity profile becomes more flattened. The Reynolds shear stresses and thus turbulence production (turbulence shear production equals to the multiplication of turbulent shear stress and velocity gradient) in y+>30 continuously decrease to almost zero. Although, at this moment, turbulence is partly regenerated (within 10<y+<30) and Tke is being transported from 10<y+<30 (where net production is positive) to the other regions (where net production is negative), the production is still not sufficient to offset the dissipation (Positive areas < Negative areas). Thus, Tke keeps decreasing especially in the core region (*Figure 54* a1), the peak Tke in the near-wall region is also reduced by a factor of three. The effectiveness of heat transfer is impaired due to the reduction in turbulence (more precisely, turbulent diffusivity of heat).

It is clear that, the growth of low-density layer helps restore the turbulence production within 10<y+<30 (*Figure 54* c1), and because of this regeneration, Tke does not drop to zero in the near-wall region (a small peak is observed within 10<y+<30, see *Figure 54* a1), which makes it quantitatively better than SLR and SST in predicting the peak temperature (for SLR and SST the results are shown in section 5.3.3). What is observed here slightly deviates from the explanation given by other researchers, in which they argue that the buffer layer generation is suppressed and in our case it appears to have been regenerated upstream of the point of deterioration.

For non-gravity flows the same results are shown in section 5.3.2. It shows that in the absence of the buoyancy force turbulent net production within y+>30 remains higher than in the gravity case here, and hence the flow is not dominated by dissipation resulting in a higher Tke in the near-wall region. Therefore, in the non-gravity case the heat transfer is more effective and HTD is avoided.

4) The recovery of HTD (18<x/D<36)

At location of x/D=18, the flow in the near-wall region starts moving faster than that in the core region (mainly due to the buoyancy force exerted on the low-density layer, because in the non-gravity flow case the velocity of near-wall fluid never becomes greater than that fluid in the core region, see section 5.3.2), therefore the low-density layer will exert an upward force on the core fluid by shear. It can be seen from Figure *53* c2, more fluid in the core region next to the fast-moving-low-density layer is being accelerated. The velocity profiles begins to distort into the M-shape as noticed in other studies. In other words, the shear stress in the core region will change its sign (become positive) and begin to increase (Figure *53* d2). This leads to regeneration of turbulence in the core (Figure 54 d2), which upstream of the deterioration point had been dominated by dissipation. Although, the magnitude of this production is quite small, it has a strong impact on the turbulence level, because now more turbulence in the core is being generated than dissipated (Figure 54 d2), thus allowing the total turbulence levels in the flow (in both near-wall and core regions) to be restored (Figure 54 a2). Eventually, the restoration of turbulence (Tke) and turbulent diffusivity (of heat) helps recover the wall temperature. It is notable that the (net) turbulence production in the buffer layer (10<y+<30) quickly rebounds to a level that is two to three times higher during the recovery, while the local shear stress does not change much. It seems that there is a delay in the full recovery of turbulence production within 10<y+<30, as the increase in shear stress in this region occurs much earlier during the onset of HTD (1<x/D<18).

- **<u>Second Peak</u>**

The maximum of second temperature peak is located at x/D=68. Before starting the discussion on the mechanism of the second peak, it is helpful to review the density profile upstream. It can be seen from Figure *53* b1, that the low-density fluid during the onset of HTD (0<x/D<18) is limited to the wall-layer y+<40, while the fluid in the core region remains high-density. Due to the impaired turbulent diffusivity (of heat) in the core region (*Figure 54* a1), this large density difference can be maintained. However, when turbulence is regenerated during the recovery (18<x/D<44), the increase in turbulent diffusivity (*Figure 54* a2) allows better convection of heat from low-density fluid to the high-density fluid, which lowers the temperature of the low-density fluid, and raises that of the high-density fluid, resulting in a smaller density difference (Figure *53* b2). Hence, at the end of the first recovery, the buoyancy force exerted on the low-density fluid has been decreased.

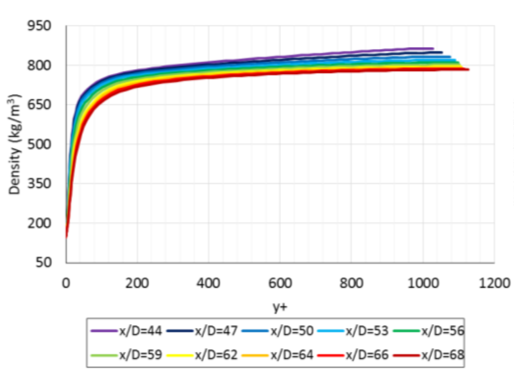

(a1) Density (onset)

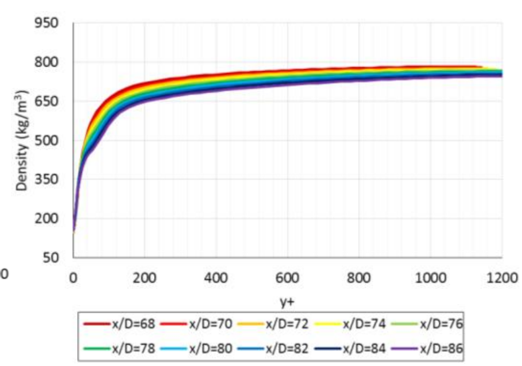

(a2) Density (recover)

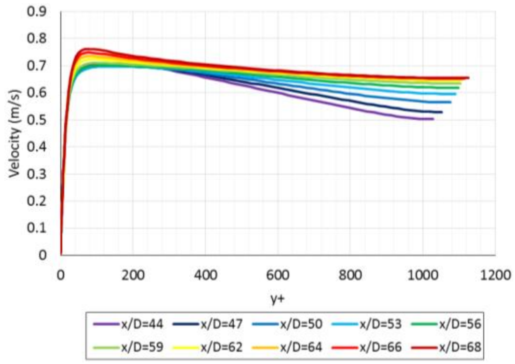

(b1) Velocity (onset)

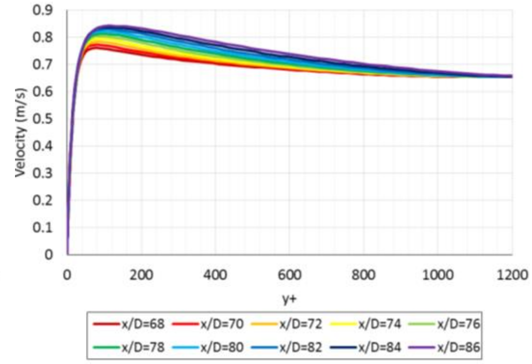

(b2) Velocity (recover)

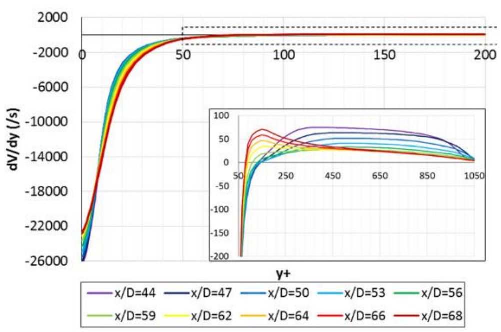

(c1) Velocity gradient (onset)

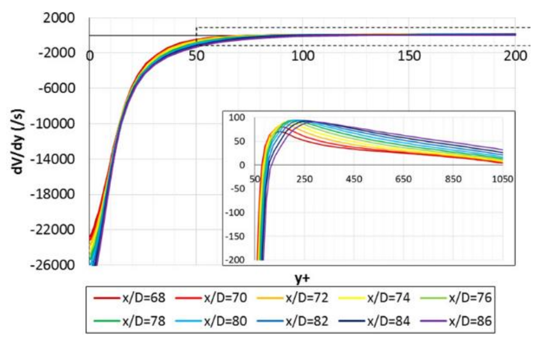

(c2) Velocity gradient (recover)

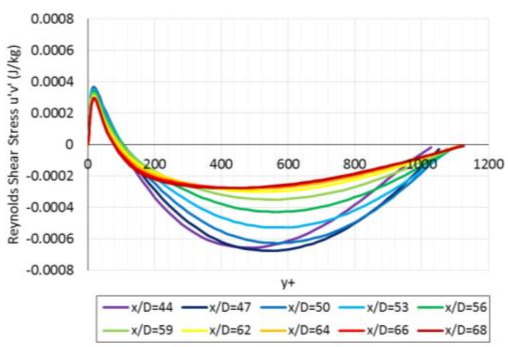

(d1) Reynolds shear stress uv (onset)

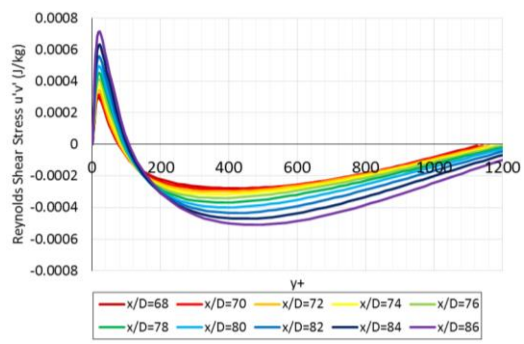

(d2) Reynolds shear stress uv (recover)

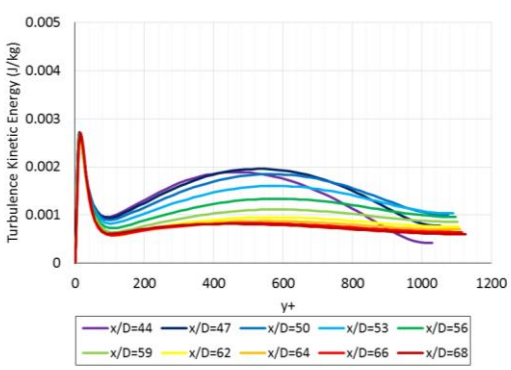

(e1) Turbulent kinetic energy (onset)

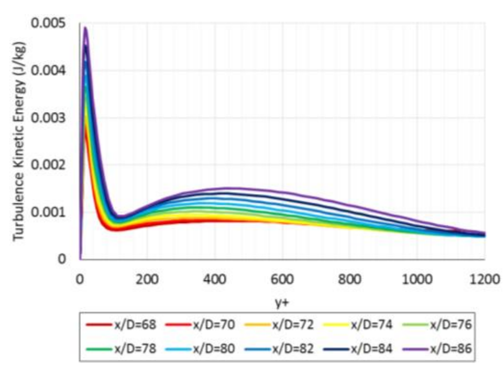

(e2) Turbulent kinetic energy (recover)

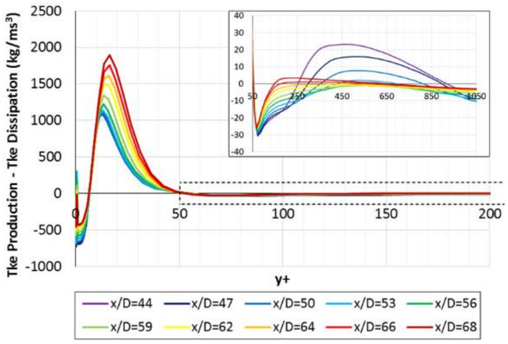

(f1) Tke net production (onset)

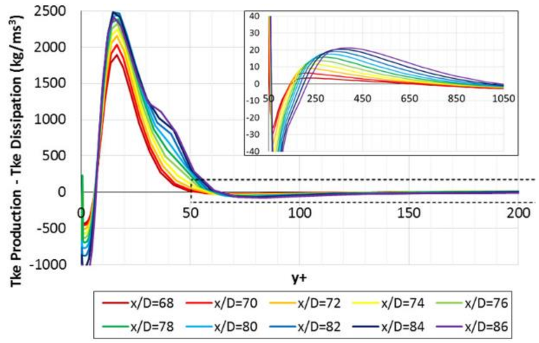

(f2) Tke net production (recover)

Figure 55 Radial distribution of turbulence and shear stress by RST – 2nd peak

As the flow moves downstream, the fluid is further heated. Since the turbulent diffusivity is high, the heat can be effectively used to raise the enthalpy of the fluid in core region. The density of the core fluid decreases further (Figure *55* b1) which increases the velocity in the core, meanwhile, the buoyancy force becomes even weaker. All these factors make the velocity profile shift away from the M-profile (Figure *55* b1), leading to the decrease in the shear stress (dV/dy) in the core region (Figure *55* c1).

As discussed earlier, turbulence production is directly related to the shear stress. The decrease in the velocity gradient in the core materially reduces the Reynolds shear stress and turbulence production in that region (Figure *55* d1, f1). The net production of Tke in the core drops to a negative value, which means turbulent dissipation is again dominant. Indeed the turbulent kinetic energy decreases significantly in the core region, see Figure *55* e1. It is also notable that the turbulent kinetic energy in the near-wall region y+<50 does not change appreciably, although there is an increase in the local turbulence production (Figure *55* f1). Thus, the reduction in the Tke in the core region is responsible for the onset of this second temperature peak. This is actually consistent with the conclusion of first peak, i.e. while normally production in the buffer layer is most important, it is the change of turbulence (Tke) outside the buffer region which gives rise to the unique behaviour of buoyancy driven HTD.

The reduction in turbulence in the core region impairs the heat transfer effectiveness allowing the low-density layer near the wall to grow again (Figure *55* a2). The density difference becomes greater, resulting in the greater buoyancy force, which further accelerates the near-wall layer leading to restoration of the M-shape velocity profile, see Figure *55* b2. Therefore, the shear stress (dV/dy) becomes greater in both 0<y+<80 and y+>250. As a result, the Reynolds shear stress and the turbulence production (net) increase appreciably in those two regions, see Figure *55* d2, f2. Accordingly, the turbulence kinetic energy rises in both near-wall region 10<y+<80 and core region y+>200, which leads to the recovery of wall temperature from the second deterioration.

5.3.2 Entrance Effect in No-gravity Flow

The discussion above suggests that the entrance effect is playing a crucial role in triggering the HTD under some flow conditions. To observe the effect of buoyancy a comparison is made by carrying out a similar study in a no-gravity flow with identical boundary conditions, i.e. P=8.5MPa, q=100kW/m^2, G=505kg/m^{2}s, T_{in}=12^{o}C. The wall temperature distribution of no-gravity flow is shown in Figure *56* along with the temperature predictions of downward flow.

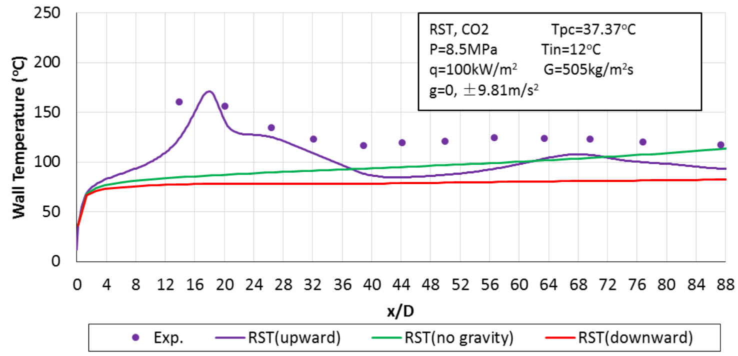

Figure 56 Axial wall temperature distributions with three options of gravity

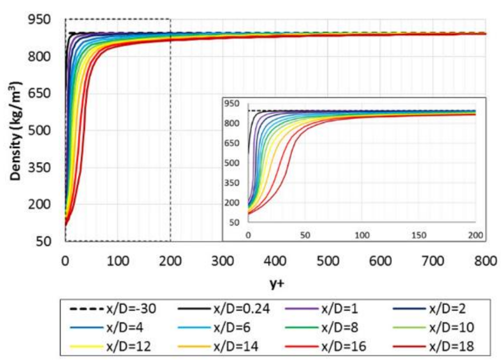

(a) Density (upward, onset of HTD)

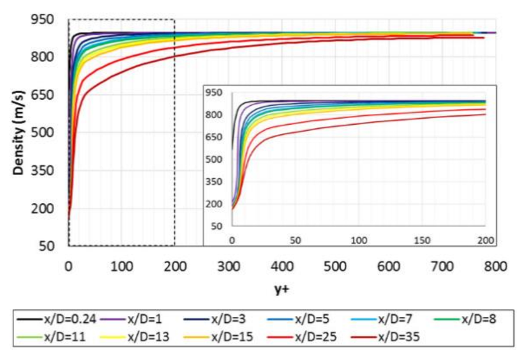

(b) Density (no gravity)

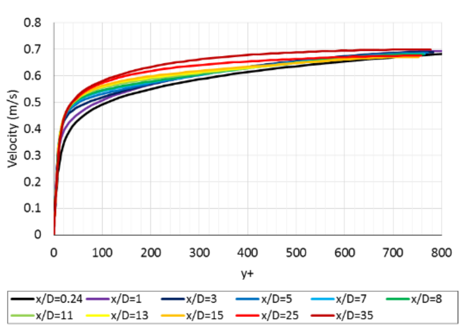

(c) Velocity

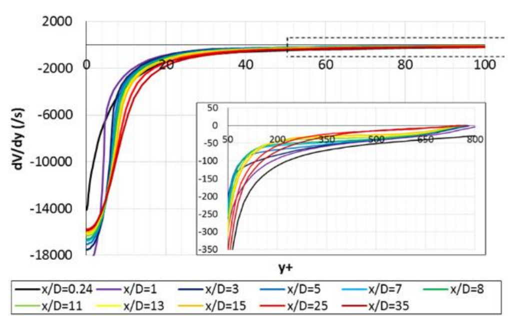

(d) Velocity gradient

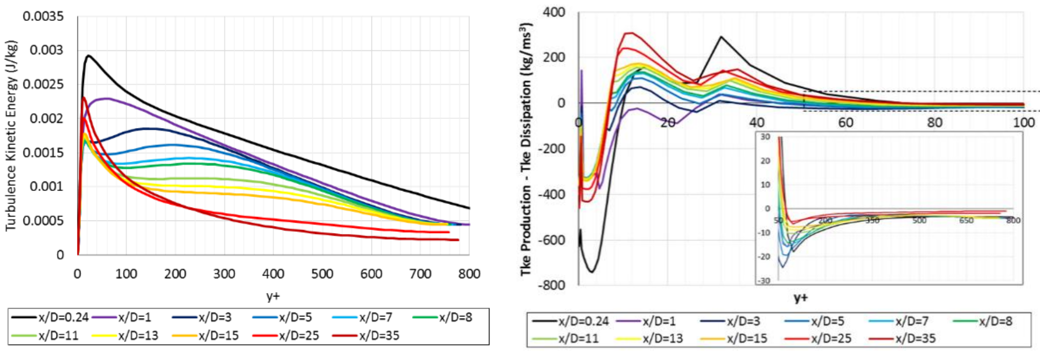

(e) Turbulence kinetic energy (f) Net production of k

Figure 57 Radial distribution of fluid properties by RST in no-gravity flow

Figure *57* shows the variation of fluid properties in the entrance region (The density distribution in the upward flow case is also put here for comparison, see Figure *57* a). It was clear that similar entrance effect as discussed for upwards flow also exists here. After the flow enters the heated region, a similar thin low-density layer is formed against the wall within a very short distance (x/D=1). The fluid in the thin layer is immediately accelerated (Figure *57* c and d). As a result, the shear stress (which is proportional to dV/dy) within y+<6 increases, and that in y+>6 decreases. Since most of the turbulence is generated within 10<y+<80, the reduced shear stress leads to the impairment in turbulence production, see Figure *57* f, which is just like what is observed in the upward flow case. Apparently, this modification of shear stress we refer to as the “entrance effect” is not caused by buoyancy. It is suspected that the thermal expansion in the thin low-density layer when it is formed is playing a more important role here.

As the flow proceeds downstream, the density of fluid near the wall decreases further. However, because there is no buoyancy force, the near-wall fluid will not be accelerated as much as in the upward flow case (it will still accelerate due to density expansion). Therefore, the velocity profile away from the wall is not flattened, and it is only slightly modified (Figure *57* c). The shear stress in y+<50 is increased while that in the y+>50 remains largely unaffected (Figure *57* d), which leads to the regeneration of turbulence within 10<y+<60 (Figure *57* f) in the region 3<x/D<35. The difference between upward flow and no-gravity flow is that the turbulence is able to regenerate within 30<y+<60 in the no-gravity case but not in the upward flow case. The reason is that in upward flow the velocity profile in the core region is made extremely flat due to the extra buoyancy force close to the wall which limits the turbulence production in y+>30 (Figure 54 c1 and d1) preventing the turbulence (Tke) from recovering for upward flows.

The Tke level in the zero-gravity case does not go into the dissipation dominated regime, and hence turbulence recovers such that no deterioration is possible (Figure *57* e). It is also notable that the low-density layer in the zero-gravity case does not grow and is always limited to the viscous sublayer (Figure *57* b), which is attributed to higher turbulence level in the near-wall region. It allows better removal of heat from the wall-layer to the core fluid, and in turn the resulted ultra-thin low-density layer will leads to a higher heat transfer effectiveness.

5.3.3 SST and SLR in Upward Flow

The discussions on the HTD mechanism in the last two sections are based on the RST model which presents the best performance in this study. Nevertheless, it is still worthwhile to compare other two-equation turbulence models which showed reasonable agreement with the experimental results.

SST model (First Peak)

SST model predicts a very similar wall temperature trend as RST model, except for the over-estimation of maximum temperatures, see Figure *40*. The predicted two temperature peaks are plotted against axial locations on Figure *58*. It should be noted that the location of the first peak is shifted upstream compared to RST while the second peak is further downstream. Only the first peak will be studied here. Again, about twenty axial locations within the range of first peak are picked, ten on each side.

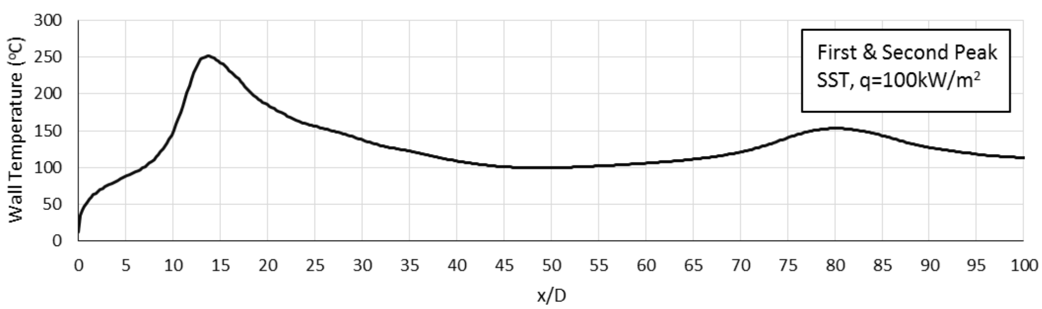

Figure 58 Wall temperature distribution predicted by SST

The distributions of fluid properties at these locations can be found in Figure *59*. The curves of various fluid properties are noticeably distorted around y+=35, which is not observed in RST study. Since the y+ value here are calculated with local fluid properties using the following equation:

$$y^+ = \frac{\rho u_t y}{\mu} = \frac{\rho y\sqrt{\tau_w/\rho}}{\mu}$$

The distortion is attributed to the very strong variation of properties where the local fluid temperature at that y+ value exceeds the T_{pc}. In other words, when the density and viscosity are decreasing so quickly with increasing distance (y), the calculated y+ may decrease even though y is increasing. The reason why RST avoids this issue may be that the variation of fluid properties between two adjacent cells predicted by RST is slower.

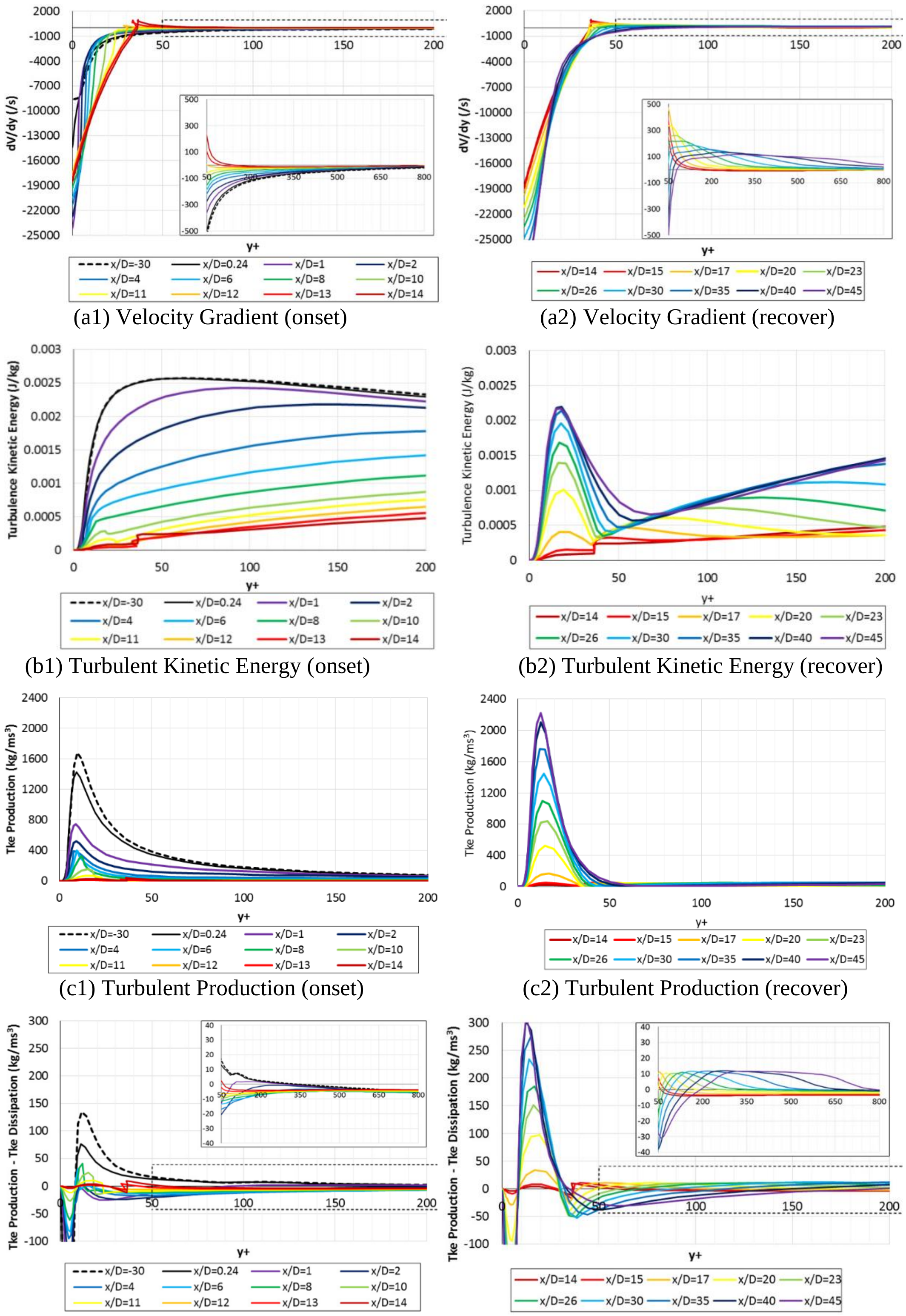

(a1) Velocity Gradient (onset)

(a2) Velocity Gradient (recover)

(b1) Turbulent Kinetic Energy (onset)

(b2) Turbulent Kinetic Energy (recover)

(c1) Turbulent Production (onset)

(c2) Turbulent Production (recover)

(d1) Net Production of Tke (onset)

(d2) Net Production of Tke (recover)

Figure 59 Radial distribution of fluid properties by SST model – 1st peak

The profiles of velocity (therefore shear stress) predicted by SST model (Figure *59* a1, a2) are very similar to that by RST model (Figure *53* d1, d2). Hence, it is not surprising that SST model predicts a very similar temperature trend in this case. It can also be seen from Figure *59* c1, the turbulence production drops rapidly after the flow enters the inlet, followed by the immediate reduction in turbulence kinetic energy, which leads to the onset of HTD. However, there exists a significant difference between SST and RST, i.e. the production of Tke in the near-wall region during the onset of HTD continuously decreases in the SST without showing a regeneration within $10<y+<30$ (SST: Figure *59* c1, RST: Figure 54 c1). Consequently, no peak of Tke within $10<y+<50$ is observed, as can be seen in Figure *59* b1. In other words, the turbulence level during the onset of HTD predicted by SST is lower than that by RST model, especially within $10<y+<35$. This under prediction of the restoration of turbulence explains why SST overestimates the peak temperature.

It is surprising that the greater velocity gradient in $y+<35$ (Figure *59* a1) was unable to regenerate the turbulence production in that region. This is in fact quite misleading, as the monotonous decrease in Tke and production of Tke may lead to an understanding that the low-density layer needs to grow sufficiently thick to have a significant impact on the turbulence production and then heat transfer, which apparently is not true. The net production of Tke (Figure *59* d1) predicted by both SST and RST has already reached a very low level (negative) in a very short distance from the inlet (x/D=1).

It can be seen from Figure *59* b2, c2, d2 that, the near-wall turbulence production predicted by SST model is able to recover downstream after the change of sign in shear stress (or velocity gradient). The turbulence production rate and turbulence kinetic energy after recovery has reached a level close to that predicted by RST model in both near-wall region and the core region. This makes SST model predict a wall temperature distribution that is similar to RST model.

SLR model

SLR model as a typical low-Reynolds k-ε model, significantly over-predicted the wall temperature, and the wall temperature did not truly recover until the bulk temperature is raised up close to T_{pc}. The wall temperature predicted by SLR model are plotted against axial location in Figure *60*.

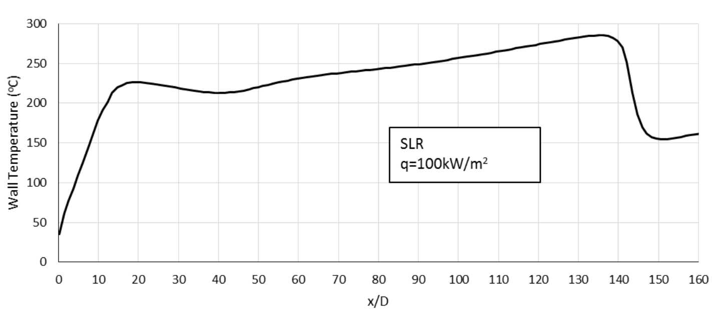

Figure 60 Wall temperature distribution predicted by SLR model

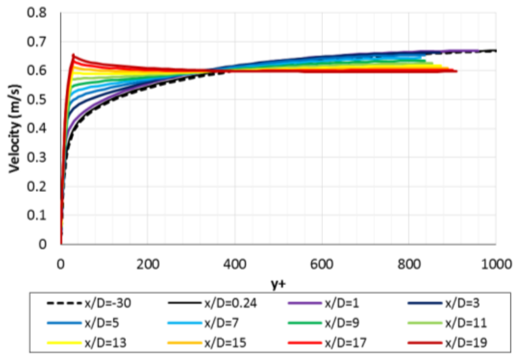

(a1) Velocity (onset)

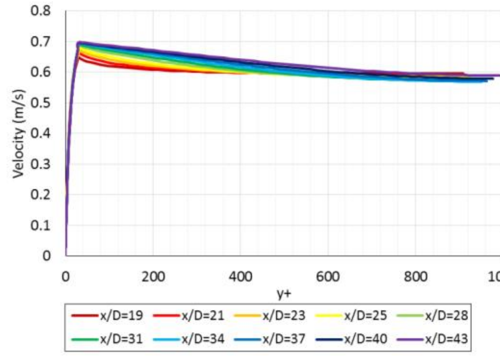

(a2) Velocity (fake recover)

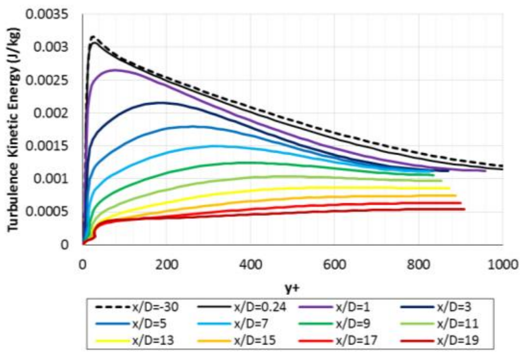

(b1) Turbulence Kinetic Energy (onset)

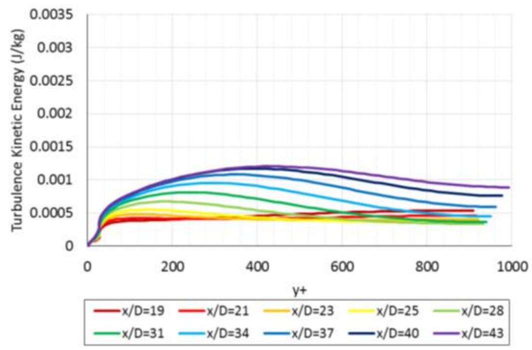

(b2) Turbulence Kinetic Energy (fake recover)

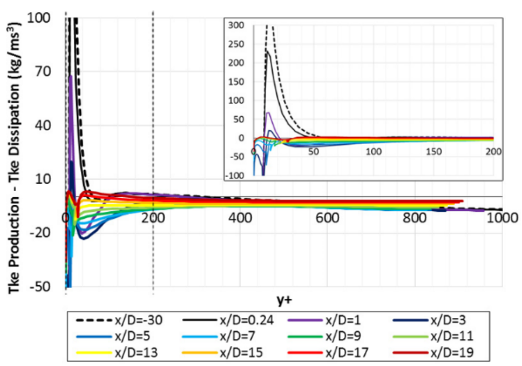

(c1) Net Production of Tke (onset)

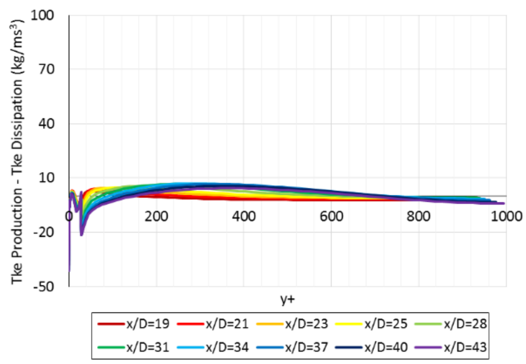

(c2) Net Production of Tke (fake recover)

Figure 61 Radial distribution of fluid properties by SLR model

The variations of fluid properties from inlet to x/D=43 are shown in Figure *61*, while that from x/D=45 to x/D=155 are shown in Figure *62*. Similar to SST model, the curves are distorted where the fluid properties undergo strong variations. The turbulence production is also impaired in a short distance from the inlet (Figure *61* c1). The net production of Tke in the near-wall region (10<y+<30) is not regenerated during the onset of HTD similar to SST. As a result, the turbulence kinetic energy decreases monotonously (Figure *61* b1). It is clear that the onset of HTD predicted by SLR is very similar to that predicted by SST.

After the onset of HTD, SLR model still fails to restore the turbulence in the near-wall region (Figure *61* b2) as turbulence production is not regenerated. However, there exists a mild recovery of turbulence in the core region (Figure *61* b2), which is attributed to the increase in shear stress when the velocity profile starts to take up the M-shape. The increase in turbulence in the core region helps recover the wall temperature by a small amount after the onset of HTD, but it is too weak to be considered as a full recovery. Apparently, the flow is still at the laminarization stage, and the low turbulence level near the wall is responsible for this behavior.

As the flow proceeds downstream, the velocity increases due to the decrease in bulk density, but the velocity profiles remain flattened, see Figure *62* a. As expected, the shear stress and therefore turbulence production will not change notably. The turbulence kinetic energy stays at a relatively low level until comes the recovery at x/D=140 (Figure *62* b). The recovery does not occur until the temperature of bulk fluid is close to T_{pc} (Figure *62* d), which implies that SLR model relies on reduction in density difference when the temperature of fluid next to the low-density layer exceeds T_{pc}, to redistribute the shear stress and regenerate the turbulence. It can be seen that the variation in the vicinity of maximum on the velocity profile becomes more gradual when the recovery comes (Figure *62* a). The increase in shear stress in the near-wall region helps restore the turbulence quickly, which leads to the rapid recovery of wall temperature. In He's study [44], the AKN (low-Re) model presents a similar behavior. Compared to that predicted by RST and SST models (they rely on the change of sign of the shear stress in the core region to restore turbulence), it is clear that SLR model fails to reproduce the observed recovery of HTD.

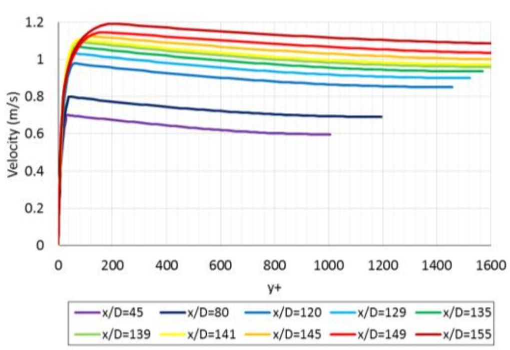

(a) Velocity

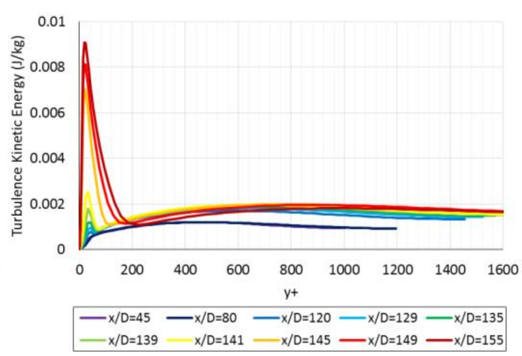

(b) Turbulence Kinetic Energy

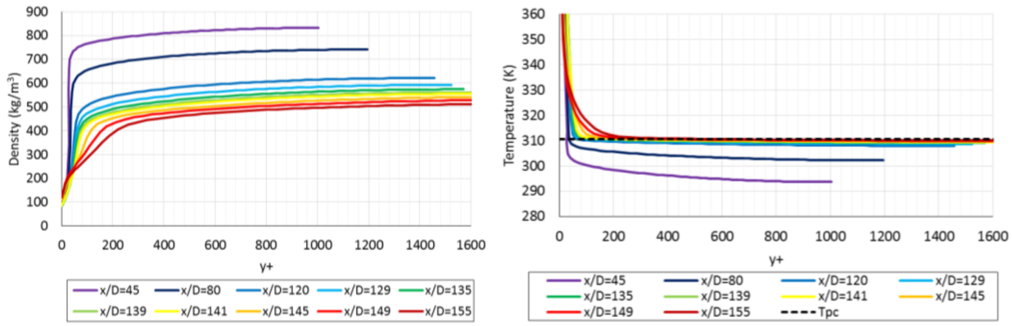

(c) Density (d) Temperature

Figure 62 Regeneration of turbulence – SLR

By far, we can safely come to the conclusion that RST models is both qualitatively and quantitatively better than the two low-Reynolds models (SLR and AKN) in predicting the HTD and its subsequent recovery. Figure *63* to Figure *65* show the surface plot of turbulent kinetic energy (Tke) predicted by RST, SST and SLR models respectively. Tke in the core region predicted by RST reaches a very low level at two different locations corresponding to two wall temperature peaks (Figure *63*). SST model fails to partly regenerate the turbulence in the buffer layer during the onset of the first HTD, which makes it overestimate the peak temperature, but it is able to restore the turbulence as well as RST model during the recovery (Figure *64*). Nevertheless, because RST and k-ω models (SST and WI) predict the HTD at higher heat fluxes compared to experiments, often in literature they are overlooked. Rather CFD users should conduct sensitivity analyses on heat flux, and quite often as a result qualitatively excellent agreement can be observed in some of these models.

Besides, the abnormally small recovery after the onset of HTD predicted by the low-Reynolds k-ε models is often mistaken for the real recovery which in fact comes much further downstream when the bulk temperature is close to T_{pc}. This is confirmed after re-simulating one of the cases in Sharabi's paper [45]. The results are presented and discussed in the Appendix 1. In that original paper the length simulated was not sufficient to observe the significant recovery which only occurs as the bulk fluid approaches the pseudo-critical temperature. The low-Reynolds k-ε models tend to over-predict the downstream wall temperatures after the onset of HTD, because the turbulence production is not regenerated within the correct region, see Figure *65*.

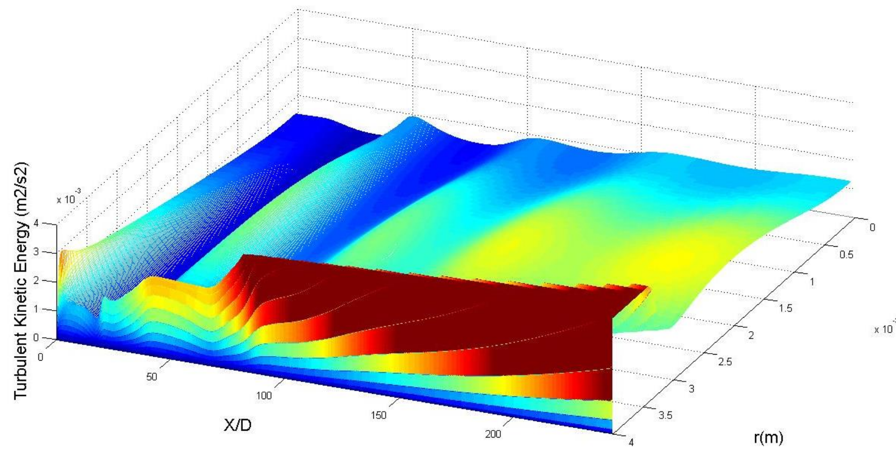

Figure 63 Surface plot of Turbulence Kinetic Energy by RST model, T_{in}=12°C, G=505kg/m^2-s, q=100kW/m^2 – (Maximum Tke= 0.0352m^2/s^2)

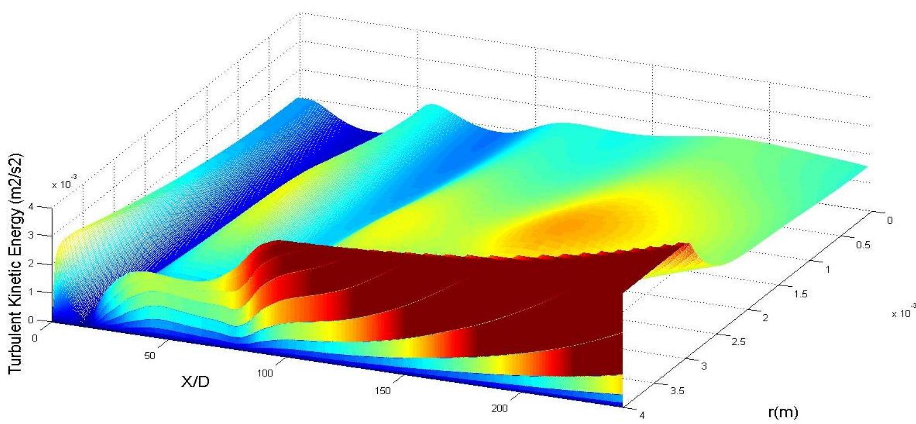

Figure 64 Surface plot of Turbulence Kinetic Energy by SST model, T_{in}=12°C, G=505kg/m^2-s, q=100kW/m^2 – (Maximum Tke= 0.0222m^2/s^2)

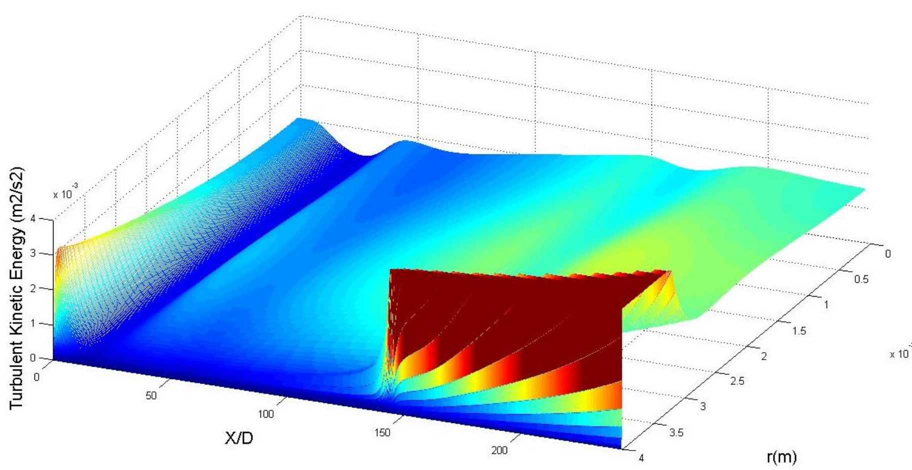

Figure 65 Surface plot of Turbulence Kinetic Energy by SLR model, T_{in}=12°C, G=505kg/m^2-s, q=100kW/m^2 – (Maximum Tke= 0.0292m^2/s^2)

5.4 Supercritical Water Flow

The experimental data on supercritical water by Watts [33] covered a wide range of flow conditions, those used in this study are summarized in the Table *7*. Since one of the main interests of this study is to assess the performance of different turbulence model in predicting the HTD, most of the simulated cases are those where HTD was observed experimentally. The majority of them have wall temperature below pseudo-critical temperature, i.e. $T_b<T_w<T_{pc}$, which is different from previous CO_2 study where all the simulated cases have wall temperature above T_{pc}. However, there are still few cases in which the axial wall temperature curve crosses T_{pc}, or are above T_{pc}. Hence, all the simulated flow conditions are roughly categorized into three types, i.e. a) $T_b<T_{pc}<T_w$, b) $T_b<T_w<T_{pc}$, and c) T_w crosses T_{pc}. Of course, this categorization is not for the identification of different types of HTD, as all three types are caused by buoyancy. Nevertheless, it is found that the performance of turbulence models is largely dependent on the type of flow conditions characterized by the relation between T_b, T_w and T_{pc}.

5.4.1 Performance of Various Turbulence Models

Since it is time consuming to simulate all the cases using all turbulence models, the first step is to pick three typical experiments that fall into the three types of flow conditions, and run them with different turbulence models to get a preliminary idea on the performance of those turbulence models. Based on the results from previous CO_2 study, only the four most representative turbulence models are chosen for comparison, i.e. SLR, AKN, SST, and RST, as listed in Table *5*.

1. $T_b<T_{pc}<T_w$

There is one set of the experimental data that has wall temperatures above the T_{pc}, i.e. $T_b<T_{pc}<T_w$. In these cases, T_w exceeds T_{pc} at a location very close to the inlet of heated section, which is same as the CO_2 experiments we discussed earlier. Figure *66* shows the wall temperature distributions predicted by different turbulence models in one of these cases.

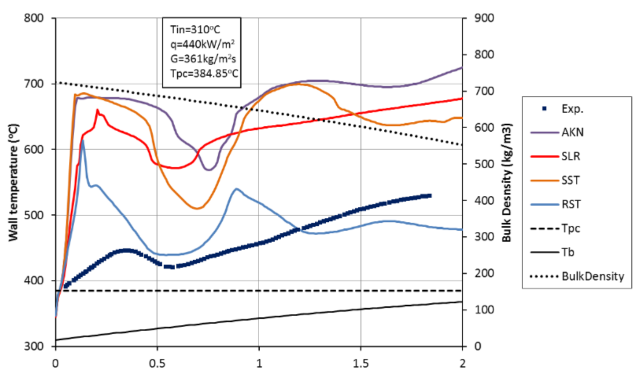

Figure 66 Wall temperatures predicted by different turbulence models - $T_b<T_{pc}<T_w$

It can be seen from Figure *66*, all the turbulence model are able to predict the HTD, however, with significant overestimation of the peak wall temperatures. RST model performs the best among them, mainly because it is able to recover the wall temperature after the onset of HTD better than other turbulence models. It is notable that RST predicts a very similar temperature trend to its prediction in the CO_2 study, i.e. in both cases RST predicts two sharp temperature peaks. However, the measured wall temperatures in the water experiments when $T_b<T_{pc}<T_w$ are very different from those in the CO_2 experiments. The temperature peak from the water experiments as seen in Figure *66* is much milder and more flattened than that in the CO_2 experiments. It seems RST model was not able to capture the difference between two experiments, even though it is quantitatively better than other models.

2. $T_b<T_w<T_{pc}$

The majority of the water data from Watts's experiments have wall temperatures below the pseudo-critical temperature, i.e. $T_b<T_w<T_{pc}$. These cases which are different from the previous CO_2 cases are the main interest of the H_2O study in this chapter. The fluid temperature never exceeds T_{pc}, hence the density difference between the wall layer and the core fluid is much milder. For this type of flow, the simulated flow condition is: T_{in}=150ºC, q=175kW/m^2, G=278kg/m^{2}s. The results are shown in Figure *67*. It is clear that SST and RST predict no HTD in this case, whereas the two low-Re k-ε models, i.e. AKN and SLR, were able to qualitatively predict the wall temperature peak resulting from the HTD.

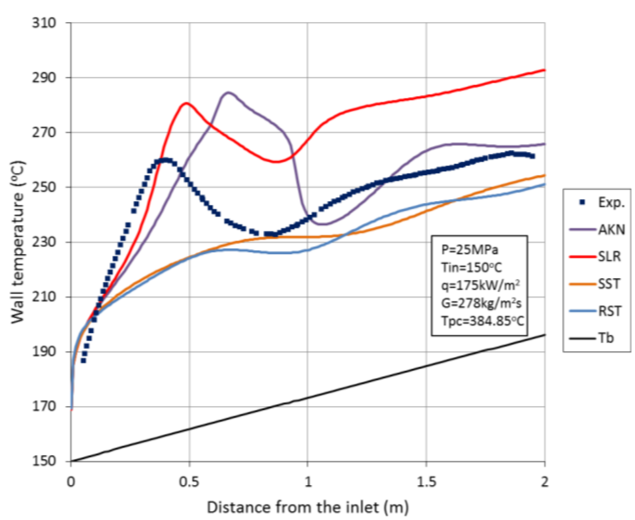

Figure 67 Wall temperatures predicted by different turbulence models - $T_b<T_w<T_{pc}$

Figure 68 summarized the wall temperatures predicted by RST model at the lowest mass fluxes in different sets of experimental conditions. From Figure *68*, it can be seen that RST model failed to predict the HTD in all the low-mass-flux cases where $T_b<T_w<T_{pc}$, and the downstream wall

temperature is significantly underestimated. In some cases, the RST predicted a mild temperature peak, however, much lower than that observed experimentally. SST showed similar behaviours in these cases. Therefore, it can be concluded that both RST and SST under-predict the buoyancy effects when the T_w is below T_{pc}. In other words, the transport of heat from the near-wall region to the core is overestimated. The author also attempted to increase the heat flux as in the previous CO_2 study, to see whether RST and SST would predict a stronger HTD at slightly higher heat flux. The results are shown later in section 5.4.3 when studying the sensitivity of heat flux.

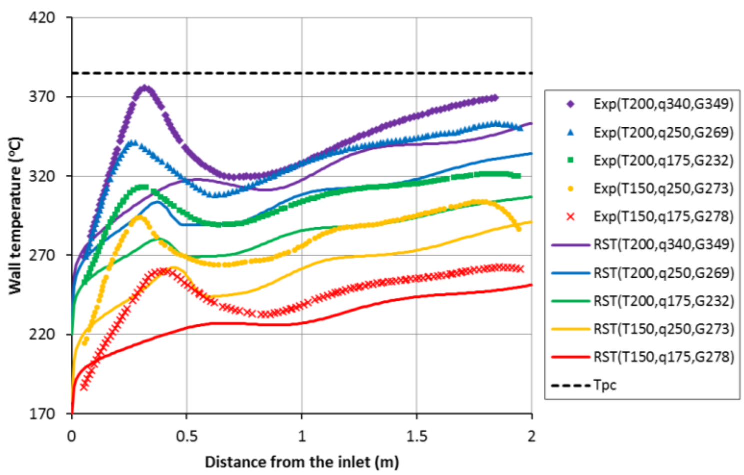

Figure 68 RST model at relatively low mass fluxes

3. T_w crosses T_{pc}

In this type of flow, the wall temperatures exceed T_{pc} at locations between the inlet and outlet, i.e. part of the wall temperatures are above the T_{pc} while part of them are below T_{pc}. This is the transition from the first type to the second type. The simulated experiment and the wall temperature distributions predicted by the four turbulence models are shown in the Figure *69*.

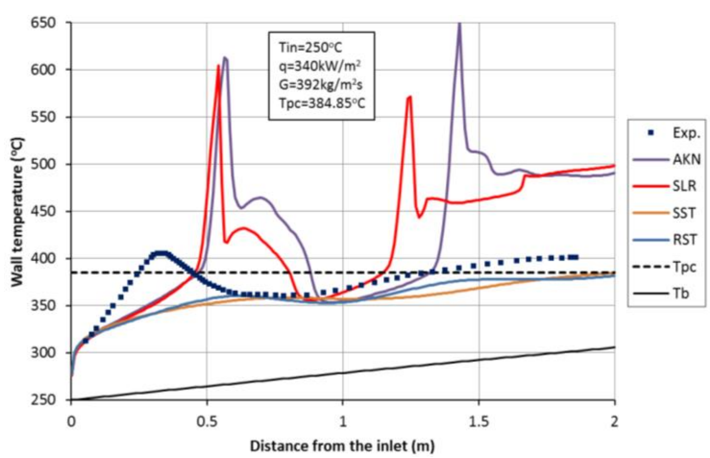

Figure 69 Wall temperatures predicted by different turbulence models – T_w crosses T_{pc}

It can be seen that the two low-Re models (AKN and SLR) predict two sharp temperature peaks at locations where T_w exceeds the T_{pc} which is different from that observed in experiments. The HTD in experiments is mild and occurs near the inlet (well before T_w approaches T_{pc}), while the HTD predicted by AKN and SLR is sharp and occurs at axial locations where T_w exceeds the T_{pc}. This phenomenon is attributed to the strong variation of fluid properties near the wall with temperatures approaching T_{pc}, especially the drastic decrease in density and viscosity. When the temperatures of the wall and near-wall fluid exceeds T_{pc}, the fluid properties will change dramatically. It seems that both AKN and SLR overestimate the impact of this strong variation in fluid properties on HTD. SST and RST still fail to predict HTD in this case, and the wall temperature profiles remain below T_{pc}.

After the above discussion, it is concluded that when $T_b<T_w<T_{pc}$, AKN and SLR models are better than SST and RST models in predicting the HTD; however, in cases where $T_b<T_{pc}<T_w$, RST performs the best among these turbulence models.

5.4.2 Effect of Mass Flux

As mentioned earlier, in Watts's experiments one set of observations was taken with the same inlet temperature and heat flux, but over a range of mass flux. Hence, those experimental data can be used to study the effect of mass flux on the predicted HTD.

- **$T_b<T_w<T_{pc}$**

The mass flux effect when $T_b<T_w<T_{pc}$ is studied using AKN, SLR and RST models. The results are shown in the following figures (AKN: Figure *70*; SLR: Figure *71* to Figure *73*; RST: Figure *74*).

In experiments, the HTD occurs at relatively low mass flux, and the decrease in mass flux acts to move the temperature peak upstream. It is notable that there exists a maximum peak temperature when the mass flux is decreasing, i.e. after reaching a certain mass flux the decrease in mass flux does not increase the peak temperature further (Figure *71* to Figure *72*).

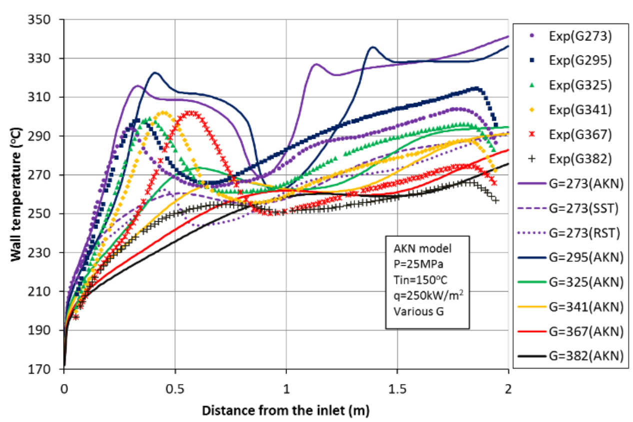

Figure 70 AKN model at different mass fluxes – T_{in}=150ºC, q=250kW/m^2

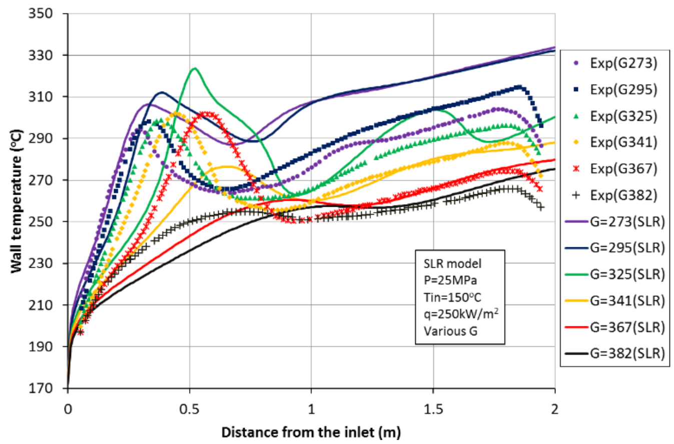

Figure 71 SLR model at different mass fluxes – T_{in}=150ºC, q=250kW/m^2

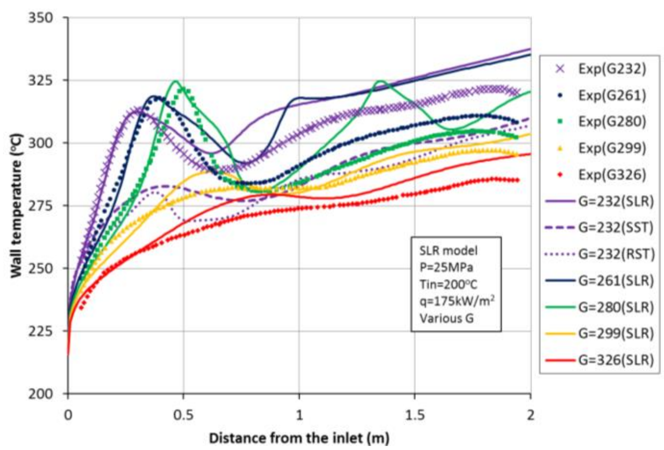

Figure 72 SLR model at different mass fluxes – T_{in}=200ºC, q=175kW/m^2

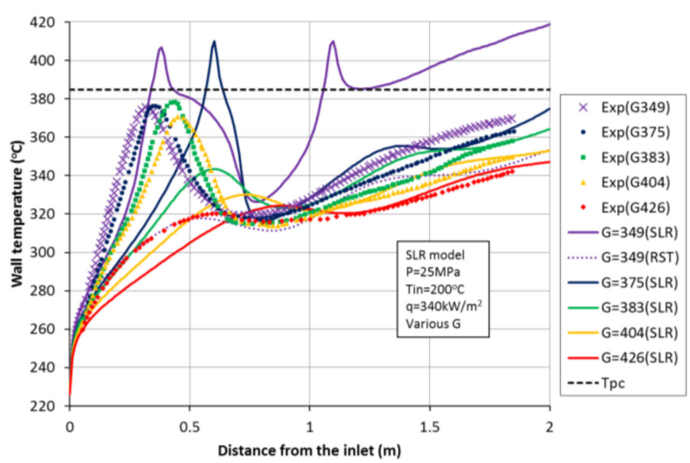

Figure 73 SLR model at different mass fluxes – T_{in}=200ºC, q=340kW/m^2

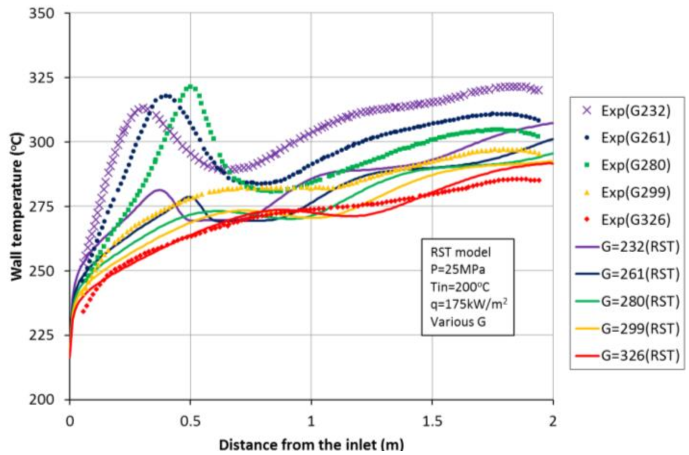

Figure 74 RST model at different mass fluxes – T_{in}=200^{o}C, q=175kW/m^2

Figure *70* and Figure *71* show the mass flux effect at T_{in}=150^{o}C, q=250kW/m^2 predicted by AKN and SLR models respectively. It can be seen that both AKN and SLR models are able to qualitatively predict the first temperature peak at relatively low mass fluxes. However, with increasing mass flux, the discrepancies increase, as AKN and SLR models predict the HTD at lower mass flux than the experiments. Comparing AKN and SLR models, it is clear that SLR model is quantitatively better than AKN model in most of the cases. Hence, for other flow conditions, only the results by SLR model are presented here, while that by AKN model are attached in Appendix 3.

After careful observation on Figure *71* to Figure *73*, it can be seen that SLR model is able to reproduce the first temperature peak very well, especially at low heat fluxes. In Figure *72*, SLR predicts the wall temperatures both qualitatively and quantitatively, except for the over-estimation of the downstream temperature. In some cases, e.g. G=325kg/m^{2}s in Figure *71*, and G=280kg/m^{2}s in Figure *72*, the SLR model predicts a second temperature peak which is not observed in experiments. This second peak is very sensitive to heat flux and seems the prelude to the over-estimation of the downstream wall temperature (discussed later in the sensitivity study). It seems that at high heat-flux-to-mass-flux ratio, the low-Reynolds models (AKN and SLR) tend to over-predict the wall temperature after the onset of HTD, which is consistent with what is found in the previous CO_2 study. It is also notable that the overpredicted downstream wall temperatures in Figure *71* are almost identical, even though the mass fluxes are different (similar behavior is also observed in Figure *70* and Figure *72*).

Figure *74* shows the wall temperatures distributions predicted by RST model at various mass fluxes. It can be seen that RST predicts the wall temperature very well at high mass flux where no HTD is observed experimentally. However, with decreasing mass flux, discrepancy increases prior to the onset of HTD. RST model significantly underestimates both the peak temperature and the downstream wall temperatures at lower mass fluxes.

- **T_b <T_{pc}<T_w**

The mass flux effect when T_b<T_{pc}<T_w is studied using RST model only, the results of which are shown in Figure *75*.

Although RST seems better than other turbulence models in predicting the HTD when T_w is above T_{pc}, the wall temperatures at various mass fluxes predicted by RST model in Figure *75* are still significantly overestimated. As discussed above, the predicted temperature peaks are more peaked than observed experimentally. In experiments, the measured temperature peak is mild, and with increasing mass flux, the peak moves downstream and becomes even more flattened. Although, the predicted peak also moves downstream and becomes lower as the mass flux increases, it is still nothing like those measured in experiments.

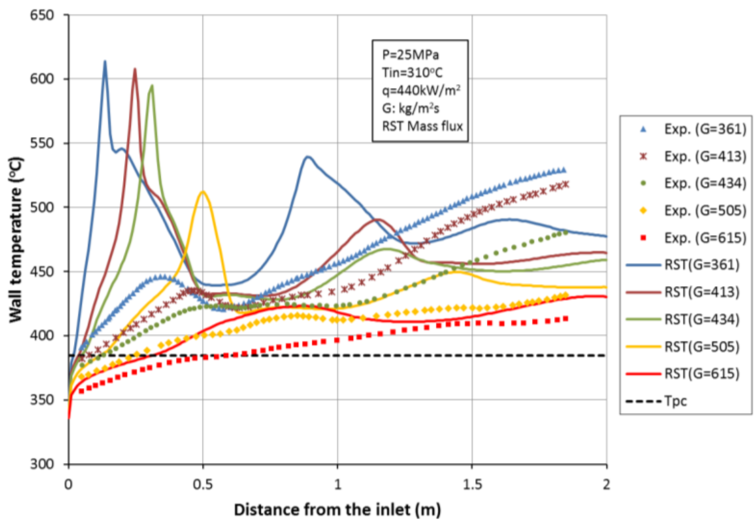

Figure 75 RST model at different mass fluxes – T_{in}=310°C, q=440kW/m^2

5.4.3 Sensitivity Study of Heat Flux

As mentioned earlier in experimental investigation, the thicker side of pipe has a slightly higher heat flux than the thinner side. But the pipe is treated as uniformly heated in this study by using the average heat flux. Hence, it is necessary to study the sensitivity of turbulence models to heat flux. On the other hand, the heat flux effect on HTD may help gain a deeper insight into the heat transfer behaviour predicted by those turbulence models.

SLR model

The results of heat flux sensitivity study of SLR model are shown in Figure *76*, Figure *77* and Figure *78*. Those less important ones in other flow conditions are also attached in Appendix 4.

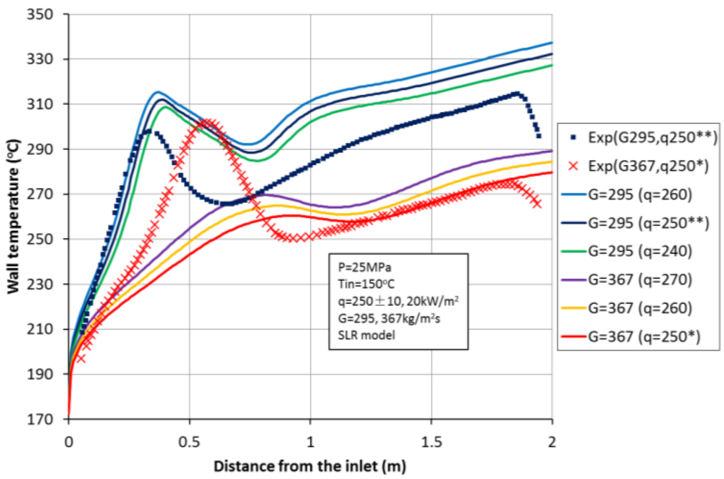

Figure 76 Sensitivity of heat flux outside the vicinity of HTD threshold

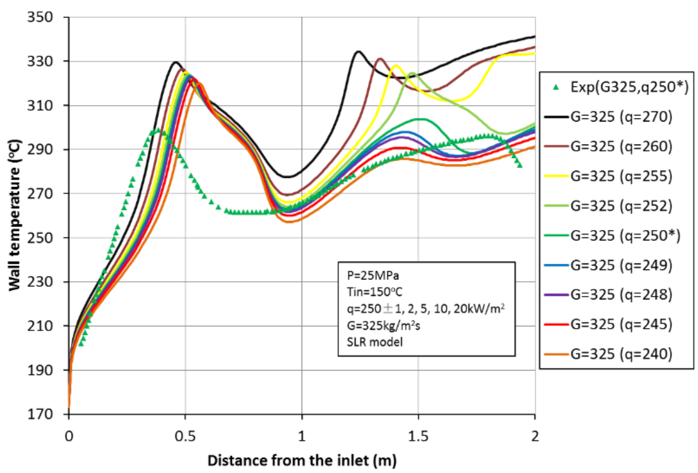

Figure 77 Sensitivity of heat flux in the vicinity of HTD threshold (second peak)

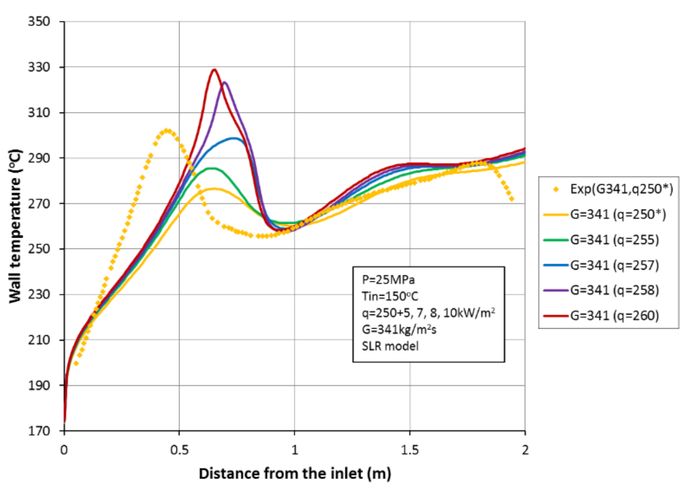

Figure 78 Sensitivity of heat flux in the vicinity of HTD threshold (first peak)

It can be seen that only in the vicinity of HTD threshold the wall temperatures are sensitive to the change of heat flux, see Figure *77* and Figure *78*. Beyond the vicinity of HTD threshold, the results are far less sensitive (Figure *76*). It is consistent with what is found in the sensitivity study of mesh and turbulent Prandtl number in section 5.1. This behaviour is also observed in the CO_2 study as discussed earlier.

The predicted second temperature peak eventually evolves into the overestimation of the entire downstream wall temperature with a small increase in the heat flux (Figure *77*). Hence, the second peak is very sensitive to heat flux and may be the prelude to the overestimation of the downstream temperatures. It is clear that the SLR model as a typical k-ε low-Reynolds model tends to over-predict the downstream wall temperature. This is attributed to the failure in regenerating the turbulence after the onset of HTD (discussed in section 5.5.1).

<u>RST & SST model</u>

In the CO_2 study, both RST and SST predict HTD at higher heat fluxes than observed in experiments, and they were qualitatively better than other turbulence models in predicting the observed two temperature peaks. In these H_2O cases where $T_b<T_w<T_{pc}$ they both underestimate the HTD and the downstream wall temperatures even at the lowest mass fluxes, hence we also examine the effect of heat flux on the predictions. The results are shown in the following figures.

It can be seen from Figure *79* and Figure *80* that the response of RST and SST models to the increase in heat flux is very different from that observed in the CO_2 study. The increase in heat flux only acts to raise the wall temperature profiles without affecting too much its shape, i.e. the relative magnitude of the temperature peak is not affected.

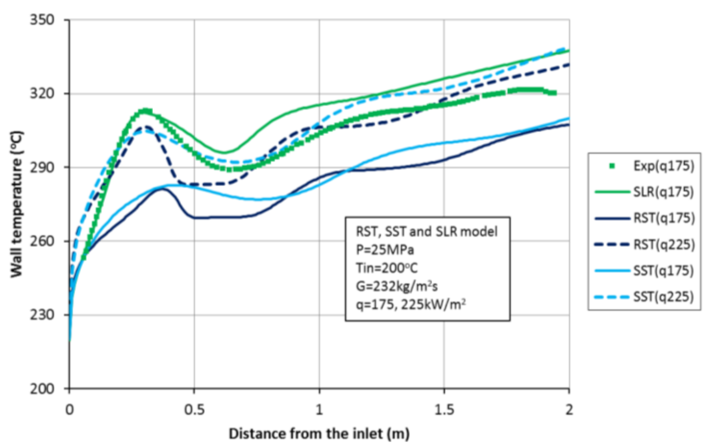

Figure 79 Heat flux effect by RST and SST ($T_b<T_w<T_{pc}$, T_{in}=200°C, q=175kW/m^2, G=232kg/m^{2}s)

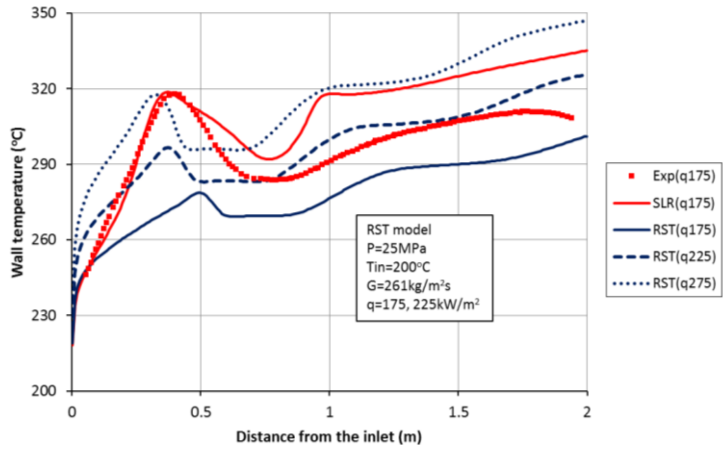

Figure 80 Heat flux Effect by RST (T_b<T_w<T_{pc}, T_{in}=200ºC, q=175kW/m^2, G=261kg/m^{2}s)

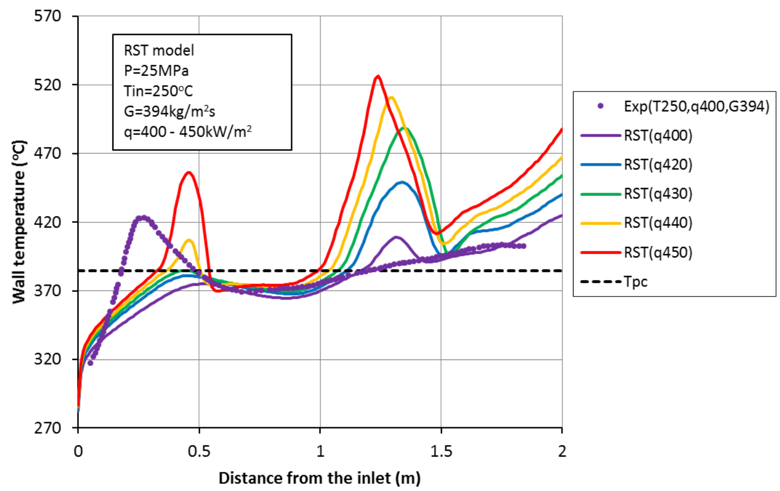

Figure 81 Heat flux effect by RST (T_w crosses T_{pc}, T_{in}=250ºC, q=400kW/m^2, G=394kg/m^{2}s)

Although, the wall temperature predicted by these two models become closer to the experimental data when the heat flux is increased by an amount of 50kW/m^2 (Figure *79*), this is attributed to the increase in bulk temperature rather than the increase in buoyancy effect. Hence, it is confirmed that RST and SST both under-predict the buoyancy effect when T_w<T_{pc}.

Figure *81* shows the heat flux effect predicted by RST model at much higher heat flux. In this case, T_w is very close the T_{pc}, and the increase in heat flux raises the wall temperature profile and makes it cross T_{pc}. RST model predicts two temperature peaks where T_w exceeds T_{pc}. This behavior is very similar to that predicted by SLR and AKN models in another case as seen in Figure *69* of section 5.4.1. The predicted temperature peak apparently is different from the one observed in experiments which is mild and occurs near the inlet.

RST and SST models show such a poor performance in predicting the HTD in cases with $T_w<T_{pc}$. In order to be assured that it is not just for flow conditions in Watts's experiments, the author re-simulated several cases with $T_w<T_{pc}$ from He's study [42] using RST, SST, and SLR models. The results show consistent response to that discussed above (see Appendix 2).

5.4.4 Effect of Inlet Temperature

Since RST model behaves so differently in predicting the HTD in two different types of flows ($T_b<T_{pc}<T_w$ and $T_b<T_w<T_{pc}$), we investigate how RST model would predict the transition from one type of flow to another. Two typical cases from experiments are selected, one with $T_b<T_{pc}<T_w$ in which RST predicts two sharp temperature peaks, another with T_w crosses T_{pc} in which RST predicts no HTD near the inlet. Since the two selected cases have almost the same heat flux and mass flux and the only significant difference is the inlet temperature, this transition study is done by gradually increasing the inlet temperature in the code. The results are shown in Figure *82*.

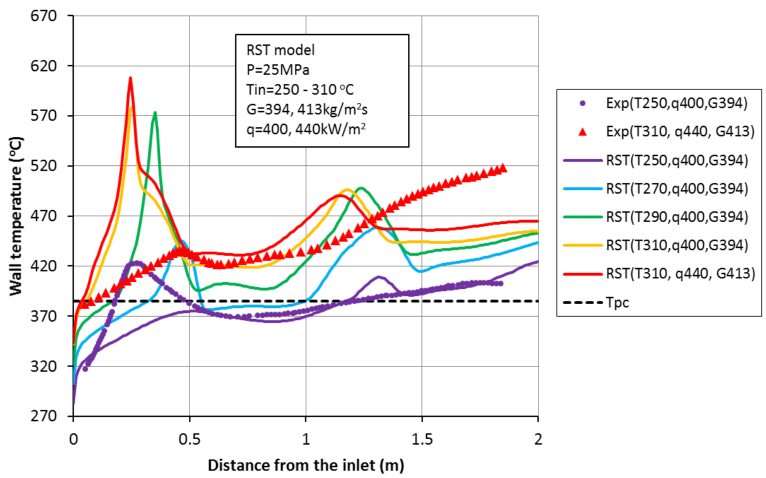

Figure 82 Effect of Inlet Temperature by RST

It can be seen from Figure *82* that the transition from $T_b<T_w<T_{pc}$ to $T_b<T_{pc}<T_w$ predicted by RST model is smooth and no discontinuity is observed. The increase in inlet temperature acts to raise the temperature profile and move the locations where T_w exceeds T_{pc} upstream. Consequently, the predicted temperature peaks move upstream and become more pronounced.

It can be seen that the two temperature peaks when $T_b<T_{pc}<T_w$ evolve from the small bumps where T_w crosses T_{pc}, and RST model is predicting the same type of HTD throughout this study, i.e. the one occurs when wall temperature exceeds T_{pc}. Somehow, RST model fails to predict the HTD correctly in cases where T_w never exceeds T_{pc}, while SLR and other low-Reynolds k-ε models seems better in this aspect. The difference between the predicted physics by RST and SLR models are discussed in the following section. Further investigation on this issue is still needed.

5.5 HTD Mechanism Study for H_2O

The previous HTD mechanism study for CO_2 explains the onset of HTD and its subsequent recovery using RST model in a case where $T_b<T_{pc}<T_w$. The results are also compared to SST and SLR models under the same flow condition. After the above discussion, it is clear that the performance of turbulence models in predicting HTD when $T_b<T_w<T_{pc}$ is quite different from that when $T_b<T_{pc}<T_w$. RST model is not predicting the HTD correctly in almost all the H_2O cases in Watts's experiments, while SLR model is able to both qualitatively and quantitatively predict the onset of HTD in some of these cases, but it tends to overestimate the downstream wall temperatures. On the other hand, SLR model shows such a poor performance in the previous CO_2 study, it is by no means certain that SLR will predict the physics of HTD accurately in these cases. Therefore, in this section, instead of doing a detailed mechanism study using SLR or RST model, the main focus of this section is to understand why RST model is different from SLR in predicting the HTD especially when $T_b<T_w<T_{pc}$.

5.5.1 SLR model

The two cases selected for the mechanism study of SLR model are shown in Figure *83*. The axial wall temperature profiles are re-plotted against axial location, i.e. x/D. The one at mass flux of 261kg/m^{2}s can be used to investigate why SLR model tends to over-predict the downstream wall temperatures at higher heat-flux-to-mass-flux ratio, while another case with several different heat flux, i.e. q=175±5kW/m^2, G=280kg/m^{2}s is used to study the predicted second temperature peak which is not observed in experiments.

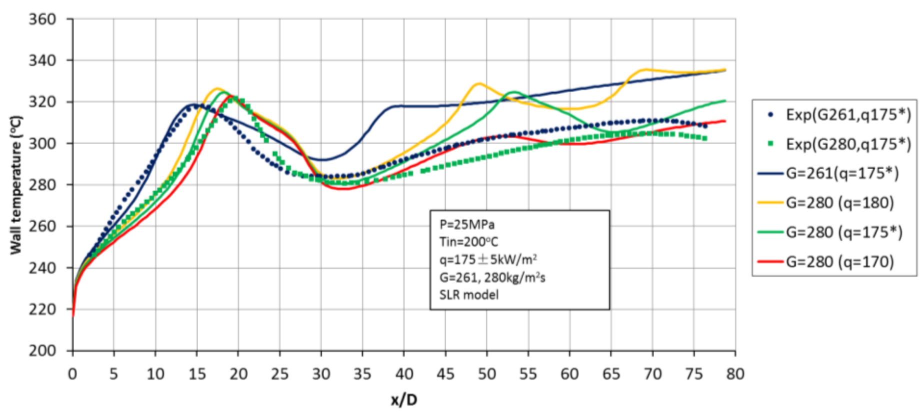

Figure 83 HTD predicted by SLR model for H_2O

<u>G=261kg/m^{2}s, q=175kW/m^2</u>

1) First temperature peak

The first temperature peak at mass flux of 261kg/m^{2}s is studied using the radial distributions of fluid properties at about 20 selected locations within 0<x/D<31, see Figure *84* and Figure *85*.

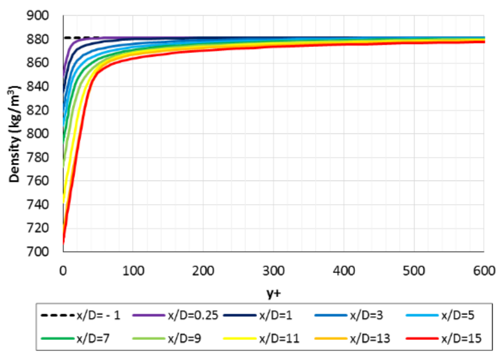

(a1) Density (onset)

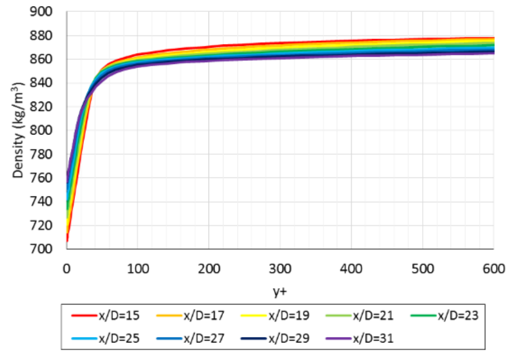

(a2) Density (recover)

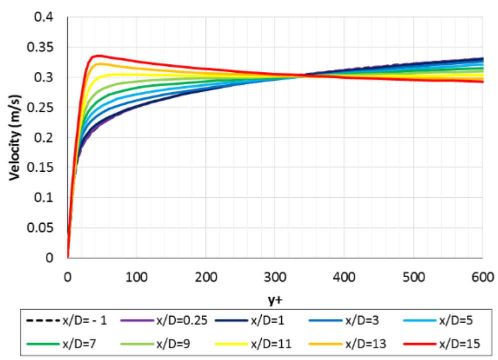

(b1) Velocity (onset)

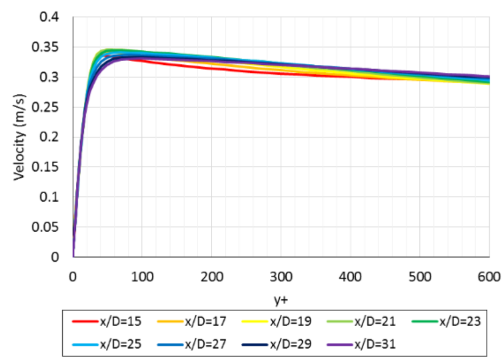

(b2) Velocity (recover)

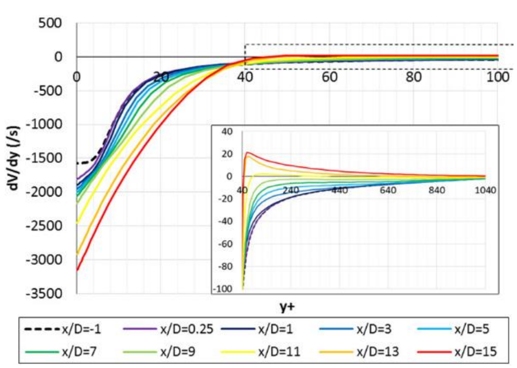

(c1) Velocity Gradient (onset)

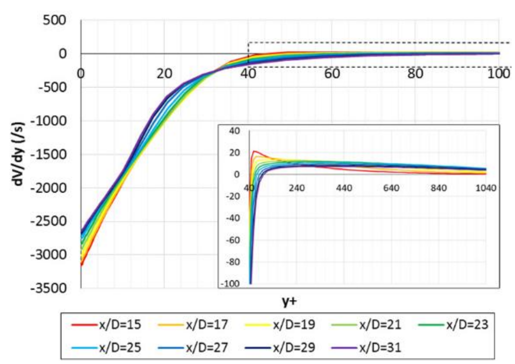

(c2) Velocity Gradient (recover)

Figure 84 Radial distribution of fluid properties at G=261 by SLR – 1st peak

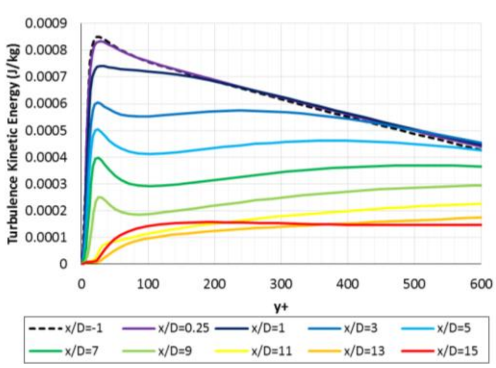

(a1) Turbulence Kinetic Energy (onset)

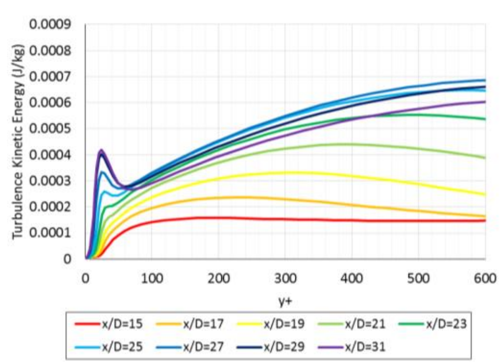

(a2) Turbulence Kinetic Energy (recover)

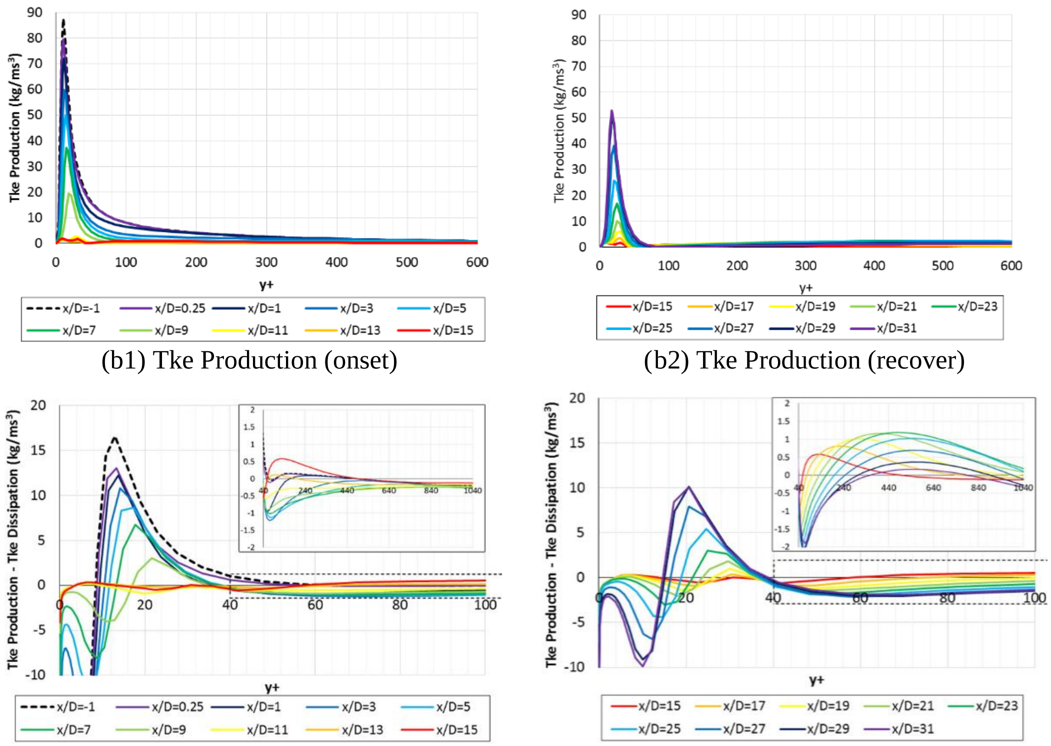

(b1) Tke Production (onset) (b2) Tke Production (recover)

(c1) Tke Net Production (onset) (c2) Tke Net Production (recover)

Figure 85 Information on turbulence at G=261 by SLR – 1st peak

It can be seen that the mechanisms for the onset of HTD and its subsequent recovery in this case are similar to that predicted by RST and SST models in the previous CO_2 study. The acceleration of the near-wall low-density layer caused by the buoyancy force increases the shear stress in the near-wall region while decreasing it everywhere else (Figure *84* c1), which leads to the impairment of turbulence production (Figure *85* b1, c1), resulting in the onset of HTD. When the velocity of the low-density fluid is further increased, it begins to move faster than the high-density fluid in the core, exerting an upward force on the fluid in the core, which makes the velocity profile distort into the M-shape (Figure *84* b2). The shear stress in the core changes its sign (becomes positive) and starts to increase (Figure *84* c2), which restores the turbulence production in both near-wall and core regions (Figure *85* b2, c2), leading to the recovery of HTD.

Despite of the above similarities, there is a significant difference between the H_2O case here and the CO_2 case. Comparing the (net) production of turbulence kinetic energy in these two studies (H_2O: Figure *85* b1, c1; CO_2: *Figure 54* c1, d1), it is clear that there is no “entrance effect” in the H_2O case (recall that the entrance effect in CO_2 caused an immediate reduction in turbulence at the entrance, followed by some recovery). For the H_2O case where $T_w<T_{pc}$ the production of turbulence decreases monotonously as the low-density layer develops, and reaches the minimum at a location close to the peak temperature (in CO_2 case it reaches minimum in a very short distance from the inlet). This

difference is attributed to the much lower density difference within the wall region in the H_2O case, as the wall temperature does not approach T_{pc}.

In the CO_2 case (see section 5.3.1 for details), T_w exceeds T_{pc} almost as soon as the flow enters the inlet of heated section, which suggests that the density of fluid in the wall-layer will drop rapidly. This drastic decrease in density in the wall-layer accelerates the near-wall fluid (probably due to thermal expansion rather than buoyancy), reducing the shear stress everywhere except the viscous sublayer y+<6 (Figure *53* e1, f1), which significantly impairs the near-wall turbulence production.

In the H_2O case here, the decrease in density in the wall-layer is much lower (Figure *84* a1), because the variation of density far from T_{pc} is much smaller than that in the vicinity of T_{pc} (Figure *3*). As a result, the velocity profile does not change significantly when flow enters the inlet. But as the flow proceeds downstream, the low-density layer grows thicker and its density decreases continuously (Figure *84* a1), thus the buoyancy force exerted on the low-density layer becomes greater. The velocity near the wall increases, while that in the core decreases, resulting in a flattened velocity profile, which eventually leads to the onset of HTD.

2) Overestimation of all downstream temperatures

After the recovery of HTD, the wall temperature predicted by SLR model starts to rise again and maintains at a higher level than that measured in experiments, overestimating all downstream wall temperatures. In order to gain a deeper insight into this behavior, the variation of fluid properties after the recovery of first peak from x/D=32 to x/D=70 is studied. The radial distributions of fluid properties at various locations within this range are shown in Figure *86* (a-f).

The velocity profile after the recovery of first peak takes up the M-shape, and the variation in the vicinity of the maxima is gradual (Figure *84* b2). As the flow moves downstream, the density in the near-wall layer decreases further, resulting in a greater density difference, see Figure *86* a. As a result, the velocity near the wall is further increased. The variation of velocity in the vicinity of maxima becomes less gradual, see Figure *86* b. Consequently, the shear stress within 35<y+<100 decreases (Figure *86* c), which impairs the turbulence production near the wall 10<y+<70 (Figure *86* e, f) leading to the onset of the second deterioration.

It can be seen that the cause of second HTD in this case is very different from that in the CO_2 case predicted by RST and SST. In the CO_2 case, the onset of second temperature peak is caused by the decrease in shear stress and turbulence production in the core region, because the velocity profile shifts away from the M-shape due to the decrease in density difference (see section 5.3.1 for details). But in this case, the velocity profile does not change appreciably, except that its edge near the wall becomes sharper.

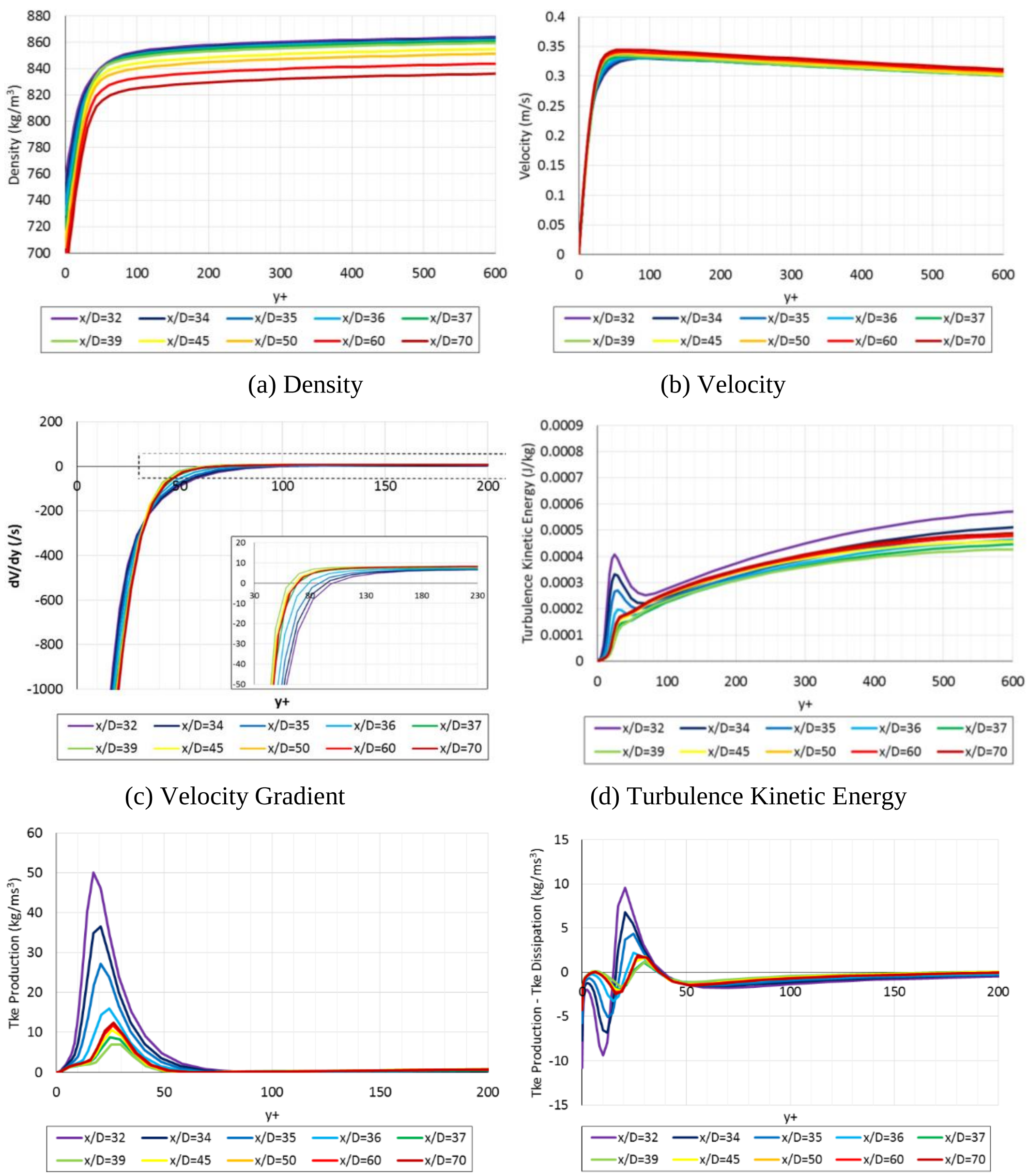

(a) Density

(b) Velocity

(c) Velocity Gradient

(d) Turbulence Kinetic Energy

(e) Tke Production

(f) Tke Net Production

Figure 86 Radial distribution of fluid properties at G=261 by SLR – downstream

G=280kg/m^{2}s, q=175 ±5kW/m^2

The sensitivity study of heat flux in section 5.4.3 reveals that the second peak is very sensitive to heat flux, and seems to be the prelude to the full laminarization of the downstream flow which is observed at lower mass flux (G=261kg/m^{2}s) as discussed above. Therefore, we investigate the G=280kg/m^{2}s case where SLR model predicts a second peak at x/D=53 but does not observe the significant bias in the downstream portion (Figure *83*). The results are shown in Figure *87*.

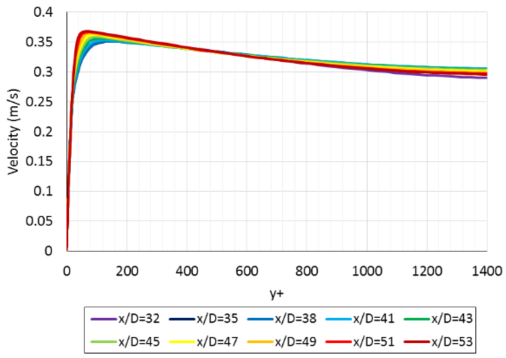

(a1) Velocity (onset)

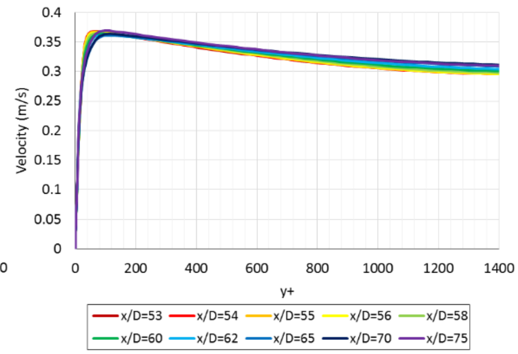

(a2) Velocity (recover)

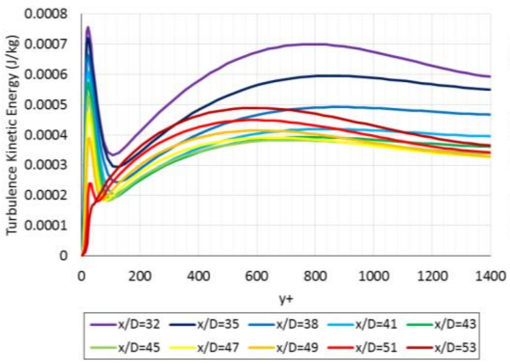

(b1) Turbulence Kinetic Energy (onset)

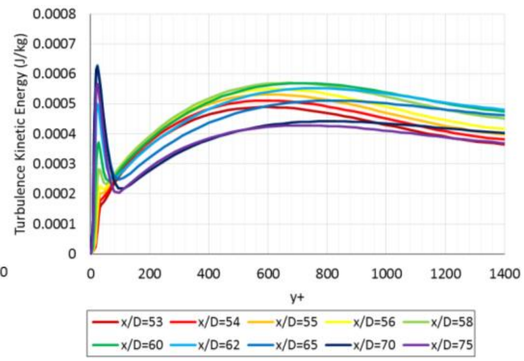

(b2) Turbulence Kinetic Energy (recover)

Figure 87 Second temperature peak at G=280, q=175 by SLR model

From Figure *87* a1, a2, it can be seen that the modification of velocity profile in the vicinity of maxima (near the wall) should be responsible for the onset of second temperature peak and its recovery. When the velocity profiles become sharper in the vicinity of maxima, the turbulence kinetic energy near the wall is reduced substantially (Figure *87* b1), leading to the onset of second deterioration. When the variation of velocity becomes more gradual in the vicinity of maxima, turbulence is regenerated (Figure *87* b2) which helps recover the wall temperature. It can be concluded that the cause of the onset of second peak here is the same as that at G=261kg/m^{2}s as discussed above.

Figure *88* to Figure 90 show the evolution of turbulence kinetic energy as the heat flux increases at G=280kg/m^{2}s. Clearly, in order to reproduce the measured wall temperature, the turbulence near the wall should not be impaired after the recovery of first HTD, i.e. the downstream turbulence kinetic energy near the wall at heat flux of 175kW/m^2 should stay at the same level as that at slightly lower heat flux (q=170kW/m^2, Figure *88*). However, with only a small increase in heat flux, the downstream turbulence near the wall is reduced significantly. It seems that the velocity profile predicted by SLR model tends to take up a “sharp-M-shape” (Figure *92*), which will impair the near-wall turbulence production. Turbulence is thus suppressed throughout the downstream section (Figure *91*), resulting in the overestimation of all downstream wall temperatures.

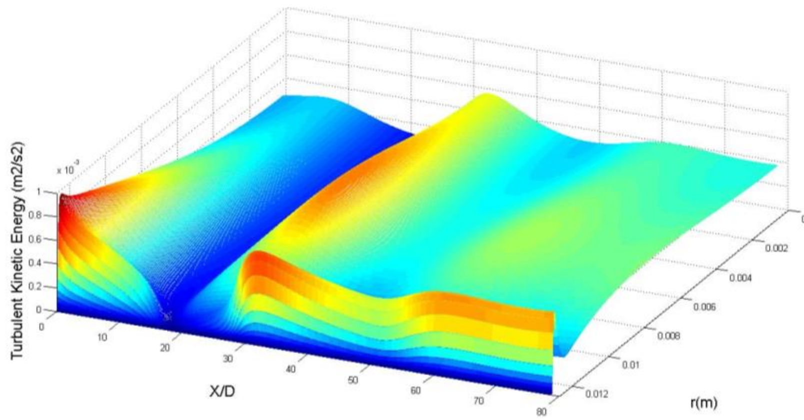

Figure 88 Surface plot of turbulence kinetic energy at G=280kg/m^{2}s, q=170kW/m^2

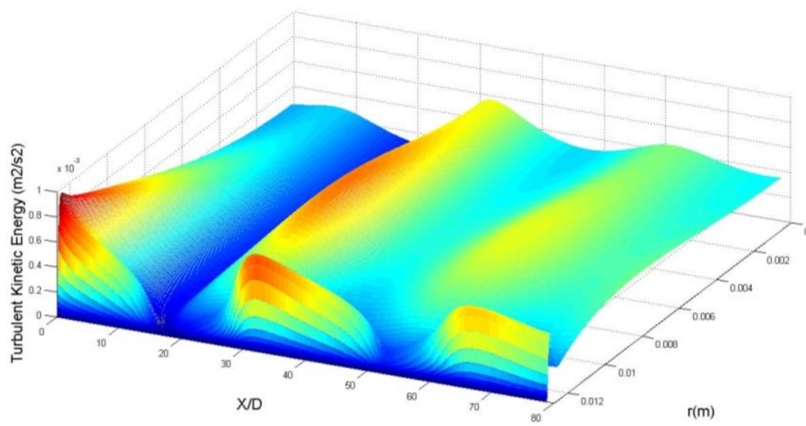

Figure 89 Surface plot of turbulence kinetic energy at G=280kg/m^{2}s, q=175kW/m^2

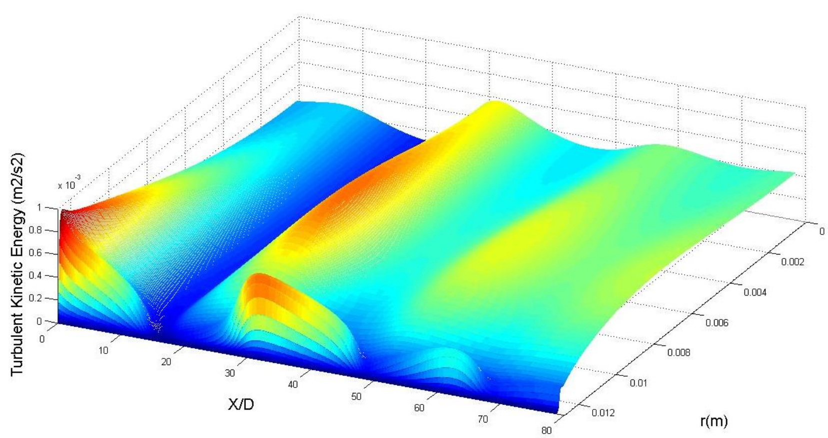

Figure 90 Surface plot of turbulence kinetic energy at G=280kg/m^{2}s, q=180kW/m^2

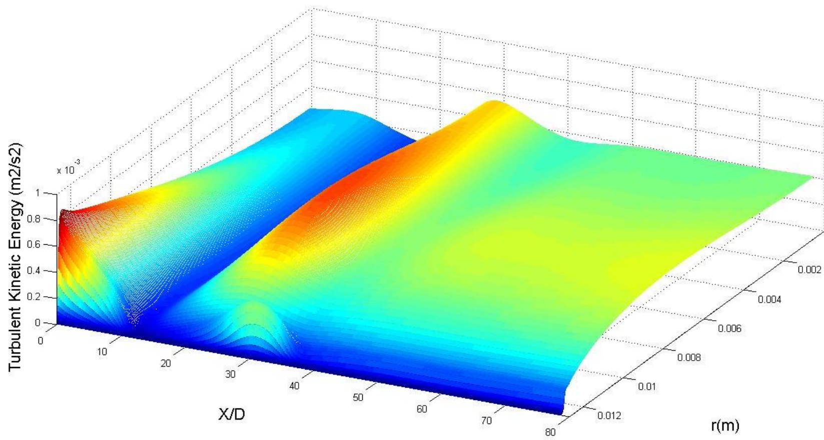

Figure 91 Surface plot of turbulence kinetic energy at G=261kg/m^{2}s, q=175kW/m^2

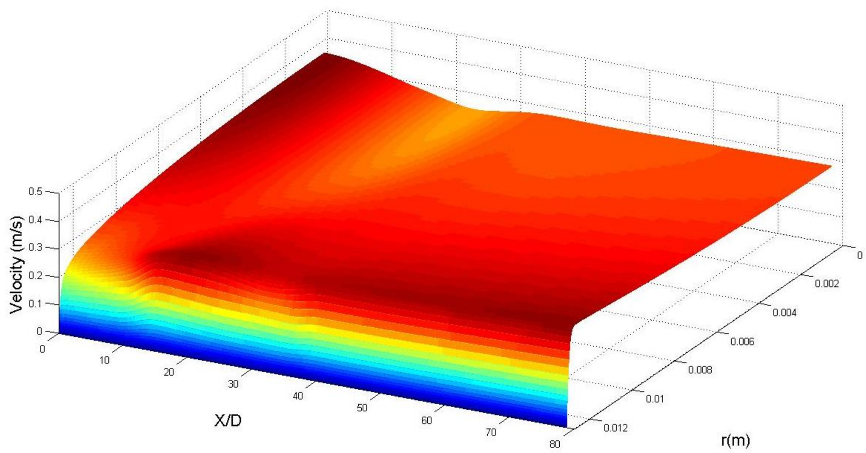

Figure 92 Surface plot of velocity at G=261kg/m^{2}s, q=175kW/m^2

5.5.2 RST model

RST and SST models significantly underestimated the peak temperature and the downstream wall temperatures in cases where wall temperatures are below T_{pc}. A typical case with T_w<T_{pc} is chosen to investigate this behavior using RST model. The axial wall temperatures are re-plotted against x/D in Figure *93*. Again, about 20 axial locations are selected within 0<x/D<31 to study the variation of fluid properties and turbulence distribution, see Figure *94* and Figure *95*.

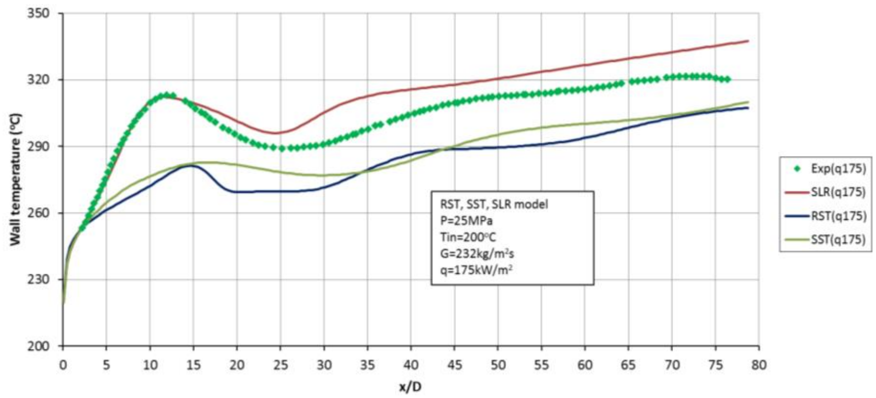

Figure 93 HTD predicted by RST, SST and SLR models in a typical case with T_w < T_{pc}

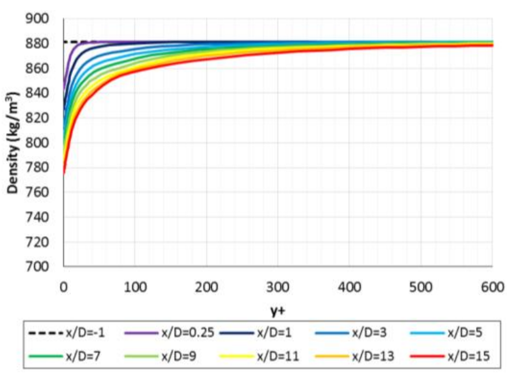

(a1) Density (RST)

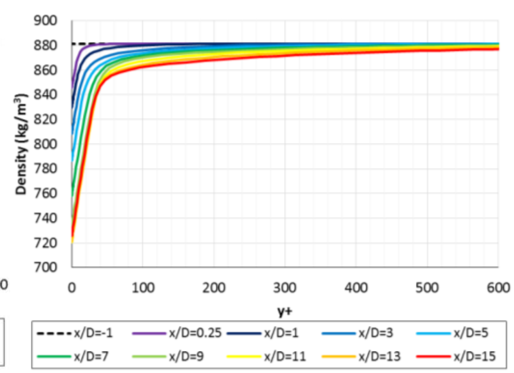

(a2) Density (SLR)

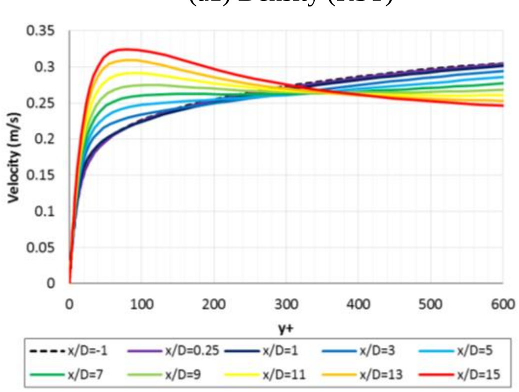

(b1) Velocity (RST)

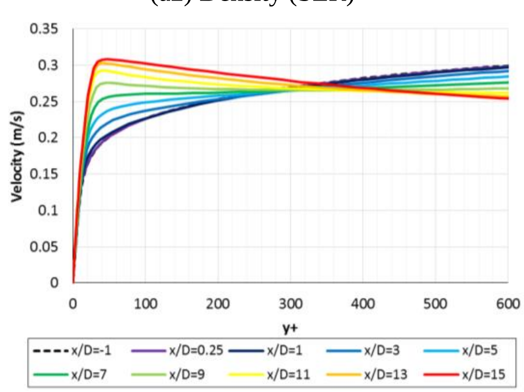

(b2) Velocity (SLR)

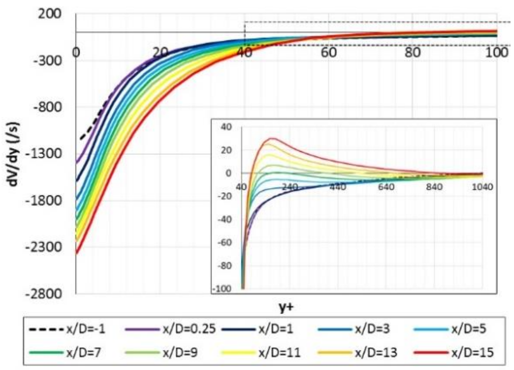

(c1) Velocity Gradient (RST)

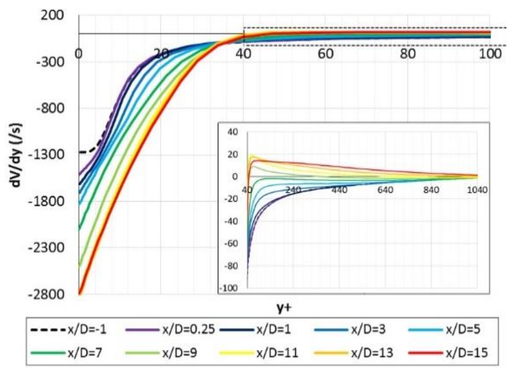

(c2) Velocity Gradient (SLR)

Figure 94 Fluid properties during the onset of HTD by RST and SLR (G=232kg/m^{2}s)

It can be seen from Figure *94* b1 and b2 that the velocity profiles predicted by RST model during the onset of HTD is similar to that predicted by SLR model except that the variation in the near-wall region is much more gradual. The vicinity of maximum velocity (where the velocity gradient is zero) also shifts from y+≈40 (SLR) to y+≈60 (RST).

Figure *95* a1 and a2 show the turbulence kinetic energy (Tke) at different locations predicted by RST and SLR respectively. Before entering the heated section, the Tke predicted by two models are very similar. The RST model predicts a peak in the buffer layer at all axial locations, while SLR model does not. This behavior is also observed in the previous CO_2 case. Nevertheless, the peak of Tke predicted by RST model in this case is not impaired as much as that in the CO_2 case where the peak Tke is reduced by a factor of three. In other words, the Tke in the buffer layer in this case is overestimated which leads to the underestimation of HTD. This is attributed to the abnormally high turbulence production in the near-wall region (Figure *95* b1). The net turbulence production predicted by SLR model decreases continuously during the onset of HTD (Figure *95* c2), while that predicted by RST decreases at the very beginning then rebounds to a level that is almost ten times higher (Figure *95* c1).

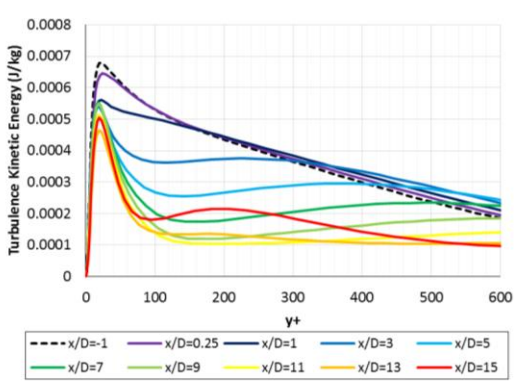

(a1) Turbulence Kinetic Energy (RST)

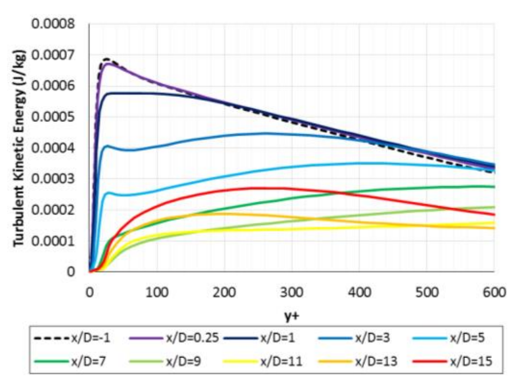

(a2) Turbulence Kinetic Energy (SLR)

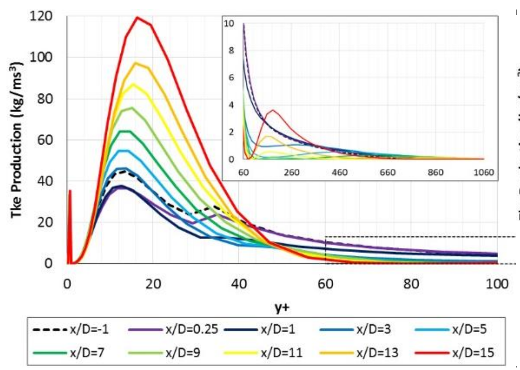

(b1) Tke Production (RST)

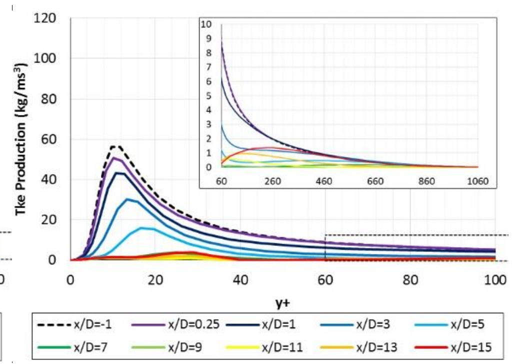

(b2) Tke Production (SLR)

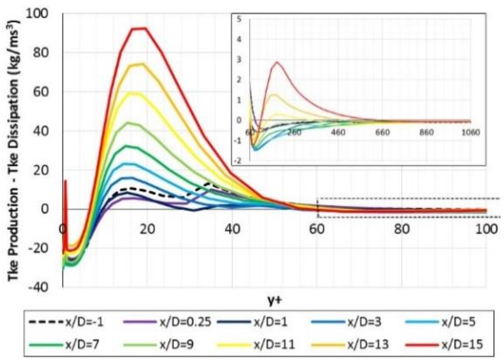

(c1) Tke Net Production (RST)

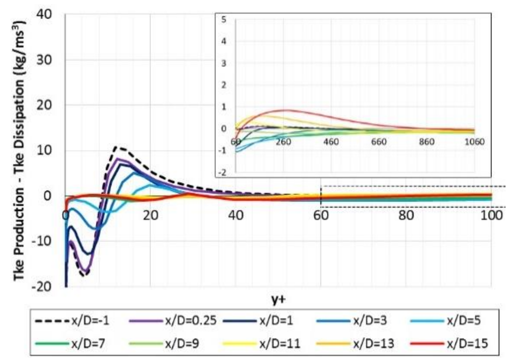

(c2) Tke Net Production (SLR)

Figure 95 Information on turbulence during the onset of HTD by RST and SLR (G=232 kg/m^{2}s)

It is suspected that this abnormally high turbulence production is resulting from the too-gradual velocity variation in the near-wall region which may be caused by the smaller density difference between near-wall and core regions (Figure *94* a1). Although, SLR model predicts the onset of HTD both qualitatively and quantitatively in this case, it is by no means certain that SLR is predicting the turbulence correctly, as it shows relatively poor performance when $T_b<T_{pc}<T_w$. It would be helpful if the distributions of turbulence kinetic energy from experiments or DNS are available, especially in the near-wall region where HTD occurs.

6. Conclusions and Future Work

6.1 Performance of Different Turbulence Models in predicting HTD

In order to predict the HTD caused by buoyancy force, the viscous sub-layer need to be properly resolved. Several turbulence models that can resolve the viscous sub-layer are compared in this thesis. All the turbulence models reproduce the wall temperatures very well at relatively low heat flux where no HTD occurs. Discrepancy increases at higher heat flux and in the presence of HTD. The k-ε models with two-layer approach, i.e. STO and RTO, fail to predict the HTD in all the cases. The k-ε models with low-Reynolds number approach, i.e. SLR and AKN, are able to predict the HTD qualitatively in both CO_2 and H_2O experiments ($T_b<T_{pc}<T_w$ and $T_b<T_w<T_{pc}$), but the peak and downstream temperatures are often overestimated especially when $T_b<T_{pc}<T_w$. In the CO_2 study, the recovery predicted by SLR and AKN does not show up until T_b is close to T_{pc}, and they both start to predict the HTD at heat fluxes well below that observed in experiments. RST and SST model in some cases predict the HTD in a very good agreement with the experiment when $T_b<T_{pc}<T_w$, and they are far less sensitive to the heat flux. However, they start to predict the HTD at higher heat flux than observed experimentally. Another drawback of RST and SST is that they both fail to predict the HTD when $T_b<T_w<T_{pc}$. The k-ω model by Wilcox (WI) is very similar to SST model, except that it fails to predict the second temperature peak in the CO_2 study. SLR is suggested for cases with $T_b<T_w<T_{pc}$, while RST is the optimal choice for deteriorated heat transfer when $T_b<T_{pc}<T_w$.

6.2 Mechanism of Buoyancy-induced HTD

The mechanism of HTD in the CO_2 study is first explained thoroughly using RST model. Not all the obtained results are consistent with Jackson's buoyancy theory which is widely used in other CFD studies to explain the HTD. First, the "entrance effect" has not been discussed in detail by other researchers. Most authors postulate that the low density layer needs to grow sufficiently thick in order to materially reduce the shear stress thus turbulence production in the buffer layer. But what we observe here is that the near-wall turbulence production is already impaired when the low-density layer is still limited to the viscous sublayer. The flow acceleration due to thermal expansion is found to play a more important role than that due to buoyancy in causing the "entrance effect". Second, turbulence production is partly regenerated in the buffer layer due to the increase in local shear stress during the onset of HTD. This is not again expected, as other researchers believe that the increase in near-wall shear stress is usually in region where turbulence is damped out by the wall, thus will not give rise to the increase in turbulence production. SST and SLR models predict no regeneration of turbulence production during the onset of HTD, which explains why they over-predict the peak temperatures. The recovery predicted by RST and SST are very similar, hence they predict a similar temperature trend; while SLR fails to restore the turbulence after the onset of HTD, therefore the downstream wall temperature is significantly overestimated.

The causes of the HTD when $T_b<T_w<T_{pc}$ in the H_2O study obtained using SLR model, are very similar to that in the CO_2 case ($T_b<T_{pc}<T_w$), except that no "entrance effect" is observed. The turbulence production drops gradually as the low-density layer develops, which is attributed to weaker density variation as T_w is below T_{pc}. SLR and other low-Reynolds models tend to over-predict the downstream wall temperatures at lower mass fluxes when $T_b<T_w<T_{pc}$, because turbulence is impaired after the recovery of first temperature peak. RST predicts an abnormally strong regeneration of turbulence in the buffer layer during the onset of HTD, which makes it overestimate the near-wall turbulence level, leading to the underestimation of wall temperatures.

6.3 Future Work

Many numerical studies have been carried out by different researchers, but there is still a big deficiency in the prediction of heat transfer to supercritical fluids. The understanding of heat transfer phenomena such as HTD is also limited. In this thesis, the Reynolds stress transport (RST) model predicted the HTD in an excellent agreement with data from the CO_2 experiment, and it is able to give more reasonable explanation on the mechanism of HTD. However, its performance in the H_2O study is not so satisfactory. It is difficult to tell which model is predicting the physics, in particular the turbulence, better, as the distributions of velocity and turbulence especially in the very near-wall region from experiments are still lacking. RST is clearly superior to EVM models for situation where the anisotropy of turbulence has a dominant effect on the mean flow. Whether it is necessary to adopt RST model for supercritical fluid flow in circular pipes, further study is needed.

The performance of turbulence models varies with the change of flow conditions, a continuing assessment of different turbulence models for the applicability to supercritical fluid flow is still necessary. The simulated cases in this thesis are limited to buoyancy-induced HTD, hence it is worthwhile to further investigate other modes of heat transfer, i.e. heat transfer enhancement, or acceleration-induced HTD.

Much more effort is needed to improve the turbulence models to give more reliable predictions under supercritical pressures. It has been recognized that the quality of the boundary layer characteristics predicted by turbulence models is vital important for the accurate prediction of wall temperature. Attention should be focused on the improvement of turbulence model in better resolving the boundary layer. Further investigation on the two-layer approach is necessary.

References

[1] "Origins of the GIF," Generation IV International Forum, [Online]. Available: https://www.gen-4.org/gif/jcms/c_9334/origins. [Accessed March 2014].

[2] M. Yetisir, W. Diamond, L. K. Leung, D. Martin and R. Duffey, "Conceptual Mechanical Design for a Pressure-Tube Type Supercritical Water-Cooled Reactor," in *The 5th Int. Sym. SCWR*, Vancouver, British Columbia, Canada, 2011.

[3] L. K. Leung, "Thermalhydraulics and Safety-Related Experiments in support of the Canadian SCWR Concept Development," in *Canada-China Conference on Advanced Reactor Development*, Niagara Falls, Canada, 2014.

[4] "Canada's National Program on Generation IV Energy Technologies - Research and Development Priorities for 2012–16," Natural Sciences and Engineering Research Council of Canada, 2012. [Online]. Available: http://www.nserc-crsng.gc.ca/Professors-Professeurs/RPP-PP/GENIV0809Priorities-GENIV0809Priorites_eng.asp. [Accessed March 2014].

[5] S. Gopaul, V. Hopps, C. Jacobs, M. Khan, R. Patkunam and I. L. Pioro, "Some Design Features of SCW Pressure-Tube Nuclear Reactor," in *Proceedings of the 15th International Conference on Nuclear Engineering*, Nagoya, Japan, 2007.

[6] E. W. Lemmon, M. L. Huber and M. O. McLinden, "NIST Standard Reference Database 23, Version 9.1," Applied Chemicals and Meterials Division, United States of America, 2013.

[7] CD-adapco, "STAR-CCM+ v8.06.005 User Guide," US, 2013.

[8] H. Zahlan, K. Jiang, K. Tavoularis and D. Groeneveld, "Measurements of heat transfer coefficient, CHF and heat transfer deterioration in flows of CO2 at near-critical and supercritical pressures," in *The 6th International Symposium on Supercritical Water-Cooled Reactors, ISSCWR-6*, Shenzhen, Guangdong, China, 2013.

[9] J. D. Jackson, "The Supercritical Pressure Water Heat Transfer Study at Manchester with a Natural Circulation Test Facility," IAEA Coordinated Research Programme (CRP), 2009.

[10] J. D. Jackson and W. B. Hall, "Forced convection heat transfer to fluids at supercritical pressureTurbulent Forced Convection in Channels and Bundles," *Hemisphere Publishing Corporation,* p. 563–611, 1979.

[11] J. D. Jackson and W. B. Hall, "Influences of buoyancy on heat transfer to fluids flowing in vertical tubes under turbulent conditions," in *Advanced Study Institute Book: Turbulent Forced Convection in Channels and Bundles*, 1979, p. 613–640.

[12] J. Licht, M. Anderson and M. Corradini, "Heat transfer to water at supercritical pressures in a circular and square annular flow geometry," *International Journal of Heat and Fluid Flow,* vol. 29, no. 1, p. 156–166, 2008.

[13] M. E. Shitsman, "Natural convection effect on heat transfer to a turbulent water flow in intensively heated tubes at supercritical pressures," in *Proc. I. Mech. E.*, Ibid., 1968.

[14] W. B. Hall, J. D. Jackson and A. Watson, "A review of forced convection heat trans- fer to fluids at supercritical pressures," in *Proc. I. Mech. E.*, Bristol Symposium, 1968.

[15] W. B. Hall and J. D. Jackson, "Laminarisation of a turbulent pipe flow by buoyancy forces," in *ASME AIChE National Heat Transfer Conference*, Minneapolis, MN, USA, 1969.

[16] J. D. Jackson, "Fluid flow and convective heat transfer to fluids at supercritical pressure," *Nuclear Engineering and Design,* vol. 264, no. 1, pp. 24-40, 2013.

[17] J. D. Jackson, "Validation of an Extended Heat Transfer Equation for Fluids at Supercritical Pressure," in *4th ISSCWR*, Heidelberg, Germany, 2009.

[18] B. S. Shiralkar and P. Griffith, "Deterioration in heat transfer to fluids at supercrit- ical pressure and high heat fluxes," *A.S.M.E., J. Heat Transfer,* pp. 27-36, 1969.

[19] B. Shiralkar and P. Griffith, "The effect of swirl inlet conditions, flow direction and tube diameter on the heat transfer to fluids at supercritical pressure," *J. Heat Transfer,* vol. 92, pp. 465-474, 1970.

[20] W. B. Hall, "Forced Convective Heat Transfer to supercritical pressure fluid," *Arch Termodyn Spalania* , vol. 6, p. 341–352, 1975.

[21] X. Cheng and T. Schulenberg, "Heat Transfer at Supercritical Pressures - Literature Review and Application to an HPLWR," Institut für Kern- und Energietechnik, 2001.

[22] I. L. Pioro and R. B. Duffey, "Experimental heat transfer in supercritical water flowing inside channels (survey)," *Nuclear Engineering and Design,* vol. 235, no. 22, p. 2407–2430, 2005.

[23] I. L. Pioro and R. B. Duffey, "Experimental heat transfer of supercritical carbon dioxide flowing inside channels (survey)," *Nuclear Engineering and Design,* vol. 235, no. 8, p. 913–924, 2005.

[24] M. E. Shitsman, "Impairment of the heat transfer at supercritical pressures," *High Temper. (Translated from Teplofzika Vysokikh Temperaur),* vol. 1, no. 2, pp. 267-275, 1963.

[25] H. S. Swenson, J. R. Carver and C. R. Kakarala, "Heat transfer to supercritical water in smooth-bore tubes," *Journal of Heat Transfer: Transactions of the ASME Series C 87 (4),* vol. 87, no. 4, p. 477–484, 1965.

[26] A. A. Bishop, R. O. Sandberg and L. S. Tong, "High temperature supercritical pressure water loop: Part IV. Forced convection heat transfer to water at near-critical temperatures and super-critical pressures," Westinghouse Electric Corporation, Pittsburgh, PA., 1964.

[27] J. W. Ackerman, "Pseudoboiling Heat Transfer to Supercritical Pressure Water in Smooth and Ribbed Tubes," *Journal of Heat Transfer,* vol. 92, no. 3, pp. 490-497, 1970.

[28] A. P. Ornatsky, L. P. Glushchenko and E. T. Siomin, "The research of temperature conditions of small diameter parallel tubes cooled by water under supercritical pressures," in *Proceedings of the 4th International Heat Transfer Conference*, Paris, Versailles, France, 1970.

[29] A. P. Ornatskiy, L. F. Glushchenko and S. I. Kalachev, "Heat transfer with rising and falling flows of water in tubes of small diameter at supercritical pressures," *Therm. Eng,* vol. 18, no. 5, pp. 137-141, 1971.

[30] A. P. Ornatskiy, L. F. Glushchenko and O. F. Gandzyuk, "An experimental study of heat transfer in externally-heated annuli at super- critical pressures," *Heat Transfer-Soviet Res.,* vol. 4, no. 6, pp. 25-29, 1972.

[31] K. Yamagata, K. Nishmawa and S. Hasegawa, "Forced Convective Heat Transfer to Supercritical Water Flowing in Tubes," *Int. J. Heat Mass Transfer,* vol. 15, pp. 2575-2593, 1972.

[32] G. V. Alekseev, V. A. Silin, A. M. Smirnov and V. I. Subbot, "Study of the thermal conditions on the wall of a pipe during the removal of heat by water at a supercritical pressure," *High Temp.*, vol. 14, no. 4, pp. 683-687, 1976.

[33] M. J. Watts, "Heat transfer to supercritical pressure water – Mixed convection with upflow and downflow in a vertical tube," PhD Thesis, University of Manchester, 1980.

[34] E. N. Pis'menny, V. G. Razumovskiy, E. M. Maevskiy, A. E. Koloskov and I. L. Pioro, "Heat Transfer to Supercrtical Water in Gaseous State or Affected by Mixed Convection in Vertical Tubes," in *Proceedings of ICONE14*, Miami, Florida, USA, 2006.

[35] J. Licht, M. Anderson and M. Corradini, "Heat transfer to water at supercritical pressures in a circular and square annular flow geometry," *International Journal of Heat and Fluid Flow,* vol. 29, no. 1, pp. 156-166, 2008.

[36] X. Cheng, X. Liu and H. Gu, "Fluid-to-fluid scaling of heat transfer in circular tubes cooled with supercritical fluids," *Nuclear Engineering and Design*, vol. 241, pp. 498-508, 2011.

[37] J. Fewster, "Mixed forced and free convective heat transfer to supercritical pressure fluids flowing in vertical pipes," Ph.D. thesis., University of Manchester, UK, 1976.

[38] J. Fewster and J. D. Jackson, "Experiments on supercritical pressure convective heat transfer having relevance to SPWR," in *Proc. ICAPP'04*, Pittsburgh, PA, USA, 2004.

[39] J. K. Kim, H. K. Jeon, J. Y. Yoo and J. S. Lee, "Experimental study on heat transfer characteristics of turbulent supercritical flow in vertical circular/non-circular tubes," in *Proceedings of the 11th NURETH-11, ,* Avignon, France, 2005.

[40] J. K. Kim, H. K. Jeon and J. K. Lee, "Wall temperature measurement and heat transfer correlation of turbulent supercritical carbon dioxide flow in vertical circular/non-circular tubes," *Nuclear Engineering and Design,* vol. 237, no. 15-17, pp. 1795-1802, 2007.

[41] Y. Y. Bae, "Mixed convection heat transfer to carbon dioxide flowing upward and downward in a vertical tube and an annular channel," *Nuclear Engineering and Design*, vol. 241, no. 8, pp. 3164-3177, 2011.

[42] S. Koshizuka, "Numerical analysis of deterioration phenomena in heat transfer to supercritical water," *Int. J. Heat Mass Transfer,* vol. 38, no. 16, pp. 3077-3084, 1995.

[43] S. He, W. S. Kim, P. X. Jiang and J. D. Jackson, "Simulation of mixed convection heat transfer to carbon dioxide at supercritical pressure," *Proceedings of the Institution of Mechanical Engineers, Part C: Journal of Mechanical Engineering Science,* vol. 218, no. 11, pp. 1281-1296, 2004.

[44] R. Weinberg, "Experimental and theoretical study of buoy- ancy effects in forced convection to supercritical pressure carbon dioxide," PhD thesis, University of Manchester, 1972.

[45] S. He, W. S. Kim and J. D. Jackson, "A computational study of convective heat transfer to carbon dioxide at a pressure just above the critical value," *Applied Thermal Engineering,* vol. 28, no. 13, pp. 1662-1675, 2008.

[46] M. Sharabi, W. Ambrosini, N. Forgione and S. He, "Prediction of Experimental Data on Heat Transfer to Supercritical Water with Two-Equation Turbulence Models," in *3rd ISSCWR*, Shanghai, China, 2007.

[47] W. Ambrosini, "Continuing Assessment of System and CFD Codes for Heat Transfer and Stability in Supercritical Fluids," in *4th ISSCWR*, Heidelberg, Germany, 2009.

[48] M. Sharabi and W. Ambrosini, "Discussion of heat transfer phenomena in fluids at supercritical pressure with the aid of CFD models," *Annals of Nuclear Energy,* vol. 36, no. 1, pp. 60-71, 2009.

[49] D. Palko and H. Anglart, "Theoretical and Numerical Study of Heat Transfer Deterioration in High Performance Light Water Reactor," *Science and Technology of Nuclear Installations,* vol. 2008, no. 2, pp. 1-5, 2008.

[50] L. Liu, Z. Xiao, X. Yan, X. Zeng and Y. Huang, "Heat transfer deterioration to supercritical water in circular tube and annular channel," *Nuclear Engineering and Design,* vol. 255, pp. 97-104, 2013.

[51] H. K. Versteeg and W. Malalasekera, An Introduction to Computational Fluid Dynamics - The Finite Volume Method (Second Edition), Essex, England: Pearson Edu., 2007.

[52] A. A. Townsend, "Equilibrium layers and wall turbulence.," *J. Fluid Mech,* vol. 11, 1961.

[53] B. E. Launder and B. I. Sharma, "Application of the Energy Dissipation Model of Turbulence to the Calculation of Flow Near a Spinning Disc," *Letter in Heat and Mass Transfer,* vol. 1, no. 2, pp. 131-138, 1974.

[54] W. Rodi, "Experience with Two-Layer Models Combining the k-e Model with a One-Equation Model Near the Wall," in *29th Aerospace Sciences Meeting*, Reno, NV, 1991, January 7-10.

[55] D. C. Wilcox, Turbulence Modeling for CFD, 2nd edition, DCW Industries, Inc., 1998.

[56] D. C. Wilcox, "Reassessment of the Scale-determining Equation for Advanced Turbulence Models," *AIAA J.,* vol. 26, no. 11, p. 1299–1310, 1988.

[57] Y. Zhu, "Numerical Investigation of the Flow and Heat Transfer within the Core Cooling Channel of a Supercritical Water Reactor," IKE, University of Stuttgart , Stuttgart, Germany, 2010.

[58] F. R. Menter, "Two-equation eddy-viscosity turbulence modeling for engineering applications," *AIAA Journal,* vol. 32, no. 8, pp. 1598-1605., 1994.

[59] F. R. Menter, "Ten Years of Industrial Experience with the SST Turbulence Model," in *Proceedings of the Fourth International Symposium on Turbulence, Heat and Mass Transfer*, Begell House, Redding, CT., 2003.

[60] B. E. Launder, G. J. Reece and W. Rodi, "Progress in the Development of a Reynolds-stress Turbulence Closure," *J. Fluid Mech.,,* vol. 68, no. 3, p. 537– 566, 1975.

[61] M. Chatharaju, "Computational Study of Critical Flow Discharge in Supercritical Water Cooled Reactors," McMaster Univeristy, Hamilton, ON, Canada, 2011.

[62] W. P. Jones and B. E. Launder, "The Prediction of Laminarization with a Two-Equation Model of Turbulence\u201d,," *Int. J. Heat and Mass Transfer,* vol. 15, pp. 301-314., 1972.

[63] T. H. Shih, W. W. Liou, A. Shabbir, Z. Yang and J. Zhu, "A New k-epsilon Eddy Viscosity Model for High Reynolds Number Turbulent Flows -- Model Development and Validation," NASA TM 106721, 1994.

[64] K. Abe, T. Kondoh and Y. Nagano, "A new turbulence model for predicting fluid flow and heat transfer in separating and reattaching flows --- 1. Flow field calculations," *Int. J. Heat Mass Transfer,* vol. 37, pp. 139-151, 1994.

[65] F. S. Lien, W. L. Chen and M. A. Leschziner, "Low-Reynolds number eddy-viscosity modelling based on non-linear stress-strain/vorticity relations," in *Proc. 3rd Symp. on Engineering Turbulence Modelling and Measurements*, Crete, Greece, 1996, 27-29 May.

[66] D. C. Wilcox, "Formulation of the k-omega turbulence model revisited," *AIAA Journal*, vol. 46, no. 11, pp. 2823-2838, 2008.

[67] M. M. Gibson and B. E. Launder, "Ground effects on pressure fluctuations in the atmospheric boundary layer," *J. Fluid Mech.*, vol. 86, no. 3, pp. 491-511, 1978.

[68] C. G. Speziale, S. Sarkar and T. B. Gatski, "Modelling the pressure-strain correlation of turbulence: an invariant dynamical systems approach," *J. Fluid Mech.*, vol. 227, pp. 245-272., 1991.

[69] D. P. Mikielewicz, A. M. Shehata, J. D. Jackson and D. M. Mceligot, "Temperature, velocity and mean turbulence structure in strongly heated internal gas flows: Comparison of numerical predictions with data," *Internat. J. Heat Mass Transfer*, vol. 45, pp. 4333-4352, 2002.

[70] C. Dang and E. Hihara, "In-tube cooling heat transfer of supercritical carbon dioxide. Part 2. Comparison of numerical calculation with different turbulence models," *International Journal of Refrigeration*, vol. 27, no. 7, pp. 748-760, 2004.

[71] S. He, W. S. Kim and J. H. Bae, "Assessment of performance of turbulence models in predicting supercritical pressure heat transfer in a vertical tube," *International Journal of Heat and Mass Transfer*, vol. 51, no. 19-20, pp. 4659-4675, 2008.

[72] Y. V. Vikhrev, Y. D. Barulin and A. S. Kon'kov, "A study of heat transfer in vertical tubes at supercritical pressures," *Therm. Eng.*, vol. 14, no. 9, p. 116–119., 1967.

[73] M. D. Rosa, "CFD Analysis of Experimental Data on Heat Transfer Deterioration with Supercritical Water," University of Pisa, Italy, 2010.

[74] Y.-Y. Bae and H.-Y. Kim, "Convective heat transfer to CO2 at a supercritical pressure flowing vertically upward in tubes and an annular channel," *Experimental Thermal and Fluid Science*, vol. 33, no. 2, pp. 329-339, 2009.

[75] E. W. Lemmon, M. L. Huber and M. O. McLinden, "NIST Standard Reference Database 23, Version 9.1," Applied Chemicals and Materials Division, Boulder, USA.

Appendix

1. Rerun one case from Sharabi et al. with artificially increased heated length

1.1 Quick Review

The case that are re-run by the author is from Sharabi 2007 [45] and Ambrosini 2009 [46], detailed information on these two studies can be found in Table *1* in the chapter of literature review. They both uses Pis'menny's experimental data [33] (Figure *10*) which was obtained at pressure of 23.5MPa on supercritical water.

The main results and flow condition are show in the following figures. The mass flux G should be 509 kg/m^{2}s rather than 590 kg/m^{2}s, which may be a typo by the authors.

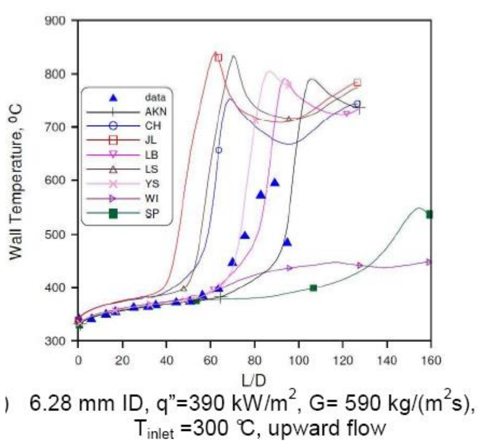

Figure 96 Sharabi's results (in-house code)

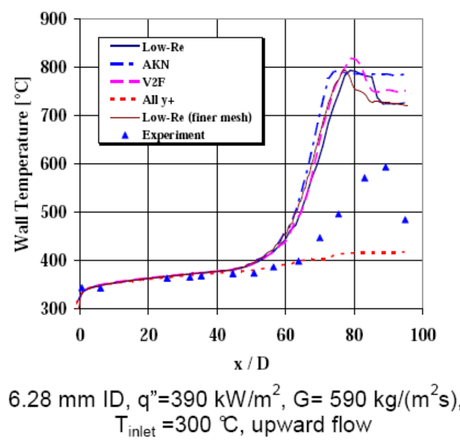

Figure 97 Ambrosini's results (STAR-CCM+)

Their main conclusions that I think is important are listed as follows:

1. All the k-ε low-Reynolds were found to be able to qualitatively predict the HTD, but with significant over-estimation of wall temperature.
2. Both k-ω and k-τ model fail to respond to HTD at relatively low heat flux, however with the increase in heat fluxes k-ω model starts to respond to HTD.
3. The two-layer approach (all y+) is not able to catch laminarization.
4. The predicted HTD is caused by buoyancy which redistributes the flow by increasing the velocity close to the wall and decreasing it in the core. The shear stresses in the buffer region is reduced, leading to onset of HTD. However, with further increase in buoyancy, the production of turbulence is restored by the reversed M-shape velocity profile.

1.2 New results by the author in STAR-CCM+

Based on the conclusions in this present thesis, it is suspected that the k-ω model is able the respond to HTD at slightly higher heat fluxes, and the mild recovery after the peak temperature predicted by low-Re k-ε model should not be considered as a real recovery, which in fact comes much later when the bulk fluid is heated up close to T_{pc} at further downstream. It is also worth noting that the turbulent Prandtl number in their studies uses a constant value of 0.85, instead of 0.9, however, the results should not be sensitive to Pr_t.

With all these in mind, the same experiment is simulated with identical flow conditions (some cases use artificially increased heated length, some not) in STAR-CCM+ by the author, the results of which are shown in the following figures.

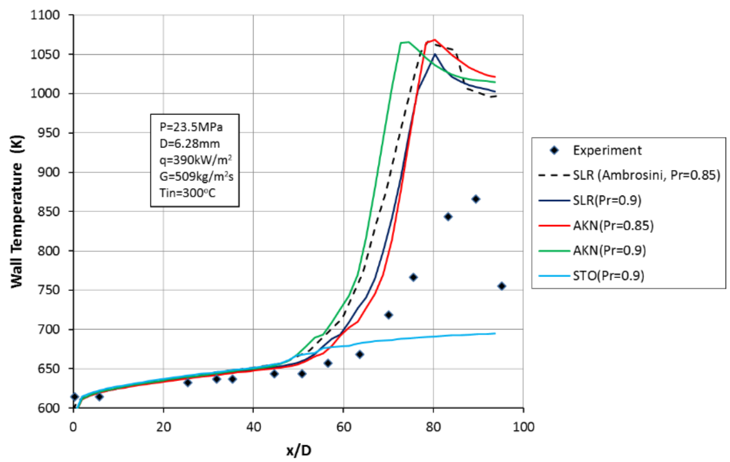

Figure 98 Validation of current CFD setting against Ambrosini's results

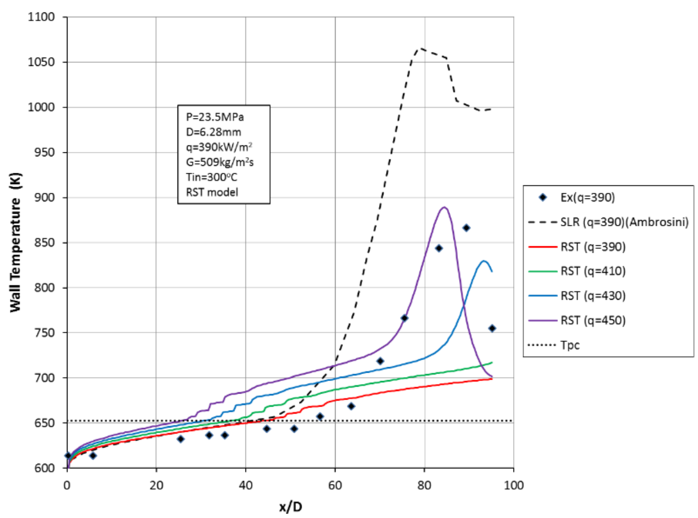

Figure 99 Performance of RST model with increasing heat flux

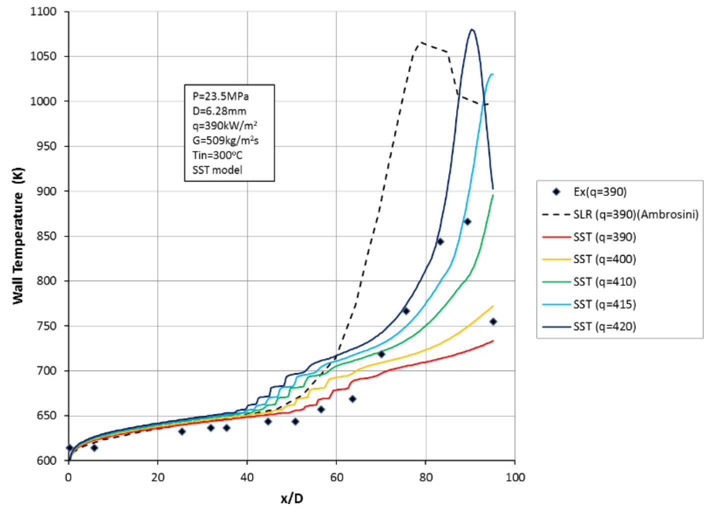

Figure 100 Performance of SST model with increasing heat flux

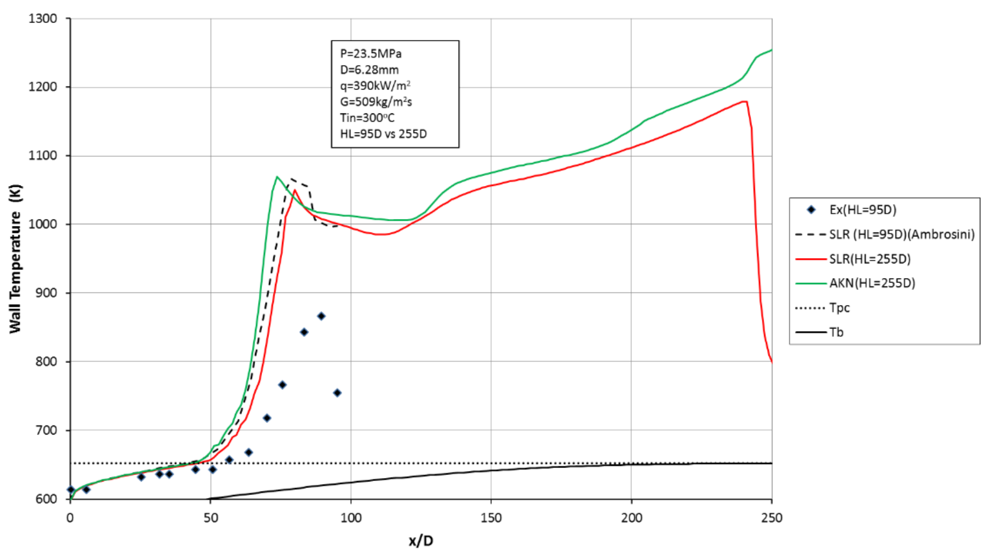

Figure 101 Low-Reynolds number model with added heated length

From the above figures, it is quite clear that all those hypotheses have been proved:

1. Both RST and SST is able the respond to HTD at higher heat fluxes.
2. The mild recovery after the peak temperature predicted by SLR and AKN (both are low-Reynolds number k-ε model) is not a real recovery, which in fact comes much later when the bulk fluid is heated up close to T_{pc} further downstream.
3. The results are not sensitive to turbulent Prandtl number, but it indeed can be used to get better results by tuning its value.

All these conclusions are consistent with what have been found in this thesis as shown in the body of this thesis, which gains us more confidence in these results.

2. Rerun Several Cases with $T_w<T_{pc}$ from He et al.

2.1 Quick Review

Simulated Experiments:

Weinberg, R. Experimental and theoretical study of buoyancy effects in forced convection to supercritical pressure carbon dioxide. PhD thesis, University of Manchester, 1972

Experimental Parameters:

Medium	Diameter	Unheated/Heated length	Pressure	T_{pc}
CO_2	19mm	64D/129D	7.58MPa	32.2°C

Reference:

He, S., Kim, W. S., Jiang, P. X., & Jackson, J. D. (2004). Simulation of mixed convection heat transfer to carbon dioxide at supercritical pressure. *Proceedings of the Institution of Mechanical Engineers, Part C: Journal of Mechanical Engineering Science*, *218*(11), 1281–1296.

Their Results:

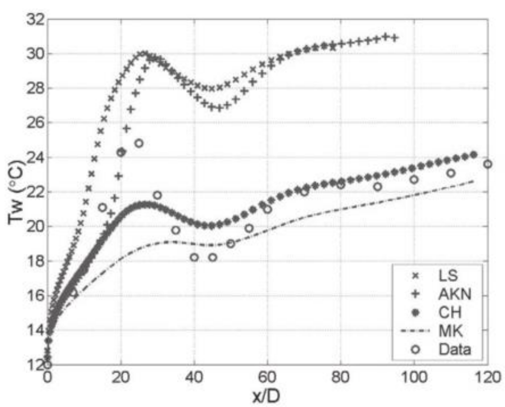

Case 1. T_{in}=8°C, q=6950W/m^2, m=0.058kg/s

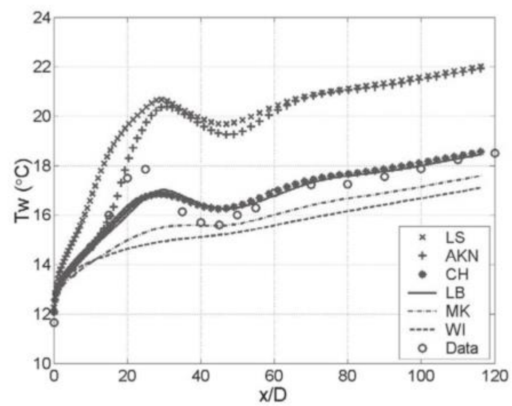

Case 2. T_{in}=10°C, q=2600W/m^2, m=0.041kg/s

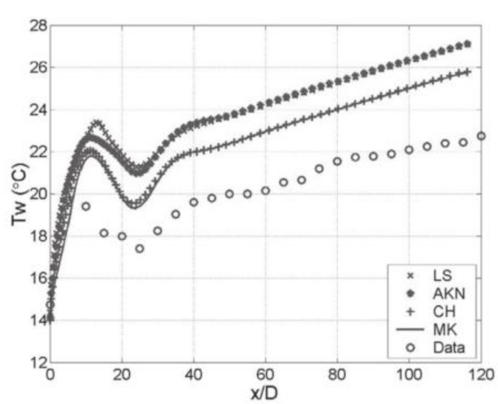

Case 3. T_{in}=10°C, q=4100W/m^2, m=0.029kg/s

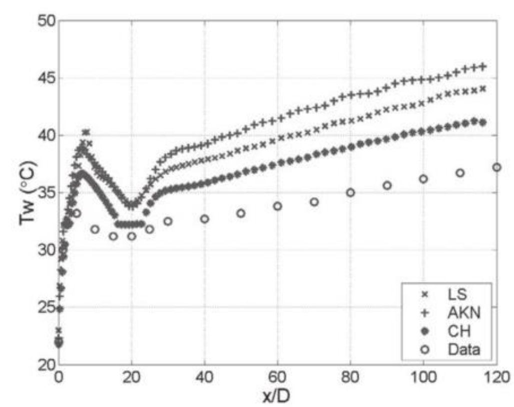

Case 4. T_{in}=10°C, q=15100W/m^2, m=0.041kg/s

Abbreviations: k-epsilon low-Reynolds models: LS, CH, LB, AKN, MK; k-omega model by Wilcox: WI

2.2 New Results by the author in STAR-CCM+

Rerun several cases using RST, SST, and SLR models in Star-CCM+

Main interest of this study: $T_w<T_{pc}$

Results:

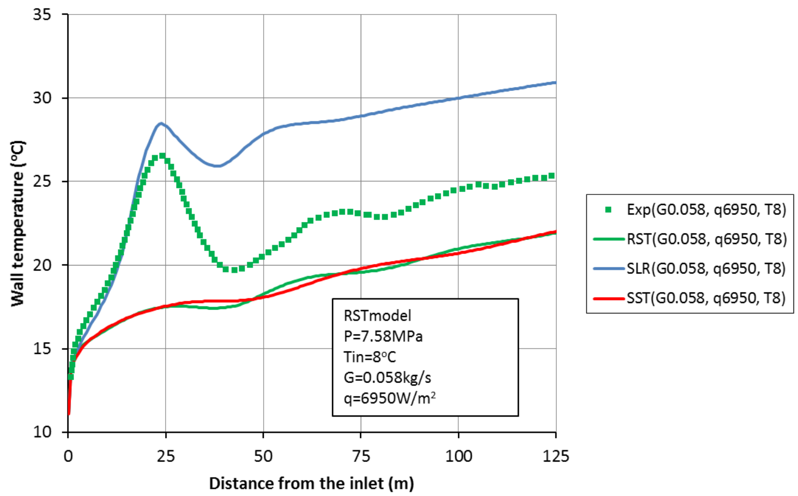

Figure 102 Wall temperature distribution by RST, SST, and SLR for Case 1

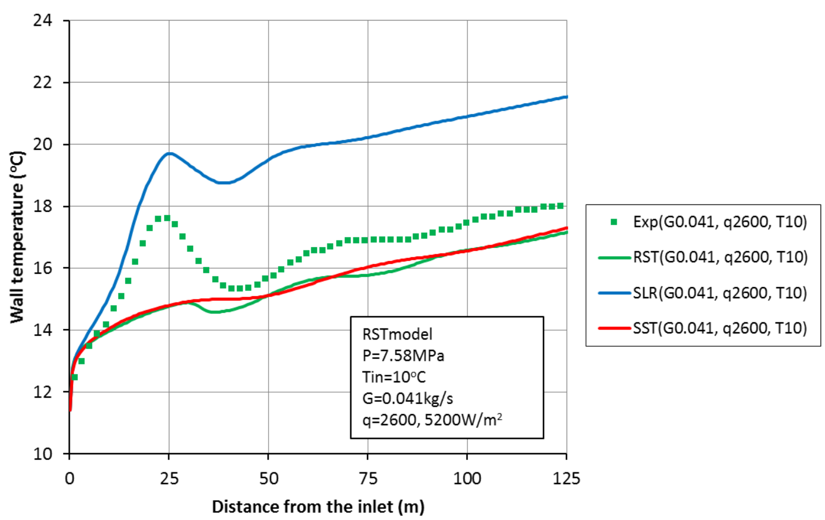

Figure 103 Wall temperature distribution by RST, SST, and SLR for Case 2

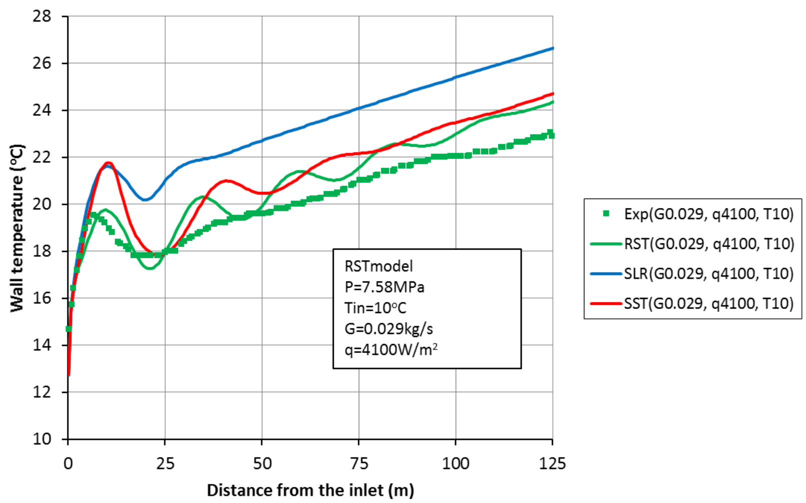

Figure 104 Wall temperature distribution by RST, SST, and SLR for Case 3

It can be seen from Figure *102* and Figure *103* that both RST and SST fail to predict the HTD observed in experiments, and the downstream wall temperature is underestimated. SLR model, on the other hand, is able to qualitatively predict the onset of HTD. However, the peak temperature and the downstream temperatures are significantly overestimated. These behaviors are consistent with what are found in this thesis.

Figure *104* shows the wall temperature distributions predicted by these turbulence models at relatively higher heat-flux-to-mass-flux ratio. Again, SLR model over-predict the peak temperature, as well as the downstream wall temperatures. RST and SST models in this case is able to qualitatively predict the first temperature peak. RST model is quantitatively better than SST and SLR models. However, the downstream temperature predicted by RST is wavy which is very different from the experiments. The wall temperature here is below T_{pc}, which implies that the RST and SST models can predict the HTD quite well in a few high heat-flux-to-mass-flux cases even though $T_w<T_{pc}$.

3. AKN Model - Mass Flux Effect in H_2O Study

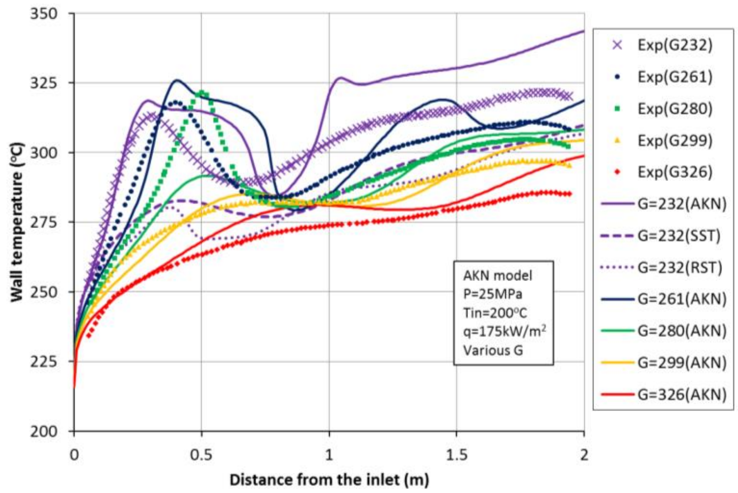

Figure 105 Wall temperature distribution by AKN model at various mass fluxes (low heat flux)

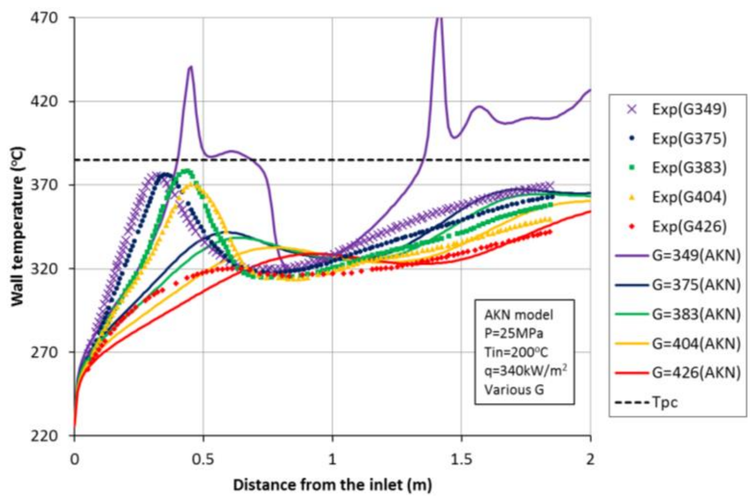

Figure 106 Wall temperature distribution by AKN model at various mass fluxes (high heat flux)

4. Sensitivity Study of Heat Flux and Mass Flux in H_2O Study

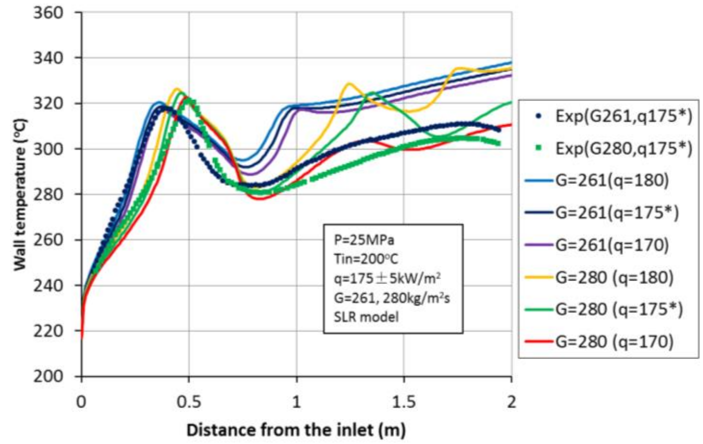

Figure 107 Sensitivity study of heat flux at q=175kW/m^2 by SLR model

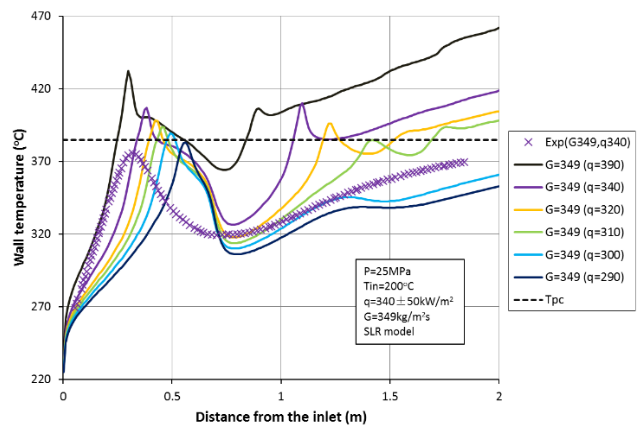

Figure 108 Sensitivity study of heat flux at q=340kW/m^2, G=349kg/m^{2}s by SLR model

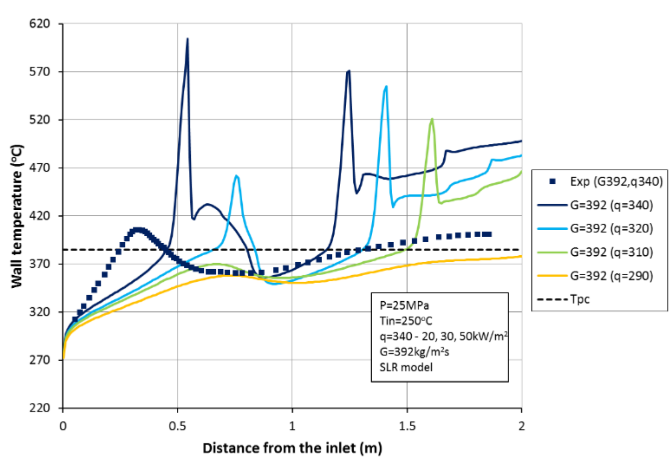

Figure 109 Sensitivity study of heat flux at q=340kW/m^2, G=392kg/m^{2}s by SLR model

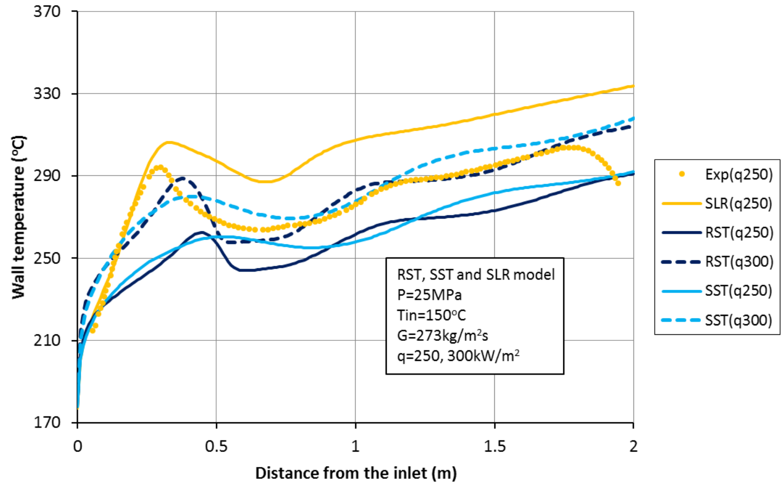

Figure 110 Effect of heat flux by RST and SST – T_{in}=150°C, q=250kW/m^2, G=273kg/m^{2}s

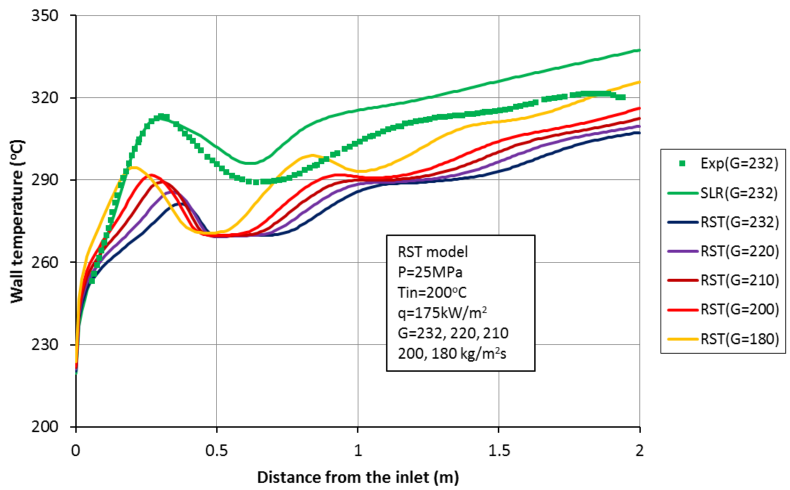

Figure 111 Effect of mass flux by RST model – T_{in}=200°C, q=175kW/m^2, G=232kg/m^{2}s